Abstract

The Parkinson's Gene VPS13C Encodes an ER-Lysosome Lipid Transfer Protein Linking Lysosomal Lipid Homeostasis and cGAS/STING-Mediated Innate Immunity

William F. Hancock-Cerutti

2022

Biallelic loss-of-function mutations in VPS13C cause early-onset Parkinson's Disease (PD), and the VPS13C locus is a GWAS hit for sporadic PD risk. VPS13C is a member of the VPS13 family, which in humans contains three other proteins, VPS13A, VPS13B, and VPS13D, all with ties to neurological diseases. Mutations in VPS13A cause chorea-acanthocytosis a Huntington's like syndrome with dysmorphic erythrocytes, mutations in VPS13B cause the neurodevelopmental disorder Cohen syndrome, and mutations in VPS13D cause spastic ataxia with varying presentation. The molecular function of these proteins, why their loss cause neurological diseases, and why they are each associated with distinct diseases despite their homology have all been open questions. In yeast, the single Vps13 protein localizes to contact sites between the mitochondria and vacuole, the yeast lysosome, and at the nuclear-vacuolar junction (NVJ), where multiple lines of indirect evidence has hinted that it may play a role in lipid transfer between these organelles. To understand whether human VPS13 proteins have diverged in their subcellular localization, we employed a combination of light and electron microscopy to demonstrate that VPS13A localizes to contact sites between the endoplasmic reticulum (ER) and mitochondria, while VPS13C localizes to contact sites between the ER and late endosomes/lysosomes. Both proteins also share a localization at ER-lipid droplet contact sites. We further show that the N-terminal portion of VPS13 forms a novel, tubular, hydrophobic cavity that can solubilize and transport glycerolipids between membranes. These findings identify VPS13 as a lipid transporter between the ER and other organelles, implicating defects in membrane lipid homeostasis in neurological disorders resulting from their mutations. Sequence and secondary structure similarity between the N-terminal portions of Vps13 and other proteins such as the autophagy protein ATG2 suggested lipid transport roles for these proteins as well, which has since been demonstrated. We next investigated the cellular phenotypes of VPS13C loss-of-function in an attempt to shed light on the pathophysiology of VPS13C-associated PD. We used CRISPR-Cas9 to generate VPS13C-knockout (VPS13C^{KO}) HeLa cells. These cells have more lysosomes compared to WT, with accumulation of both membrane and luminal lysosomal proteins. These lysosomes have an altered lipid profile, including a substantial decrease in ether-linked phospholipids and an accumulation of di-22:6-BMP, a biomarker of the PD-associated leucine-rich repeat kinase 2 (LRRK2) G2019S mutation. In addition, the DNA-sensing cGAS/STING pathway, which was recently implicated in PD pathogenesis, is activated in these cells. This activation results from a combination of elevated mitochondrial DNA in the cytosol and a defect in the degradation of activated STING, a lysosome-dependent process. These results suggest a link between ER-lysosome lipid transfer and innate immune activation and place VPS13C in pathways relevant to PD pathogenesis. Further exploration of these pathways has the potential to yield new mechanistic understanding and novel therapeutic strategies for this debilitating illness.

The Parkinson's Gene VPS13C Encodes an ER-Lysosome Lipid Transfer Protein Linking Lysosomal Lipid Homeostasis and cGAS/STING-Mediated Innate Immunity

A Dissertation
Presented to the Faculty of the Graduate School
Of
Yale University
in Candidacy for the Degree of
Doctor of Philosophy

By
William F. Hancock-Cerutti
Dissertation Director: Pietro De Camilli, MD
May 2022

Table of Contents

CHAPTER 1: INTRODUCTION 12

1.1 ORGANELLE DYSFUNCTION IN PARKINSON'S DISEASE 13
1.2 ENDOSOME-LYSOSOME PATHWAYS 15
1.2.1 LRRK2 16
1.2.2 GBA1 16
1.2.3 ATP13A2 17
1.3 MITOCHONDRIA PATHWAYS 18
1.3.1 PINK1 and Parkin 18
1.4 MITOCHONDRIA-LYSOSOME CROSSTALK 20
1.5 LIPID TRANSFER AT MEMBRANE CONTACT SITES 21
1.6 ER-LYSOSOME CONTACT SITES 23
1.7 THE VPS13C FAMILY OF PROTEINS 24
1.7.1 Yeast Vps13 25
1.7.2 The mammalian VPS13 family 26
1.7.3 VPS13A 29
1.7.4 VPS13B 30
1.7.5 VPS13C 31
1.7.6 VPS13D 32

2 CHAPTER 2: VPS13A AND VPS13C ARE LIPID TRANSPORT PROTEINS DIFFERENTIALLY LOCALIZED AT ER CONTACT SITES 34

2.1 ABSTRACT 35
2.2 INTRODUCTION 35
2.3 RESULTS 38
2.3.1 VPS13A and VPS13C are localized at organelle contact sites 38
2.3.2 FFAT motifs in VPS13A and VPS13C mediate tethering of the ER 50
2.3.3 C-Terminal regions of VPS13A and VPS13C contain binding sites for other organelles 54
2.3.4 The N-terminal portion of VPS13 has lipid transport properties 59
2.3.5 The N-terminal region of VPS13 contains a hydrophobic cavity 69
2.4 DISCUSSION 74

3 CHAPTER 3: THE EFFECTS OF VPS13C LOSS-OF-FUNCTION ON LYSOSOME BIOLOGY 79

3.1 INTRODUCTION 80
3.2 RESULTS 81
3.2.1 Cis and trans determinants of VPS13C binding to late endosomes 81
*3.2.2 Mutation of multiple conserved asparagine residues in the **β**-propeller domain prevent binding to late-endosomes, but mutations associated with Lewy-Body dementia have no effect 84*
3.2.3 Loss of VPS13C results in perturbation of lysosomal homeostasis 88
3.2.4 Loss of VPS13C causes alterations in lipid classes in whole cell and lysosomal lipidome 91
3.2.5 Enhanced levels of di-22:6-BMP in VPS13C^{KO} HeLa cells 95
3.2.6 Enhanced levels of di-22:6-BMP in VPS13C^{KO} iPSC induced neurons 98
3.3 DISCUSSION 100

4 CHAPTER 4: VPS13C LOSS-OF-FUNCTION IN HELA CELLS CAUSES ACTIVATION OF THE STING PATHWAY BY CYTOSOLIC MTDNA. 103

4.1 INTRODUCTION 104
4.2 RESULTS 105
4.2.1 Activation of the cGAS/STING pathway 105
4.2.2 Role of mtDNA escape in cGAS/STING activation in VPS13C^{KO} cells. 108
4.2.3 Steady-state change in the localization of STING in VPS13C^{KO} cells 112
4.2.4 Silencing of cGAS unmasks cGAMP responsiveness of VPS13C^{KO} cells and reveals impaired STING degradation 117
4.3 DISCUSSION 124

5 CHAPTER 5: DISCUSSION AND FUTURE DIRECTIONS 127
5.1 VPS13: A NOVEL CLASS OF LIPID TRANSFER PROTEINS AT MEMBRANE CONTACT SITES 128
5.2 POSSIBLE MECHANISMS DRIVING LIPID TRANSFER 130
5.3 POSSIBLE CELLULAR FUNCTIONS OF VPS13C GERMANE TO PD 133
5.3.1 Function of VPS13C in glial cells 133
5.3.2 Lipid changes in relation to PD 134
5.3.3 A role for VPS13C in de novo membrane formation? 135
5.4 CONCLUSION 138

6 CHAPTER 6: MATERIALS AND METHODS 139
6.1 MATERIALS AND METHODS FOR CHAPTER 2 140
6.1.1 Reagents 140
6.1.2 Bioinformatic analysis 141
6.1.3 Generation of constructs 141
6.1.4 Protein expression and purification 142
6.1.5 Protein crystallization, structure determination, and refinement 143
6.1.6 Lipid analysis of Vps13 by mass spectrometry 144
6.1.7 Liposome preparation 145
6.1.8 In vitro lipid-binding assay 145
6.1.9 In vitro lipid-transfer FRET assays 145
6.1.10 Cell culture and transfection 146
6.1.11 Generation of 2×HA-tagged VPS13A and VPS13C CRISPR– knock-in HeLa cell line 147
6.1.12 Fixed- and live-cell imaging 148
6.1.13 Correlative fluorescence and EM microscopy 149
6.1.14 Image processing, analysis, and statistics 149
6.2 MATERIALS AND METHODS FOR CHAPTER 3 AND 4 151
6.2.1 DNA plasmids 151
6.2.2 Antibodies 152
6.2.3 Cell culture and transfection 152
6.2.4 Generation of Stable STING-GFP cells using retrovirus 153
6.2.5 Generation of CRISPR-KO and CRISPR-KI rescue cell lines 153
6.2.6 Live-cell imaging 154
6.2.7 Immunofluorescence 155
6.2.8 Image processing and analysis 155
6.2.9 Synthesis of colloidal dextran-conjugated superparamagnetic iron-oxide nanoparticles (SPIONs) 156
6.2.10 Immunoblotting 156
6.2.11 Purification of lysosomes with dextran-conjugated SPIONs 157
6.2.12 Lipid extraction for mass spectrometry lipidomics 158
6.2.13 Mass spectrometry data acquisition 159
6.2.14 Data analysis and post-processing 160
6.2.15 Measurement of di-22:6-BMP and di-18:1-BMP 160
6.2.16 Depletion of mtDNA 160
6.2.17 Quantitative PCR 160
6.2.18 Fractionation of cytosol by centrifugation 161
6.2.19 Statistical analyses 162

Table of Figures

FIGURE 1.1 CELLULAR PATHWAYS OF PD GENES. 14
FIGURE 1.2 LOCALIZATION OF YEAST AND MAMMALIAN LIPID TRANSFER PROTEINS. 22
FIGURE 1.3 SCHEMATIC REPRESENTATION OF VPS13 PROTEIN DOMAINS AND SIMILARITY TO ATG2. 28
FIGURE 2.1 VPS13A LOCALIZES AT ER–MITOCHONDRIA AND ER–LIPID DROPLET CONTACT SITES. 39
FIGURE 2.2 VPS13A LOCALIZES AT ER–MITOCHONDRIA AND ER–LIPID DROPLET CONTACTS AND NOT ON ENDOLYSOSOMES. 41
FIGURE 2.3 VPS13C LOCALIZES AT ER–ENDOSOME CONTACTS. 47
FIGURE 2.4 VPS13A AND VPS13C LOCALIZATIONS. 48
FIGURE 2.5 THE PREDICTED FFAT MOTIF IN VPS13A AND VPS13C TETHERS THEM TO THE ER. 52
FIGURE 2.6 REGIONS OF VPS13A AND VPS13C THAT BIND MITOCHONDRIA AND LATE ENDOSOMES/LYSOSOMES. 55
FIGURE 2.7 BINDING REGIONS FOR MITOCHONDRIA OR LATE ENDOSOMES LIE IN THE C-TERMINAL HALF OF VPS13 PROTEINS. 57
FIGURE 2.8 N-TERMINAL PORTIONS OF VPS13 SOLUBILIZE AND TRANSPORT LIPIDS. 61
FIGURE 2.9 LOW-RESOLUTION CHARACTERIZATION OF THE VPS13 N-TERMINAL REGION. 64
FIGURE 2.10 LIPID TRANSFER ASSAYS: VPS13A DOES NOT PROMOTE MEMBRANE FUSION OR HEMIFUSION. 67
FIGURE 2.11 MULTIPLE SEQUENCE ALIGNMENT FOR THE VPS13 N TERMINUS (VPS13A). 73
FIGURE 2.12 DIAGRAM DEPICTING SITES OF ACTION OF VPS13A AND VPS13C. 76
FIGURE 3.1 TRANS BINDING FACTORS OF VPS13C ON LATE ENDOSOMES 83
FIGURE 3.2 CIS BINDING FACTORS OF VPS13C 87
FIGURE 3.3 DELETION OF VPS13C CAUSES ACCUMULATION OF LYSOSOMES. 90
FIGURE 3.4 LOSS OF VPS13C RESULTS IN ALTERED CELLULAR AND LYSOSOMAL LIPID COMPOSITION 94
FIGURE 3.5 ANALYSIS OF LIPID SPECIES AND BMP LEVELS 97
FIGURE 3.6 ANALYSIS OF BMP LEVELS IN VPS13C^{KO} INEURONS 99
FIGURE 4.1 LOSS OF VPS13C RESULTS IN ACTIVATION OF THE CGAS/STING PATHWAY 107
FIGURE 4.2 ACTIVATION OF THE CGAS/STING PATHWAY IN VPS13C^{KO} CELLS IS DEPENDENT ON INCREASED CYTOSOLIC MTDNA 110
FIGURE 4.3 CONTROL EXPERIMENTS FOR FIGURE 4.2 AND NORMAL MTDNA NUCLEOID MORPHOLOGY IN VPS13C^{KO} CELLS 111
FIGURE 4.4 STING IS ACTIVATED AND TRANSLOCATED OUT OF THE ER AT BASELINE IN VPS13C^{KO} CELLS 114
FIGURE 4.5 STING SIGNALING IS ELEVATED IN VPS13C^{KO} CELLS LINES STABLY EXPRESSING STING-GFP 116
FIGURE 4.6 SILENCING OF CGAS UNMASKS CGAMP RESPONSIVENESS AND REVEALS IMPAIRED STING DEGRADATION IN VPS13C^{KO} CELLS 119
FIGURE 4.7 SILENCING OF CGAS UNMASKS CGAMP RESPONSIVENESS AND REVEALS IMPAIRED STING DEGRADATION IN VPS13C^{KO} CELLS 121
FIGURE 4.8 EFGR AND LC3 DEGRADATION ARE NOT IMPAIRED IN VPS13C^{KO} CELLS 123
FIGURE 5.1 STRUCTURES AND PROPOSED FUNCTION OF VPS13 FAMILY AND RELATED PROTEINS 129
FIGURE 5.2 POSSIBLE MECHANISMS DRIVING LIPID TRANSFER 132
FIGURE 5.3 KNOWN AND HYPOTHESIZED ROLES OF VPS13 FAMILY AND ATG2 IN DE NOVO MEMBRANE EXPANSION. 137

Table of Figures

TABLE 1 70

Acknowledgements

I would like to express the deepest appreciation to the entire De Camilli lab. Science is an inherently capricious pursuit, and my wonderful colleagues over the past five years have been a consistent foil to the emotional vicissitudes of research. On weeks when all of my experiments failed, my culture dishes were contaminated, my hypotheses negative, I still enjoyed coming to work because of the brilliant, funny, kind, and hardworking people persevering alongside me. To Dr. Pietro De Camilli, my thesis advisor, for his unbridled love of science, his generous and reliable mentorship, and his support and understanding during difficult times. Pietro's enthusiasm is infectious because of its sincerity. He leads us by example to read more broadly, think more critically, and imagine more boldly. To the core De Camilli lab team, past and present, Frank, Vikki, Heather, Rose, Lila, Alice, and now Mona, who keep the lab running, always have a backup tube, always make time to help when my poor planning threatens to ruin an experiment, or just to have a casual chat about life when too much science threatens to eclipse my humanity. To all of the postdocs and research scientists who bring such a diverse wealth of backgrounds, experiences, techniques, and perspectives that make the lab a vibrant, cutting-edge place to do science. Especially to Marianna, my first teacher in the De Camilli lab, who taught me much of what I know about being a scientist. Aside from being a dedicated mentor and collaborator, Mari has been a dear friend who I've relied on through many difficult times, and trust implicitly both with my insecurities as a scientist and with my life on the other end of a climbing rope. Finally, to the group of ne'er-do-wells known as the De Camilli Boyz: Mick, Andres, and Lizz, the other graduate students that I shared this journey with, who made the stressful work of research not only tolerable but fun. Lunches, coffee breaks, and occasional trips with the Boyz kept me sane and laughing during this lengthy endeavor. It really feels so improbably lucky that I happened to start in the lab right at the same time as two brilliant, funny, kind compatriots who are both passionate about science and also down to complain about the negative aspects of science with me. I'm inspired by them every day and can't wait to see all the things they will discover.

I would like to thank the collaborators outside the De Camilli lab who have contributed invaluably to this work, as well as my thesis Committee, Dr. Sreeganga Chandra, Dr. Shawn Ferguson, Dr. Marc Hammarlund, and Dr. Michael Nitabach, for their wide-ranging expertise and thoughtful guidance. I am also deeply indebted to the many wonderful people who make up the administration of the MD-PhD program, the Interdisciplinary Neuroscience Program, and the Departments of Cell Biology and Neuroscience.

Finally, I'd like to thank my family, which includes both my biological family and the dear people who have become my family in New Haven. My MD-PhD classmates, who share the unique bond of navigating not one but two grueling training programs, and who despite being intimidatingly smart and impressive people have always radiated kindness, empathy, and the perfect amount of goofiness. To my many beloved housemates of 8 Edwards St. over the past seven years, who became no less than a family, and built no less than a home. I'm endlessly grateful for the extraordinary little community that we created, which fostered so much personal growth and was just so darn fun – a truly special place and time. To Edwin and John, my first hosts in New Haven who have nourished me both spiritually and calorically ever since. To my OG family, my parents Callie and Rob, who can never be paid back enough, and Mern, my forever best bud, trusted co-conspirator, and frequent therapist. Knowing that they would love and be proud of me even if I didn't do a PhD is what allowed me to do a PhD. Kyle belongs in this part, my brother. To Jenny, my partner in all things, whose sense of duty to oppressed peoples keeps me perpetually in awe, and whose sense of humor keeps me perpetually laughing.

I’m so grateful for you all.

Communications arising from P.h.D. Candidate

Kumar, N.*, M. Leonzino*, **W. Hancock-Cerutti**, F. A. Horenkamp, P. Li, J. A. Lees, H. Wheeler, K. M. Reinisch and P. De Camilli (2018). "VPS13A and VPS13C are lipid transport proteins differentially localized at ER contact sites." J Cell Biol **217**(10): 3625-3639.

Ugur, B.*, **W. Hancock-Cerutti***, M. Leonzino* and P. De Camilli (2020). "Role of VPS13, a protein with similarity to ATG2, in physiology and disease." Curr Opin Genet Dev **65**: 61-68.

Hancock-Cerutti, W., Z. Wu, A. K. Tharkeshwar, S. M. Ferguson, G. S. Shadel and P. De Camilli (2021). "ER-lysosome lipid transfer protein VPS13C/PARK23 prevents aberrant mtDNA-dependent STING signaling." bioRxiv.

*These authors contributed equally

Chapter 1: Introduction

Portions of this chapter were previously published as:

Ugur, B.*, **W. Hancock-Cerutti***, M. Leonzino* and P. De Camilli (2020). "Role of VPS13, a protein with similarity to ATG2, in physiology and disease." Curr Opin Genet Dev **65**: 61-68.

1.1 Organelle dysfunction in Parkinson’s disease

Parkinson’s disease (PD) is the second most common neurodegenerative disease and most common neurodegenerative movement disorder, with a prevalence of about 1% in people over 65 years-old(Kalia and Lang, 2015; Nussbaum and Ellis, 2003; Poewe et al., 2017). Its core symptoms include tremor, rigidity, bradykinesia/akinesia, and postural instability. These motor symptoms result from the degeneration of dopaminergic neurons in the substantia nigra pars compacta (SNpc). Over time, non-motor symptoms may develop including depression, anxiety, visual hallucinations, autonomic dysfunction, and cognitive decline. Current therapeutic strategies, chiefly carbidopa/levodopa, aim at attenuating symptoms, and there are currently no disease modifying treatments.(Kalia and Lang, 2015)

Though the majority of PD cases are sporadic, it is estimated that between 5-10% of cases are attributable to familial genetic mutations(Blauwendraat et al., 2020; Lin and Farrer, 2014). Investigation into the biological mechanisms linking these mutations to PD has great potential to shed light on common cellular pathways involved in familial and sporadic PD and may inform future therapeutic strategies. Cell biological studies of PD genes have revealed common cellular pathways and organelle systems that seem to be important in PD pathogenesis, including endocytosis (especially synaptic vesicle recycling), mitophagy, and the endolysosomal system (Figure 1.1). The following sections will highlight the role of PD genes in lysosome and mitochondria biology.

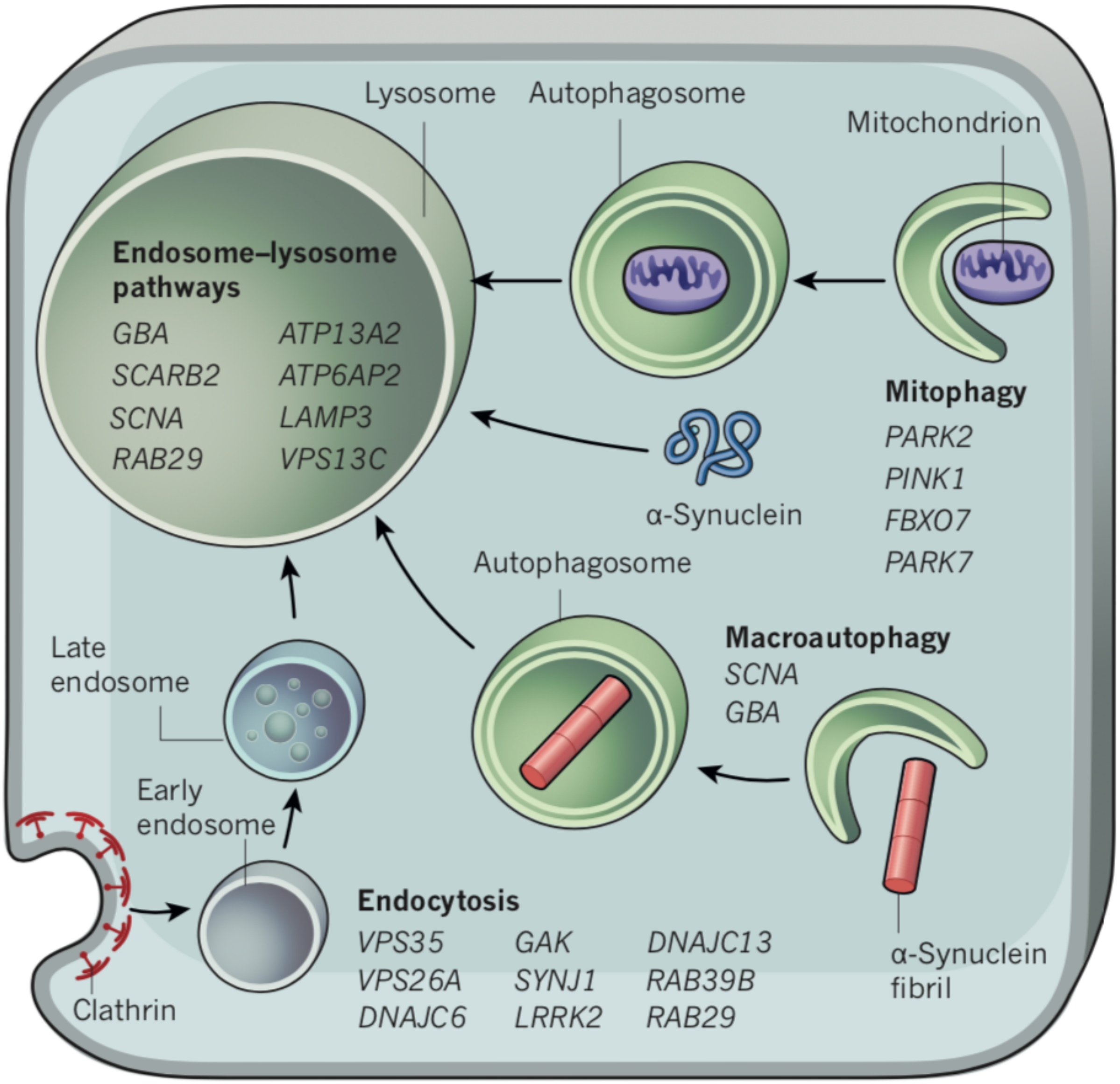

Figure 1.1 Cellular pathways of PD genes.

Multiple PD genes have been implicated in mitophagy, endocytosis, and the endo-lysosomal system. Identifying points of convergence of these pathways may provide insights for future therapeutic development. Adapted from (Abeliovich and Gitler, 2016)

1.2 Endosome-lysosome pathways

Lysosomes are acidic (pH ~4.5) membrane bound organelles which contain hydrolytic enzymes, including nucleases, proteases, and lipases, among others, that function to degrade macromolecules for re-use by the cell. The limiting phospholipid membrane is protected by a glycocalyx, a 5-12 nm-thick network of carbohydrate residues covalently linked to the luminal moieties of its integral membrane proteins, including LAMP1. (Yim and Mizushima, 2020) The luminal cargo bound for degradation derives primarily from fusion of lysosomes with either autophagosomes or late-endosomes/multivesicular bodies (MVBs). Moreover, lysosomes function as critical signaling hubs for cell metabolism, sensing nutrient levels and orchestrating appropriate metabolic responses.(Ferguson, 2015) Neurons are particularly vulnerable to defects in lysosomal function, as they are post-mitotic and thus rely on a tightly regulated balance of autophagy and lysosomal degradation to maintain homeostasis and prevent buildup of cytotoxic protein aggregates or damaged organelles. Numerous PD genes have been implicated in endo-lysosomal biology, including LRRK2(Bonet-Ponce et al., 2020; Ysselstein et al., 2019), GBA1(Mazzulli et al., 2011; Taguchi et al., 2017), ATP13A2 (van Veen et al., 2020), LIMP2 (SCARB2) (Rothaug et al., 2014), and VPS35 (Zavodszky et al., 2014), among others. PD-associated mutations have been shown to impair numerous endo-lysosomal functions and parameters, including lysosomal pH, protein and lipid degradation, tubulation and sorting, and autophagic clearance. Multiple PD genes have been shown to play a role in lysosomal lipid biology specifically, and are highlighted below.

1.2.1 LRRK2

LRRK2 mutations appear to have pleiotropic effects on lysosomal function – LRRK2 deficiency disrupts Golgi to lysosome trafficking (Lanning, 2018) while LRRK2 gain-of-function mutations cause lysosomal deacidification and defects in protein degradation and autolysosome maturation (Henry et al., 2015; Wallings et al., 2019). More recently, LRRK2 has been shown to be recruited to damaged lysosomes (Eguchi et al., 2018), where it promotes tubulation and vesicle sorting by a mechanism involving phosphorylation of Rab10 and Rab35 and recruitment of JIP4. LRRK2 gain-of-function mutations also appear to affect lysosomal lipids, as higher levels of the endo-lysosome specific lipid di-22:6-BMP were found in the urine of LRRK2 (G2019S) mutation carriers (Alcalay et al., 2020).

1.2.2 GBA1

GBA1, which encodes the luminal enzyme glucocerebrosidase (GCase), is also involved in lysosomal lipid metabolism as it catalyzes the lysis of glucosylceramide into glucose and ceramide. Aside from causing Gaucher's disease, GBA1 mutations are the most common genetic risk factor for PD (Aharon-Peretz et al., 2004; Bultron et al., 2010; Sidransky and Lopez, 2012). Loss-of-function of GCase causes accumulation of glucosylceramide and other glycosphingolipids, which has been shown to promote α-synuclein aggregation and pathology(Taguchi et al., 2017; Zunke et al., 2018). Patient derived neurons from PD patients with GBA1 mutations also had prolonged mitochondria-lysosome contacts, leading to reduced mitochondrial function (Kim et al., 2021). GBA1 also has interesting synergy with other PD genes, including SNCA, LRRK2, and LIMP2. Levels of GCase were found to be reduced even in sporadic PD, and to inversely correlate with α-synuclein levels (Murphy et al., 2014).

Furthermore, gain-of-function LRRK2 mutations were shown to reduce lysosomal GCase (the protein product of GBA1) activity (Ysselstein et al., 2019), suggesting synergy between LRRK2 and GBA1, the two most prevalent PD genes. LIMP2 was identified as a receptor for the proper trafficking of GCase to the lysosome (Reczek et al., 2007), and is critical for GCase activity (Rothaug et al., 2014). Thus, GCase expression and activity seem to play a central role in PD pathogenesis, even in the absence of GBA1 mutations.

1.2.3 ATP13A2

Loss-of-function mutations in ATP13A2 were found to be the cause of Kufor-Rakeb syndrome, a familial, early-onset Parkinsonism with combined pyramidal degeneration and dementia.(Ramirez et al., 2006) ATP13A2 encodes a transmembrane endo/lysosome associated P5-type transport ATPase. Deficiency of ATP13A2 in animal models causes reduced cathepsin D processing and activity (Matsui et al., 2013), and leads to accumulation of lipofuscin that was positive for mitochondrial ATP synthase subunit c.(Sato et al., 2016) It was also reported that ATP13A2 can be activated by binding phosphatidylinositol-(3,5)bisphosphate (PI(3,5)P2),(Holemans et al., 2015) and that loss of ATP13A2 or its PI(3,5)P_2 binding activity causes defects in lysosomal cargo sorting and accumulation of ubiquitinated proteins.(Demirsoy et al., 2017) More recently, ATP13A2 was shown to be a lysosomal polyamine exporter, functioning to promote uptake of polyamines (including spermidine) by endocytosis and facilitating their trafficking out of the lysosome and into the cytosol.(van Veen et al., 2020) In accordance with this function, loss of ATP13A2 sensitizes cells to lysosomal dysfunction, rupture, and cell death when exposed to high concentrations of polyamines. Polyamines have previously been implicated in PD pathogenesis.(Lewandowski et al., 2010)

1.3 Mitochondria pathways

Mitochondria have been proposed to play a major role in PD pathogenesis, especially since the discovery of the roles of PINK1 and Parkin in the process of mitophagy(Pickrell and Youle, 2015). Mitochondrial DNA (mtDNA) may also play a role in PD development. Mitochondria contain their own DNA nucleoid, encoding 11 mRNAs encoding 13 protiens, 2 rRNAs, and 22 tRNAs.(Bonekamp and Larsson, 2018) Mutations in mtDNA accumulate with aging, and are enriched in PD brains(Martin-Jimenez et al., 2020), and particularly in the substantia nigra(Bender et al., 2006; Kraytsberg et al., 2006). While mtDNA copy number increases with age in the substantia nigra of healthy individuals to maintain a steady complement of WT mtDNA, this increase does not occur in PD patients, thus effectively increasing the proportion of mutated mtDNA(Dolle et al., 2016). In addition, patients with mitochondrial disease caused by mutations in the mtDNA polymerase γ are prone to accumulating mtDNA mutations and are at increased risk for PD(Reeve et al., 2013).

1.3.1 PINK1 and Parkin

Mutations in either PINK1 or Parkin cause early onset, autosomal recessive PD.(Abeliovich and Gitler, 2016; Blauwendraat et al., 2020) These proteins function in a common pathway to facilitate selective degradation of damaged mitochondria by autophagy, a process termed mitophagy. (Palikaras et al., 2018; Youle and Narendra, 2011) In normal, healthy mitochondria, PINK1 is rapidly transported from the outer to the inner mitochondrial membrane (IMM), where it is cleaved by proteases and degraded by the proteasome.(Sekine and Youle, 2018) When mitochondria are depolarized, transport to the IMM does not occur, and PINK1 remains stably associated with the outer mitochondrial membrane (OMM), where it undergoes autophosphorylation. Phosphorylated PINK1 then recruits and phosphorylates Parkin, promoting its association with the OMM and inducing its E3 ubiquitin ligase activity. Parkin catalyzes the ubiquitination of multiple OMM protein substrates, and PINK1 phosphorylates these ubiquitin chains, recruiting more Parkin in a feedforward loop.(Ordureau et al., 2014) This ubiquitination can trigger a range of events from targeted to wholesale degradation: individual ubiquitinated proteins can be degraded by the proteasome(Pickrell and Youle, 2015), subdomains of OMM can undergo fission to form mitochondrial derived vesicles (MDVs) destined for the endo-lysosomal system(McLelland et al., 2016), or the entire mitochondria may be engulfed by an autophagosome for degradation in the lysosome. (Lazarou et al., 2015)

Though Parkin-KO mice do not show signs of neurodegeneration under basal conditions, introducing additional mitochondrial stress by breeding them with mice which accumulate mtDNA mutations (Mutator mice) leads to dopaminergic neuron degradation and motor phenotypes.(Pickrell et al., 2015) In a follow-up study, it was shown that introducing mitochondrial stress by either exhaustive exercise or using a Mutator background leads to inflammation and dopaminergic neuron degradation and motor phenotypes in both PINK1-KO and Parkin-KO mice.(Sliter et al., 2018) Excess mtDNA was found in the circulation, presumably leaking from damaged mitochondria that could not be efficiently degraded in the absence of PINK1 or Parkin. Moreover, these inflammatory and degenerative phenotypes could be rescued by deletion of the gene STING, which encodes a protein that functions in an innate immune pathway that senses double stranded DNA and triggers expression of interferon stimulated genes (ISGs) and inflammatory mediators.

1.4 Mitochondria-lysosome crosstalk

Though much study of organelles has been siloed, a growing body of literature is exploring the interplay between different organelles in physiological and pathophysiological contexts. In particular, numerous interactions between mitochondria and lysosomes have been established, including crosstalk by soluble factors(Hughes et al.; Yambire et al., 2019), organelle contact sites (Kim et al., 2021; Wong et al., 2018), or well established pathways like mitophagy(Palikaras et al., 2018; Pickrell and Youle, 2015).

Soluble factors that have been shown to play a role in lysosome mitochondria crosstalk include iron(Yambire et al., 2019), and amino acids (Hughes et al., 2020). Lysosomal de-acidification has been shown to cause cellular iron deficiency in both cell and animal models, which in turn led to mitochondrial disfunction, destabilization of mtDNA, and ISG upregulation (Yambire et al., 2019). These phenotypes could be rescued by iron supplementation. A separate study in yeast found that disrupting lysosome homeostasis by depletion of V-ATPase led to disruption of cellular amino acid metabolism, and that accumulation of cysteine, specifically, in the cytosol caused limited bioavailability of iron, thus impairing mitochondrial function.(Hughes et al., 2020)

Contact sites between mitochondria and lysosomes have also been proposed to play a role in physiology and disease.(Kim et al., 2021; Wong et al., 2018) Though the protein or proteins mediating this tethering have yet to be identified, it was shown that Rab7 GTP hydrolysis catalyzed by Fis1 dependent recruitment of the Rab7 GAP TBC1D15 promoted mitochondria-lysosome untethering(Wong et al., 2018). These contact sites appear to mark sites of mitochondrial fission(Wong et al., 2018) and also to be prolonged in the setting of GBA1 mutant cells from PD patients(Kim et al., 2021).

1.5 Lipid transfer at membrane contact sites

Within eukaryotic cells a variety of organelles coordinate to facilitate the metabolic reactions necessary to maintain life. Many of these organelles are defined by one or more limiting phospholipid membranes, each with distinct protein and lipid compositions. How the distinct lipid compositions of organelles are created and maintained is a question fundamental to biology, and traditionally has been attributed to vesicular traffic and enzymatic reactions. More recently, attention has been paid to the role of membrane contact sites (MCS), regions in the cell where the membranes of two organelles come into close apposition without fusing, usually defined as 10-30 nM. (Levine and Loewen, 2006; Saheki and De Camilli, 2017). These MCS are formed by proteins which can bind molecules on both organelles, thus forming a tether between them (1.2). Among numerous functions including ion transport and organelle fission, MCS serve as focal points for protein-mediated lipid transfer between apposing membranes.(Peretti et al., 2019) The proteins that facilitate this lipid transfer generally contain a hydrophobic cavity or grove capable of binding to hydrophobic moieties of lipid species.(Wong et al., 2019) Many families of lipid transfer proteins (LTPs) have been identified, with specificity for different inter-organelle contact sites and different lipid cargoes. Some bind a single lipid molecule at a time and function as shuttles between membranes, while other contain extended grooves capable of harboring multiple lipid molecules, and may function as bridges or shuttles.(Peretti et al., 2019; Saheki and De Camilli, 2017; Wong et al., 2019)

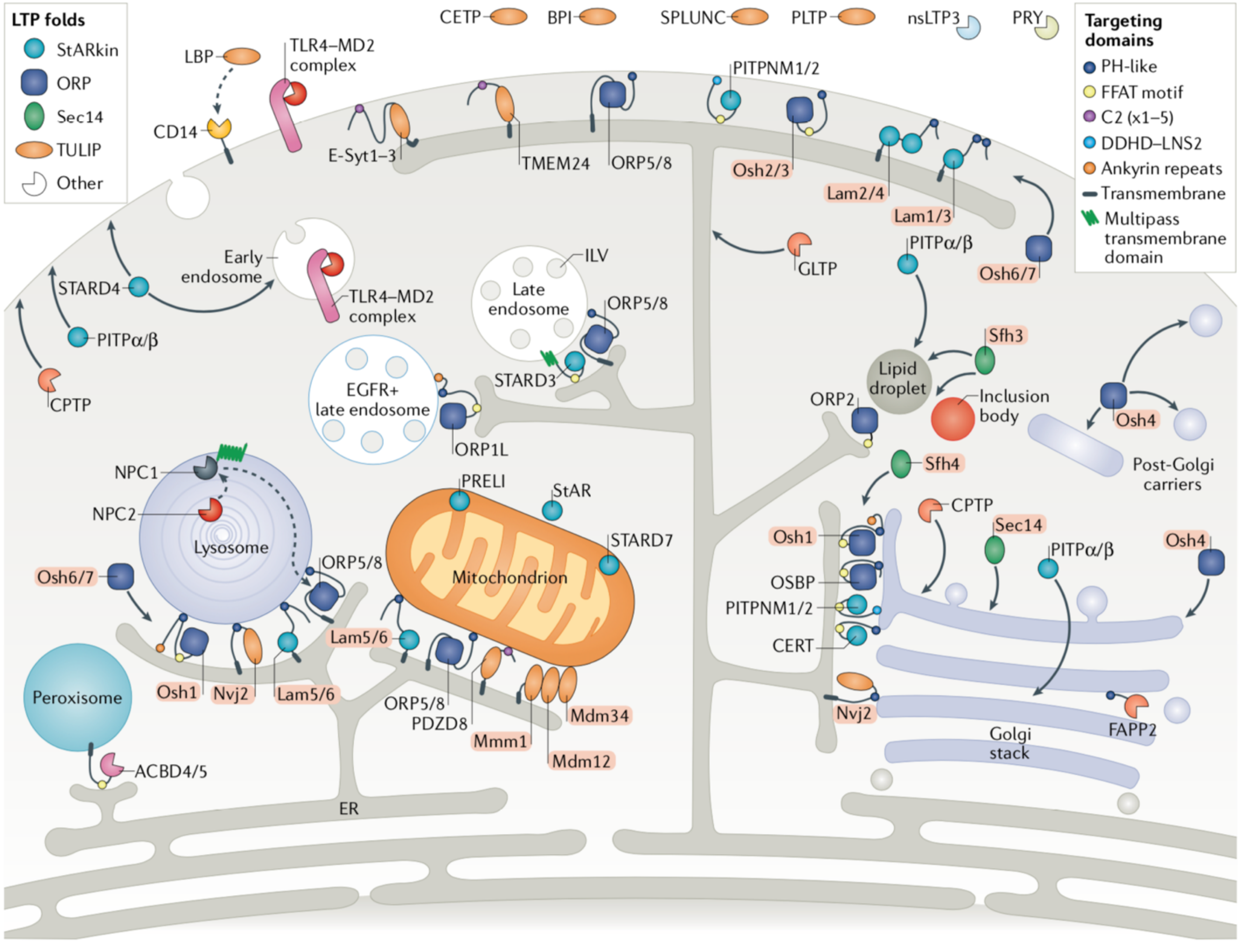

Figure 1.2 Localization of yeast and mammalian lipid transfer proteins.

Cartoons of known lipid transfer domains (LTP) are shown in the upper left box and known targeting domains in the upper right. Adapted from (Wong et al., 2019)

1.6 ER-Lysosome contact sites

As the primary site of cellular macromolecule degradation, the lysosome has numerous mechanisms to recycle catabolized products out of the lumen for reuse. Amino acids, for instance, are transported in and out of the lysosome in a tightly regulated manner (Abu-Remaileh et al., 2017; Wyant et al., 2017). How lipids are recycled from the lysosomal lumen is an active area of investigation, and is likely to also be tightly regulated. As lipids are hydrophobic and poorly soluble in the aqueous phase, this recycling likely occurs via vesicular trafficking or via lipid transfer protein mediated trafficking to apposing membranes.

Cholesterol is transported through the lysosomal lumen by NPC2, before being handed off to the transmembrane protein NPC1 (Li et al., 2017). Loss-of-function mutations in NPC1 or NPC2 cause Niemann-Pick disease type C, a lysosomal storage disorder involving cellular accumulation of cholesterol and other lipid species(Vanier, 2010). How cholesterol is trafficked from the limiting membrane to other intracellular membranes, including the ER, remains to be elucidated.

STARD3, a transmembrane protein of late endosomes that forms ER-late endosome contact sites by binding VAP on the ER, and has surprisingly been reported to transfer cholesterol primarily *from* the ER to late endosomes via its START domain, such that its overexpression causes the accumulation of cholesterol in late endosomes at the expense of the plasma membrane(Wilhelm et al., 2017).

The pathway by which phospholipids are recycled from lysosomes is not yet defined, though it may be accomplished through a combination of lysosomal tubulation(Bonet-Ponce et al., 2020; Yu et al., 2010) or by lipid transfer proteins at membrane contact sites. Recently, PDZD8, which contains an SMP lipid transfer domain domain capable of binding glycerophospholipids and ceramides(Gao et al., 2022), was shown to localize to contact sites between the ER and late-endosomes, where it interacts with Rab7(Guillen-Samander et al., 2019) and Protrudin(Elbaz-Alon et al., 2020). PDZD8 mediated lipid transfer was recently shown to be necessary for late-endosome/lysosome positioning and neurite outgrowth(Gao et al., 2022), suggesting the importance of ER-endo/lysosome phospholipid transfer in a neuronal model.

1.7 The VPS13C family of proteins

In 2001 Rampoldi et al. (Rampoldi et al., 2001) mapped mutations responsible for chorea acanthocytosis to a gene encoding a very large and uncharacterized protein (hence called chorein) which showed similarities to the yeast SOI1/VPS13 protein (Bankaitis et al., 1986; Brickner and Fuller, 1997). Chorein is one of four mammalian paralogues that are encoded by four distinct genes broadly expressed in different tissues (Velayos-Baeza et al.). Mutations in the other three paralogues also result in neurodegenerative or neurodevelopmental diseases: Cohen Syndrome (VPS13B) (Kolehmainen et al., 2003), Parkinson's disease (VPS13C) (Darvish et al., 2018; Lesage et al., 2016; Schormair et al., 2018) and spinocerebellar ataxia (VPS13D) (Gauthier et al., 2018; Seong et al., 2018). Studies in a variety of model organisms and cell types over the last several years had identified cellular processes which are affected by the loss of VPS13 family proteins, including autophagy, cytoskeletal organization, Ca^{2+} signaling and mitochondria homeostasis, but a mechanistic understanding of VPS13 function had remained elusive (Rzepnikowska et al., 2017). Very recent studies have shed light on such function by demonstrating that VPS13 is the founding member of a new family of lipid transport proteins that act at contact sites between different organelles. This brief review will discuss these new findings and, where possible, will attempt to relate these new findings to the pathological manifestations resulting from VPS13 mutations.

1.7.1 Yeast Vps13

The single Vps13 yeast protein (alias: SOI1 (Redding et al., 1996), Vpt2 (Bankaitis et al., 1986) was originally identified in a screen for proteins involved in Vacuolar Protein Sorting (Bankaitis et al., 1986; Brickner and Fuller, 1997). Subsequently, yeast Vps13 was implicated in recycling traffic between endosome and the Golgi complex (Brickner and Fuller, 1997; Redding et al., 1996), in the maintenance of mitochondrial membrane integrity (Park et al., 2016), and in the growth of the prospore membrane (Park et al., 2015; Park and Neiman; Park et al., 2013). This is a special membrane generated de novo during the second meiotic division that ultimately becomes the plasma membrane of the four daughter spore cells. This process of de novo membrane growth shares some similarities with the formation of autophagosomes as well as the acrosome in mammalian sperm cells.

A first insight into a link between Vps13 and lipid dynamics emerged from the discovery that the function of yeast Vps13 is partially redundant with that of the ERMES complex (ER to Mitochondria Encounter Structure (ERMES) (Lang et al., 2015). ERMES is a multi-subunit complex localized at contacts between the ER and mitochondria thought to mediate lipid transfer between these two organelles, which are not connected by vesicular transport (Kornmann et al., 2009). Yeast cells with ERMES deletions exhibit growth defects but are viable, suggesting the existence of additional pathways for lipid exchange between ER and mitochondria. A search for such bypass pathways identified spontaneous dominant Vps13 mutations as suppressors of the

ERMES-knockout (KO) phenotype. Conversely, the combined deficiency of ERMES and VPS13 resulted in lethality (Lang et al.; Park et al., 2016). It was also shown that Vps13 localizes to contacts between the yeast vacuole (which corresponds to lysosomes in mammalian cells) and either the nuclear envelope (which is part of the ER), or mitochondria (Lang et al.; Park et al., 2016). Collectively, these findings raised the possibility that yeast Vps13 may cooperate in lipid transfer between the ER and mitochondria via an indirect route involving the vacuole.

Intriguingly, yeast Vps13 was also identified in a screen for mutations that cause the escape of mitochondrial DNA (mtDNA) to the nucleus, termed YME mutants (for Yeast Mitochondrial Escape)(Thorsness and Fox, 1993). A follow-up study reported that in the case of Yme1, an ATP-dependent metalloprotease in the mitochondria and another hit in the YME screen, mitochondrial DNA leakage was dependent on vacuolar turnover of a mitochondrial compartment (Campbell and Thorsness, 1998).

1.7.2 The mammalian VPS13 family

VPS13 is a large (>3000 a.a.) evolutionary conserved protein. Structural predictions had revealed repetitive modules comprising primarily ß-strands throughout its N-terminal half, followed by WD40-like elements (alias VAB domain (Bean et al., 2018)), a DH-like (DH-L) fold and a PH domain at the C-terminus (Fidler et al., 2016; Kumar et al., 2018) (Figure 1.3). Additional motifs present in VPS13 proteins are shown in Figure 1.3. Interestingly, VPS13 has structural and functional similarities to the autophagy factor ATG2 (Figure 1.3) (Kumar et al., 2018; Maeda et al., 2019; Osawa et al., 2019; Pfisterer et al., 2014; Valverde et al., 2019), a protein required for the growth of the autophagic membrane, another example of de-novo growth of a membrane. VPS13 and ATG2 share small stretches of primary a.a. similarity (chorein and

ATG-C homology domain) (Figure 1.3) (Kumar et al., 2018; Velayos-Baeza et al., 2004), as well as longer stretches of predicted secondary and tertiary structure homology.

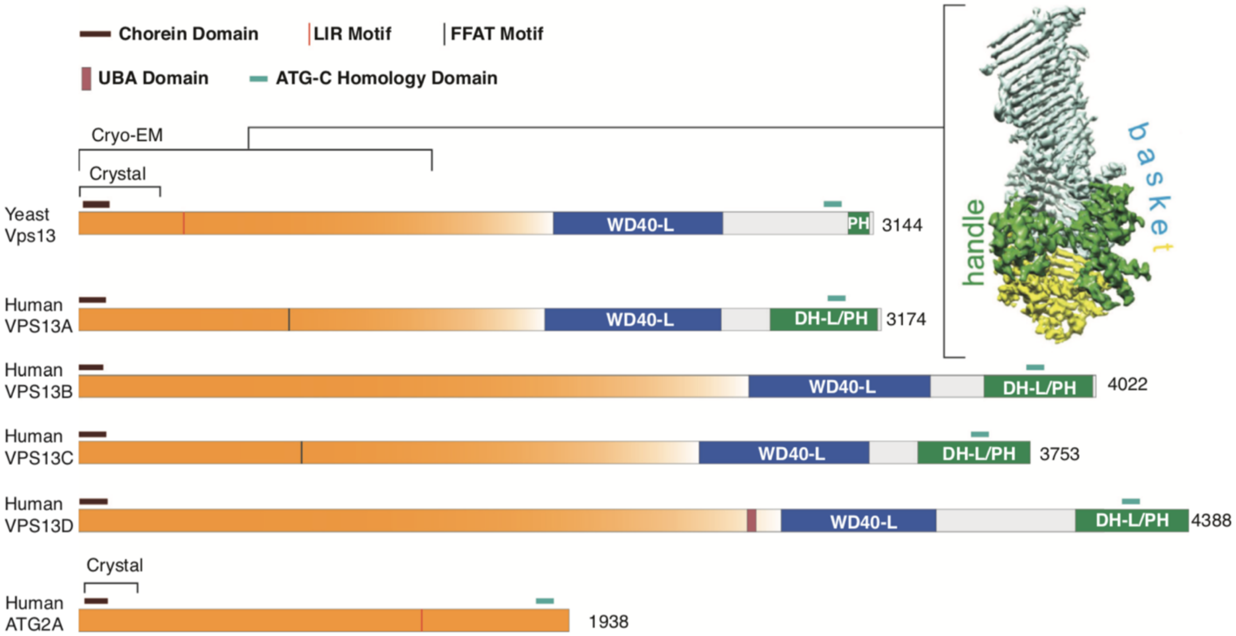

Figure 1.3 Schematic representation of VPS13 protein domains and similarity to ATG2. The N-terminal half of VPS13 proteins is indicated in orange. Primary sequence similarities occur in the chorein and ATG-C domains. A clear FFAT motif is present in VPS13A and VPS13C. VPS13D has an additional ubiquitin-associated domain (UBA in pink). Both yeast Vps13 and human ATG2A have LC3 interacting regions (LIR motif). The density map of the N-terminal region of VPS13 from Chaetomium thermophilum solved by Cryo-EM is shown at top right (Li et al., 2020).

1.7.3 VPS13A

Chorea-acanthocytosis (ChAc) is a rare, Huntington-like autosomal recessive neurodegenerative disorder caused by mutations in VPS13A (Peikert et al., 2018; Rampoldi et al., 2001). It is characterized by involuntary hyperkinetic movements (chorea; hence the name ‘chorein’ for the approximately 150 a.a. N-terminal fragment which represents the most conserved region among VPS13s and between VPS13 and ATG2). Movement symptoms in chorea-acanthocytosis correlate with the degeneration of striatal neurons, and with the presence of abnormally shaped blood cells (acanthocytosis). The age of onset is typically around the third decade of life, and core symptoms are often accompanied by seizures, dystonia and behavioral changes (Peikert et al., 2018). Similar clinical conditions, referred to as neuroacanthocytosis are McLeod syndrome (MLS), Huntington disease-like 2 (HDL 2) and pantothenate kinase-associated neurodegeneration (PKAN)(Peikert et al., 2018)). Given the lipid transport function of VPS13, it is of special interest that several of these other conditions involve alterations of lipid metabolism.

Vps13a^{KO} mice were reported to have acanthocytosis, mild neurological and behavioral abnormalities that vary strongly depending on the strain background (Sakimoto et al.; Tomemori et al., 2005), and male infertility. The latter was attributed to a defect in sperm motility resulting from abnormal mitochondria in the sperm midpiece (Nagata et al., 2018). Flies with loss-of-function mutations in the Vps13 gene (Drosophila Vps13 is most similar to human VPS13A and C, while the two other fly paralogues, Vps13b and Vps13d, represent the orthologues of mammalian VPS13B and VPS13D) have reduced lifespan, age-dependent decline in climbing ability, and large vacuoles in the brain (Vonk et al., 2017). In addition, Vps13 mutant adult fly eyes display lipid droplet accumulation (Yeshaw et al., 2019), which is a common hallmark observed with neurodegeneration induced by ROS due to mitochondrial defects (Liu et al.). Expression of human VPS13A in Vps13 mutant flies rescues a subset of these phenotypes (Yeshaw et al., 2019).

1.7.4 VPS13B

Autosomal recessive mutations in VPS13B cause Cohen Syndrome (CS) (Kolehmainen et al., 2003), a neurodevelopmental disorder characterized by postnatal microcephaly, intellectual disability, craniofacial anomalies, hypotonia, progressive retinal dysfunction and truncal fat accumulation (Cohen et al., 1973). Clinical manifestations, which can be heterogeneous, generally start to manifest by two years of age. In agreement with the reported accumulation of VPS13B in the Golgi complex, an abnormal Golgi structure was observed in fibroblasts from Cohen syndrome patients and in various mammalian cell lines upon RNAi-dependent knockdown (Duplomb et al., 2014; Seifert et al., 2011). Moreover, consistent with Golgi complex's role in glycosylation, serum proteins derived from CS patients have an unusual glycosylation pattern (Duplomb et al., 2014). Abnormal glycosylation of cell surface molecules may play a role in developmental defects, given the important role of glycoproteins in cell–cell interactions.

Vps13b^{KO} mice display behavioral/neurological impairments, including defects in spatial learning and reduced activity in the open field test (Kim et al., 2019). Furthermore, as in the case of the Vps13a^{KO} mouse model, Vps13b^{KO} mice display male infertility, but via a different mechanism. Lack of Vps13b results in impaired formation of the acrosomal membrane of sperm cells, a process which occurs in proximity of the Golgi complex area and which is required for subsequent egg fertilization (Da Costa et al., 2020). An intriguing hypothesis is that impaired acrosomal membrane growth may reflect a role of Vps13b in de novo membrane biogenesis, akin to the proposed role of yeast Vps13 in growth of the sporulation membrane (see above) and of ATG2 in the growth of the phagophore.

1.7.5 VPS13C

Biallelic mutations resulting in VPS13C loss-of-function cause rare cases of early onset, autosomal recessive Parkinson's Disease (PD) in multiple families (Darvish et al., 2018; Lesage et al., 2016; Schormair et al., 2018) (hence the VPS13C alias PARK23) and genetic variations in the VPS13C locus have been associated with PD risk by GWAS studies (Cook et al., 2017; Nalls et al., 2014; Zhang et al., 2017). All of the VPS13C mutations identified in autosomal dominant PD cases are either frameshift, nonsense, splice site,(Lesage et al., 2016; Schormair et al., 2018) or major deletion (Darvish et al., 2018), and thus likely to be complete loss-of-function. PD due to VPS13 loss-of-function initially presents with akinetic asymmetrical rigid syndrome and variable tremor and dystonia that is responsive to levodopa, but subsequently cognitive decline and motor neuron signs may also develop. Post-mortem examination of a patient brain revealed widespread diffuse alpha-synuclein-positive and ubiquitin-positive Lewy body pathology. Vps13c^{KO} mice do not have obvious neurological phenotypes (our unpublished observations), in line with the lack of such phenotypes in mouse models of other forms of familial PD.

The identification of yeast Vps13 as a protein with a role in mitochondria biology (Lang et al., 2015; Park et al., 2016) initially suggested a primary action of VPS13C at mitochondria. Accordingly, it was reported that siRNA-mediated knockdown of VPS13C in Cos7 cells leads to multiple mitochondrial defects (Lesage et al., 2016). Most interestingly, the same study also showed that VPS13C knockdown increased mitochondrial recruitment of pink1 and parkin, upregulation of parkin transcripts, and an exacerbation of pink1/parkin-dependent mitophagy upon CCCP treatment (Lesage et al., 2016). This study described the presence of VPS13C on mitochondria by subcellular fractionation. It was also shown that VPS13C plays a role in adipogenesis and lipolysis in adipocytes (Ramseyer et al., 2018; Yang et al., 2016).

1.7.6 VPS13D

Bi-allelic mutations in VPS13D have been identified as a cause of early onset, clinically heterogenous movement disorders in more than 20 patients from three separate studies (Gauthier et al., 2018; Nasser et al., 2019; Seong et al., 2018). The most common core clinical diagnosis was cerebellar ataxia with or without spasticity, as well as dystonia, hypotonia, spastic paraparesis, and chorea. Two patients had confirmed microcephaly and three suffered from seizures. Three patients presented as a pure hereditary spastic paraplegia, and were also the oldest at time of onset (40, 42, and 63), all features suggestive of a milder phenotype (Nasser et al., 2019; Seong et al., 2018).

Of all the VPS13 proteins, VPS13D seems to be the most important for cell viability. The KO of VPS13D is embryonically lethal in both mice and flies, and VPS13D was found to be essential in several human cell lines (Blomen et al., 2015; Seong et al., 2018). Moreover, none of the human cases appear to be homozygous for total loss-of-function alleles (Gauthier et al., 2018; Nasser et al., 2019; Seong et al., 2018), consistent with the possibility that biallelic total loss of function mutations may be lethal. Accordingly, the VPS13D gene is predicted to be intolerant to mutations, with a pLI score of 1.00 (Seong et al., 2018).

Genetic studies in flies have implicated VPS13D in the clearance of mitochondria in the gut and in neurons (Seong et al., 2018). More specifically, knockdown of Vps13D in the fly intestine causes a defect in mitochondrial clearance and mitophagy, as well as in the accumulation of large spherical mitochondria (Anding et al., 2018). The UBA domain of VPS13D is thought to be important for this function (Figure 1.3). Relevant to neurological diseases, knockdown of Vps13D in fly motor neurons causes a reduction in mitochondria in the axon as well as at the neuromuscular junction (Seong et al., 2018), suggesting a link of VPS13D to mitochondria motility. The defect in mitophagy was proposed to be mediated by an impairment of phagophore enlargement around mitochondria (Insolera et al., 2021) reminiscent of the phenotype displayed by ATG2 defects. Abnormal mitochondria and a defect in mitophagy were also observed in a VPS13D KO human cell line (Anding et al., 2018) and in fibroblasts from patients with VPS13D mutations (Seong et al., 2018). Mitochondrial pathology in progressive cerebellar ataxias have been previously described (Bargiela et al., 2015) consistent with a primary role of mitochondrial dysfunction in VPS13D-dependent neurological manifestations. It was recently shown that VPS13D loss of function also results in the partial or complete loss of peroxisomes. (Baldwin et al., 2021) These results are supported by the identification of different isoforms of the rho GTPase Miro as the binding partners of VPS13D on both mitochondria and peroxisomes.(Guillen-Samander et al., 2021)

Chapter 2: VPS13A and VPS13C are lipid transport proteins differentially localized at ER contact sites

This chapter was originally published as:

Kumar, N.*, M. Leonzino*, **W. Hancock-Cerutti**, F. A. Horenkamp, P. Li, J. A. Lees, H. Wheeler, K. M. Reinisch and P. De Camilli (2018). "VPS13A and VPS13C are lipid transport proteins differentially localized at ER contact sites." J Cell Biol **217**(10): 3625-3639.

Author contribution
W. Hancock-Cerutti designed and performed all experiments with VPS13C and assisted with preparation of the figures and manuscript.

2.1 Abstract

Mutations in the human VPS13 genes are responsible for neurodevelopmental and neurodegenerative disorders including chorea acanthocytosis (VPS13A) and Parkinson's disease (VPS13C). The mechanisms of these diseases are unknown. Genetic studies in yeast hinted that Vps13 may have a role in lipid exchange between organelles. In this study, we show that the N-terminal portion of VPS13 is tubular, with a hydrophobic cavity that can solubilize and transport glycerolipids between membranes. We also show that human VPS13A and VPS13C bind to the ER, tethering it to mitochondria (VPS13A), to late endosome/lysosomes (VPS13C), and to lipid droplets (both VPS13A and VPS13C). These findings identify VPS13 as a lipid transporter between the ER and other organelles, implicating defects in membrane lipid homeostasis in neurological disorders resulting from their mutations. Sequence and secondary structure similarity between the N-terminal portions of Vps13 and other proteins such as the autophagy protein ATG2 suggest lipid transport roles for these proteins as well.

2.2 Introduction

A major path for the transport of bilayer lipids between membranes is vesicular transport. However, this route can be bypassed by lipid transport proteins that extract lipids from a membrane, shield them from the aqueous cytosolic environment within hydrophobic cavities, and deliver them to a target membrane. Often, these proteins also function as tethers between two participating organelles, thus making transport more efficient (Gatta and Levine, 2017; Holthuis and Menon, 2014; Lahiri et al., 2015; Saheki and De Camilli, 2017). Protein-mediated transport is particularly important for lipid exchange between the ER and mitochondria as these two organelles are not connected by membrane traffic, yet mitochondria use precursors imported from the ER to produce most of their lipids (Dimmer and Rapaport, 2017). Conversely, lipids generated in mitochondria can be delivered to the ER for distribution to other membranes (Voelker, 1984).

Yeast studies have suggested that the ER–mitochondria encounter structures (ERMES) complex mediates this bidirectional lipid transport between the ER and mitochondria (AhYoung et al., 2015; Jeong et al., 2016; Kornmann et al., 2009). However, other pathways for ER–mitochondria lipid transfer must also exist (Elbaz-Alon et al., 2014; Honscher et al., 2014) as ERMES deletion is not lethal (Lang et al., 2015). A protein that may function in such a pathway is Vps13, as spontaneous gain-of-function mutations in its gene could rescue the growth defect of yeast ERMES mutants (Lang et al., 2015). Additionally, mutants lacking both ERMES and Vps13 are not viable (Lang et al., 2015). Vps13 localizes at contacts between the mitochondria and the vacuole (so called v-CLAMPs, for vacuole and mitochondria patches) and between the vacuole and the ER (nuclear–vacuole junction; NVJ; (Lang et al., 2015)). An interesting hypothesis is that Vps13 may mediate lipid transfer between the vacuole and other membranes and that it may provide an alternative indirect path for the flow of specific lipids between the ER and mitochondria via the vacuole. Defects in mitochondria membrane integrity observed in yeast mutants lacking either ERMES complex components or Vps13 (Hanekamp et al., 2002; Park et al., 2016) are consistent with this possibility. However, so far, there is no direct evidence that Vps13 can transfer lipids.

While the ERMES complex is not conserved in metazoan cells, members of the VPS13 family are expressed in all animal species, including humans, whose genome contains four VPS13 genes (VPS13A/Chorein, VPS13B, VPS13C, and VPS13D; (Velayos-Baeza et al., 2004)). The precise function of these proteins remains unclear, although they have been implicated in a variety of processes including membrane traffic at Golgi–endosome interfaces (De et al., 2017), cytoskeletal organization (Alesutan et al., 2013; Foller et al., 2012; Honisch et al., 2015; Schmidt et al., 2013; Shiokawa et al., 2013), calcium signaling (Pelzl et al., 2017), mitochondrial health (Lesage et al., 2016), and autophagy (Lupo et al., 2016; Munoz-Braceras et al., 2015). Interestingly, stretches of primary sequence similarity have been noted between VPS13 and ATG2, another protein of unknown function that is required for phagophore formation (Velikkakath et al., 2012; Wang et al., 2001). More specifically, similarities occur in the first ∼120 residues at the N terminus (referred to as the Chorein_N domain) and in a stretch of ∼70 aa in the C-terminal region (termed ATG_C in Pfam; (Munoz-Braceras et al., 2015; Pfisterer et al., 2014; Tamura et al., 2017)).

Human VPS13 proteins are of great biomedical interest as loss-of-function mutations in each of them are associated with genetic diseases: chorea acanthocytosis, a Huntington-like syndrome associated with red cell shape abnormalities (VPS13A; (Rampoldi et al., 2001; Ueno et al., 2001)); Cohen syndrome, a complex multisystem condition characterized by global developmental delay and intellectual disability (VPS13B; (Kolehmainen et al., 2003)); an early onset form of Parkinson's disease (VPS13C; (Lesage et al., 2016)); and a recently described form of ataxia with spasticity (VPS13D; (Gauthier et al., 2018; Seong et al., 2018)). Determining the function of these proteins will be key in elucidating the mechanisms of these diseases.

In this study, we demonstrate that the N-terminal region of Vps13 is a lipid transport module that can harbor glycerolipids and transfer them between bilayers. We also show that VPS13A, the closest homologue of yeast Vps13, localizes at contacts between the ER and mitochondria, suggesting that VPS13A may fulfill some of the functions of the ERMES complex in mammalian cells. Surprisingly, VPS13C, the paralogue most closely related to VPS13A, is instead localized at contacts between the ER and late endosomes/ lysosomes, revealing that duplication of VPS13 during evolution correlates with diversification of their sites of action.

2.3 Results

2.3.1 VPS13A and VPS13C are localized at organelle contact sites

To gain first insights into the properties of VPS13A, the chorea acanthocytosis gene, we investigated its subcellular localization. As available antibodies did not detect the protein by immunofluorescence (IF), we tagged it at a site found to preserve yeast Vps13 function ((Park et al., 2016); VPS13A^Halo or ^mCherry) and expressed it in Cos-7 or HeLa cells. By far the majority of the VPS13A signal occurred in the form of small patches arranged to form elongated structures (Figure 2.1 A, left). Coexpression of a mitochondrial marker (mito-BFP) and an ER marker (EGFP-Sec61β) identified these structures as mitochondrial profiles lying in close proximity to the ER (Figure 2.1, A and B; line scans in Figure 2.1 C; Figure 2.2 A; and quantification in Figure 2.2 B). Furthermore, in these cells, i.e., where VPS13A was overexpressed, areas of close proximity between the ER and mitochondria were increased (Figure 2.2 C). These findings are consistent with an ER-to-mitochondria tethering function of

VPS13A, consistent with the possibility that in metazoa, VPS13A may fulfill some of the functions of ERMES.

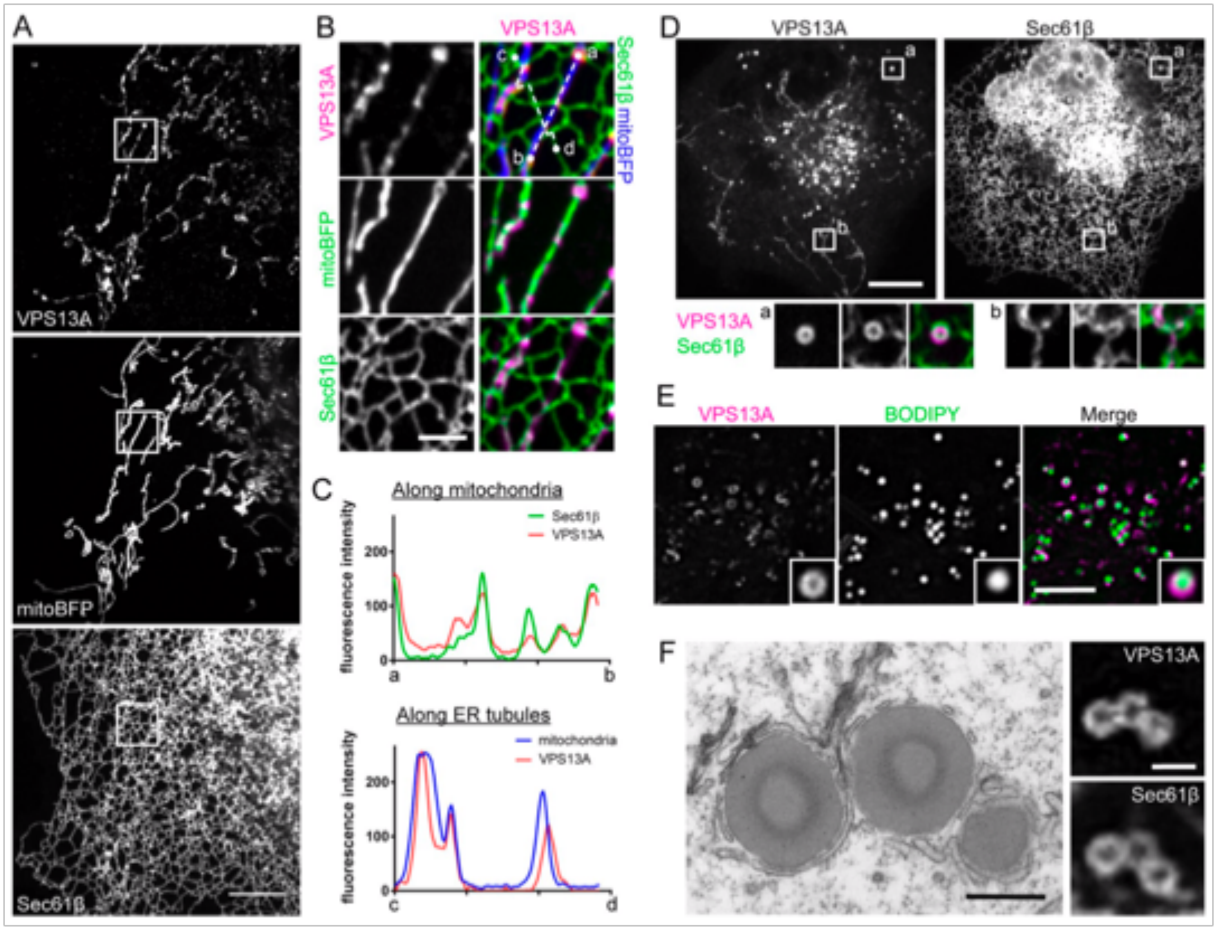

Figure 2.1 VPS13A localizes at ER–mitochondria and ER–lipid droplet contact sites. **(A)** Cos-7 cell expressing VPS13A^Halo, GFP-Sec61β, and mito-BFP showing overlap of VPS13A fluorescence with both mitochondria and ER. Bar, 10 μm. **(B)** High magnifications of the region indicated by white squares in A showing precise localization of VPS13A at sites of contact between ER and mitochondria. Bar, 2 μm. **(C)** Fluorescence intensity for the three indicated channels along a line either tracing the long axis of a mitochondrion (top) or ER tubules (bottom). Lines used for the plots are indicated by dashed lines in the merged image in B. **(D)** A Cos-7 cell expressing VPS13A^Halo and GFP-Sec61β shows two patterns of VPS13A

fluorescence both overlapping with the ER: dots (doughnuts; a) and elongated structures (b), shown at high magnification in the bottom panels. Bar, 10 µm; bottom panels, 3 × 3 µm. **(E)**

Figure 2.1 (Cont.) Live staining of neutral lipids with BODIPY 493/503 in a Cos-7 cell expressing VPS13A^Halo showing the presence of VPS13A around lipid droplets (insets). Bar, 5 µm; insets, 1.5 × 1.5 µm. **(F)** Correlative light EM of a Cos-7 cell expressing VPS13A^mChweey and GFP-Sec61β. Fluorescent images of three lipid droplets (right) and corresponding cell region shown by EM (left) demonstrate abundant presence of ER around the lipid droplets. Bars: 0.5 µm (left); 1 µm (right).

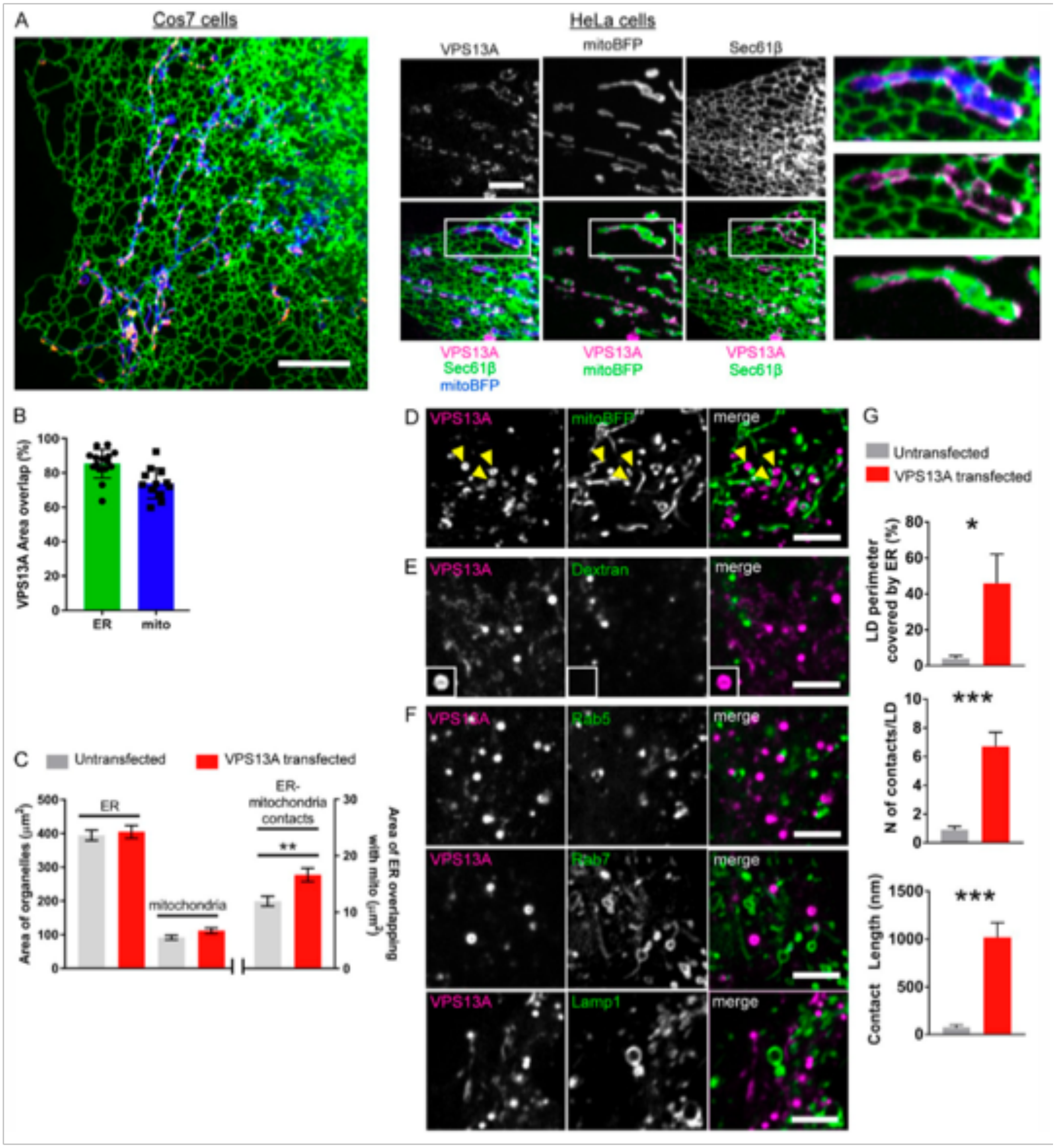

Figure 2.2 VPS13A localizes at ER–mitochondria and ER–lipid droplet contacts and not on endolysosomes.

(A) A Cos7 cell (left) and a HeLa cell (right) coexpressing VPS13A^mCherry, GFP-Sec61β, and mito-BFP showing overlap of the VPS13A signal with the ER at contacts with mitochondria. Bars, 10 µm (left); 5 µm (middle); 13 × 5.6 µm (right). **(B)** Percentage of VPS13A fluorescence

Figure 2.2 (Cont.) area that overlaps with Sec61β-positive structures (green bar; n = 15), with mito-BFP–positive structures (blue bars; n = 12), or with BODIPY 493/503. Analysis was performed on 20-μm^2 regions of Cos-7 cells from images acquired in two independent experiments. Data are shown as mean ± SEM, and each dot represent a single measurement. **(C)** Sec61β-positive area (ER) and mito-BFP– positive area (mitochondria) in control untransfected Cos-7 cells (gray bars; n = 22) and in VPS13A-transfected cells (red bars; n = 19) are plotted on the left y axis. Percentage of Sec61β-positive area overlapping with mito-BFP signal (ER–mitochondria contacts) in the same cells is plotted on the right y axis. Analysis was performed on 20-μm^2 regions of Cos-7 cells acquired in four independent experiments. Data are shown as mean ± SEM. **(D)** Cos-7 cells coexpressing VPS13A^Halo and mito-BFP showing that VPS13A-positive doughnuts (arrowheads) are not fragmented mitochondria. **(E)** Cos-7 cells expressing VPS13A^mCherry and incubated with dextran Alexa Fluor 488 for 30 min showing no overlap of the two signals. High-magnification insets show that VPS13A-positive doughnuts are not of endolysosomal origin as they do not contain dextran. **(F)** HeLa cells coexpressing VPS13A^mCherry and EGFP-tagged Rab5, Rab7, or Lamp1 showing that VPS13A does not overlap with any of these markers. All micrographs were acquired with live-cell imaging. Bars, 5 μM. **(G)** Quantification of ER–lipid droplet (LD) contacts in control Cos-7 cells (gray bars) or Cos-7 cells transfected with VPS13A (red bars) from EM micrographs. Contact length, number of contacts, and the percentage of lipid droplet perimeter covered with ER was measured in the entire area of three cells per group (>40 lipid droplets per group) obtained from two independent experiments. Data are represented as mean ± SEM, and groups were compared with a two-tailed Student t test. *, $P < 0.05$; **, $P < 0.01$; ***, $P < 0.001$. The much greater impact of VPS13A

Figure 2.2 (Cont.) overexpression on ER–lipid droplet contacts relative to ER–mitochondria contacts may indicate a more easily saturable binding partner (most likely a protein) on mitochondria.

In some cells, VPS13A fluorescence signal also appeared in the form of small doughnut-shaped spots that overlapped with the ER marker (Sec61β; Figure 2.1 D, inset a) but not with mitochondria (Figure 2.2 D). These structures were negative for preinternalized dextran (an endocytic tracer; Figure 2.2 E) and for markers of the endolysosomal system (Figure 2.2 F) and were instead identified as lipid droplets based on labeling with the neutral lipid marker BODIPY 493/503 (Figure 2.1 E). Correlative fluorescence EM analysis of VPS13A-transfected cells confirmed that VPS13A fluorescent doughnuts were lipid droplets enwrapped by ER tubules (Figure 2.1 F). EM also showed that contacts between the ER and lipid droplets were more abundant in VPS13A-overexpressing cells than in WT cells (Figure 2.2 G).

Lack of localization of VPS13A on organelles of the endolysosomal system was surprising as it contrasted with the localization of yeast Vps13 at contact sites between the vacuole and other membranes (Lang et al., 2015). We thus asked whether VPS13C, a Parkinson's disease–linked protein and the closest paralogue to VPS13A among human VPS13 proteins, was also absent from these organelles. VPS13C is similar to VPS13A throughout its length, with the exception of the presence of an ∼500-aa insert after position 807 most likely corresponding with a duplication of the upstream region. When VPS13C^mClover3 (tagged at the cognate site used for VPS13A) was coexpressed with VPS13A^mCherry in HeLa or Cos-7 cells, striking differences were observed in the localization of the two proteins (Figures 2.3 A and 2.4 A). No localization of VPS13C at mitochondria was observed (Figure 2.4 A). A major pool of VPS13C was instead localized on vesicular and tubular structures negative for VPS13A (Figures 2.3 A and 2.4 A) but positive for preinternalized dextran and generally surrounded by ER (Figure 2.3 B), suggesting that VPS13C populates contacts between ER and the endolysosomal system. Some of these vesicles were positive for the lysosomal marker LAMP1

(Figure 2.4 B) or for Rab7 (Figure 2.3 C), consistent with the reported binding of VPS13C to this Rab (McCray et al., 2010). A smaller pool of VPS13C did colocalize with VPS13A on doughnut-like structures (Figure 2.3 A, arrowheads, and Figure 2.4 A, arrowheads) that surrounded LipidTOX-stained lipid droplets (Figure 2.3 D), in agreement with the previously reported association of VPS13C with lipid droplets based on subcellular fractionation (Yang et al., 2016) and IF (Ramseyer et al., 2018). Lack of VPS13C at mitochondria contacts was unexpected as its mutations have been linked to mitochondrial dysfunction and Parkinson's disease (Lesage et al., 2016). However, mitochondrial dysfunction could represent an indirect effect of abnormalities in intracellular lipid transport.

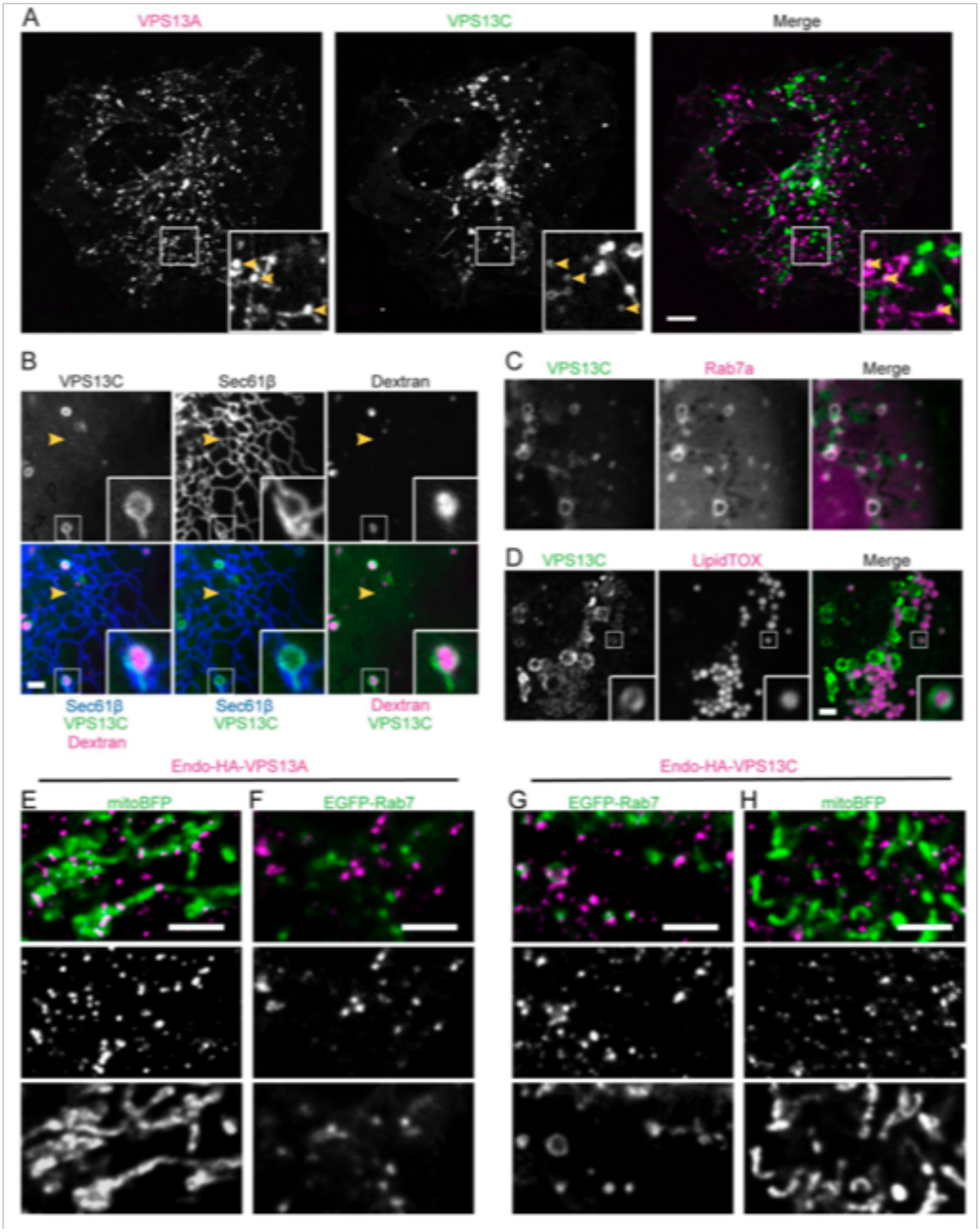
A
VPS13A
VPS13C
Merge
B
VPS13C
Sec61β
Dextran
Sec61β
VPS13C
Dextran
Sec61β
VPS13C
Dextran
VPS13C
C
VPS13C
Rab7a
Merge
D
VPS13C
LipidTOX
Merge
Endo-HA-VPS13A
Endo-HA-VPS13C
E
mitoBFP
F
EGFP-Rab7
G
EGFP-Rab7
H
mitoBFP

Figure 2.3 VPS13C localizes at ER–endosome contacts.

HeLa cells expressing VPS13A^mCherry and VPS13C^mClover3 show minimal overlap between the VPS13A and VPS13C signals specifically found on small round structures likely to be lipid droplets (arrowheads in insets). Bar, 10 µm; insets, 10 × 10 µm. **(B)** Cos-7 cells expressing VPS13C^mClover3 or RFP-Sec61β and loaded overnight with dextran Alexa Fluor 647 show VPS13C signal surrounding dextran-positive puncta, which are often surrounded by ER. Arrowheads point to a dextran-negative vesicle enwrapped by ER, likely to be a lipid droplet. Insets, 2.73 × 2.73 µm. **(C)** The majority of full-length VPS13C^mClover3 localizes on Rab7a-RFP–positive structures in Cos7 cells. **(D)** Cos-7 cells expressing VPS13C^mClover3 loaded overnight with 100 µM oleate and then fixed and stained with LipidTox. The figure shows VPS13C signal surrounding LipidTox-labeled spots (lipid droplets at high magnification in the inset) and more intense VPS13C signal around larger vesicular structures likely to be endolysosomal vesicles. Insets, 2.4 × 2.4 µm. **(E–H)** CRISPR/Cas9-edited HeLa cells expressing VPS13A or VPS13C tagged with 2×HA epitopes (endo-HA-VPS13A and endo-HA-VPS13C) at their genomic loci. Cells were transfected with either mito-BFP or EGFP-Rab7a, fixed, and immunostained with anti-HA antibodies (magenta). A large fraction of endo-HA-VPS13A–immunoreactive puncta are localized on mitochondria (E) and not on Rab7-positive vesicles (F). Conversely, a large fraction of endo-HA-VPS13C–immunoreactive puncta are localized on Rab7-positive vesicles (G) and not on mitochondria (H). Bars, 2 µM (B–H).

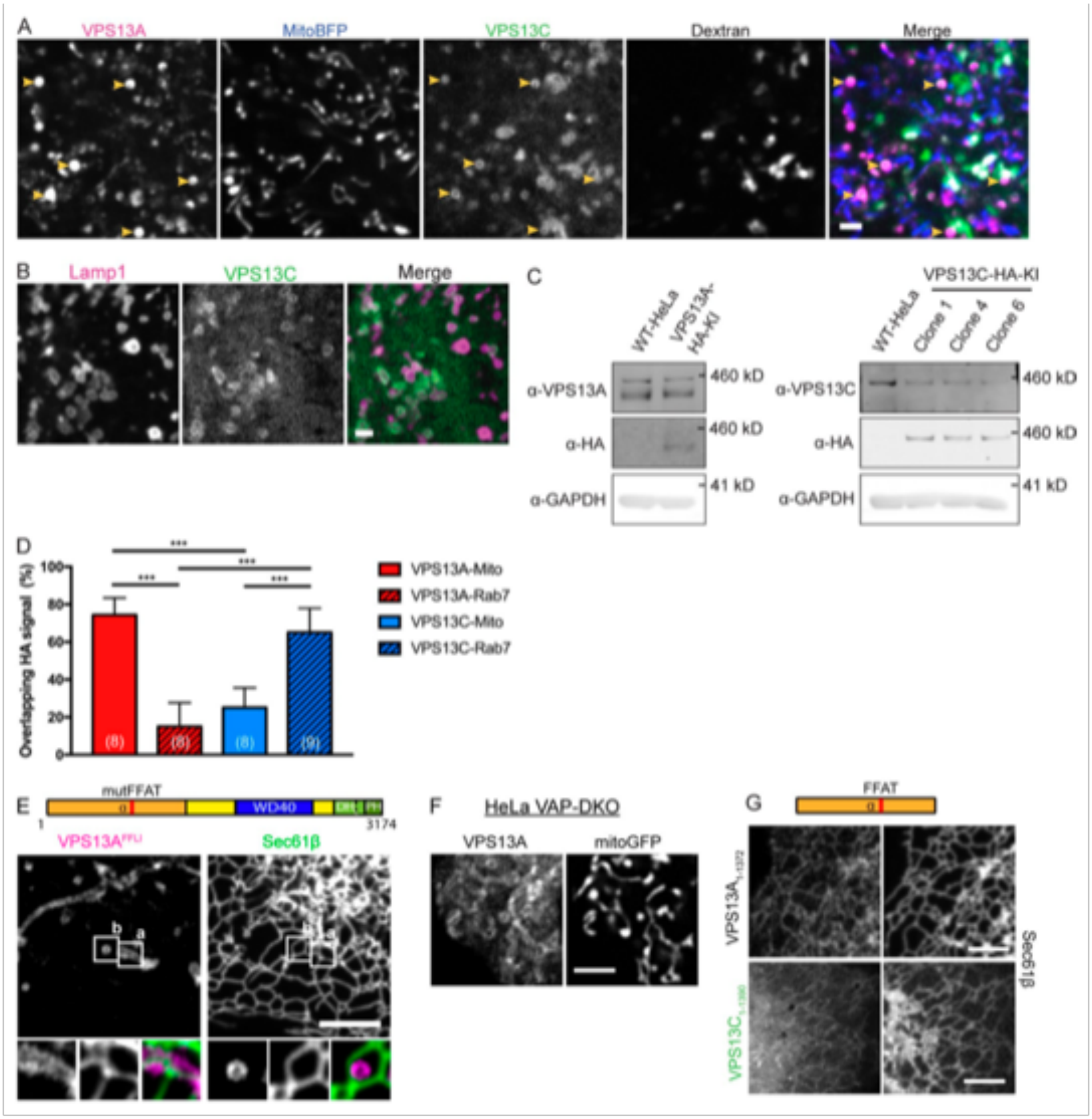

Figure 2.4 VPS13A and VPS13C localizations.

(A) Cos-7 cells expressing VPS13A^Halo, VPS13C^mClover3, and mito-BFP and incubated with dextran Alexa Fluor 647 overnight. The figure shows overlap between the VPS13A and VPS13C signals only on lipid droplets (arrowheads) with no VPS13C present on mitochondria and no VPS13A surrounding dextran-positive puncta. **(B)** Cos-7 cells expressing full-length VPS13C and Lamp1-mRFP showing presence of VPS13C on some Lamp1-positive vesicles. All

Figure 2.4 (Cont.) micrographs were acquired by live-cell imaging, and images shown are representative of at least three independent experiments. Bars, 2 µm. **(C)** Anti-VPS13A, -VPS13C, and -HA Western blots of lysates of CRISPR/Cas9-edited HeLa cells confirming the in-frame insertion of the 2×HA tag in VPS13A and VPS13C. KI, knock-in. **(D)** Quantification of the pixel overlap of VPS13A or VPS13C signal with either mitochondria (mito-GFP) or late endosomes (EGFP-Rab7a). Data are represented as mean ± SD, and groups were compared using ANOVA followed by Tukey's honest significant difference test. ***, $P < 0.001$. Number of cells analyzed are show in parenthesis in each bar. **(E)** Cos-7 cell coexpressing full-length VPS13A bearing a mutant FFAT motif and EGFP-Sec61β. Note that this VPS13A construct homogeneously labels the surface of mitochondria regardless of the presence of the ER (see high magnification of region a below). This construct also labels doughnut-shaped structures negative for the ER (see high magnification of region b below; 2 × 2 µm.). **(F)** WT VPS13A coexpressed with mito-BFP in VAP–double KO (DKO) HeLa cells display a similar lack of ER binding and enrichment on the mitochondrial surface. **(G)** The N-terminal portion of VPS13A and VPS13C localize throughout the ER marked by EGFP-Sec61β, although in the presence of a cytosolic pool. All micrographs were acquired by live-cell imaging, and images shown are representative of at least two independent experiments. Bars, 5 µm.

Expression of tagged protein yields optimal fluorescence signal but may produce artifacts of overexpression. Thus, the localization of VPS13A and VPS13C was further validated by immunostaining HeLa cells in which the corresponding genes were edited to encode proteins with 2×HA epitopes at the same sites used to tag the exogenous proteins (Figure 2.4 C). The analysis of these cells, where VPS13A and VPS13C are expressed at endogenous levels, confirmed the differential localization of the two proteins at sites of contacts between the ER and mitochondria and between the ER and endolysosomes, respectively (Figure 2.3, E–H; and Figure 2.4 D). One difference was that in all cases, only spotlike contacts between the ER and these other organelles were detected, indicating that the more extensive localization of VPS13A and VPS13C at organelle interfaces are due to expansions of these contacts as a result of overexpression.

2.3.2 FFAT motifs in VPS13A and VPS13C mediate tethering of the ER

A function of VPS13A and VPS13C in bridging the ER to other organelles requires the presence of binding sites responsible for these localizations. Bioinformatics analysis of VPS13 revealed a domain organization conserved from yeast to humans. A long N-terminal region of unknown fold (VPS13α) was followed by putative WD40 modules, a domain reminiscent of a DH domain (DH-Like domain; DH_L) and a previously predicted C-terminal pleckstrin homology (PH) domain (Figure 2.5 A; (Fidler et al., 2016)). An FFAT motif, a short amino acid sequence known to interact with the ER VAMP-associated protein (VAP), is present in the Vps13α region of both proteins as previously noted (Murphy and Levine, 2016). Accordingly, full-length VPS13A harboring the FFAT mutation ($VPS13A^{FFLI}$) was no longer tethered to the ER but rather was localized to the entire outer surface of mitochondria and of lipid droplets (Figure 2.4

E). The same localization was observed for WT VPS13A when expressed in VAP-knockout (KO) cells (Figure 2.4 F; (Dong et al., 2016)). Likewise, N-terminal constructs (VPS13α) of both proteins (VPS13A$_{1-1,372}$ and VPS13C$_{1-1,390}$) accumulated over the entire ER, more so upon cotransfection with VAP (VAPB; Figures 2.5 B and 2.4 G), while the same constructs harboring mutations of the FFAT motif (VPS13A$_{1-1,372}^{FFLI}$ and VPS13C$_{1-1,390}^{YFSL}$) had a diffuse cytosolic distribution (Figure 2.5 C). Furthermore, overexpression of VAPB together with VPS13C induced the formation of abnormal ER structures, completely enwrapping all VPS13C-positive endosomes (Figure 2.5 D). These findings not only confirm the role of the FFAT motif in anchoring these proteins to the ER but also indicate that binding sites for mitochondria (in VPS13A), late endosomes/lysosomes (in VPS13C), and lipid droplets (both proteins) are localized in the C-terminal regions of the two proteins.

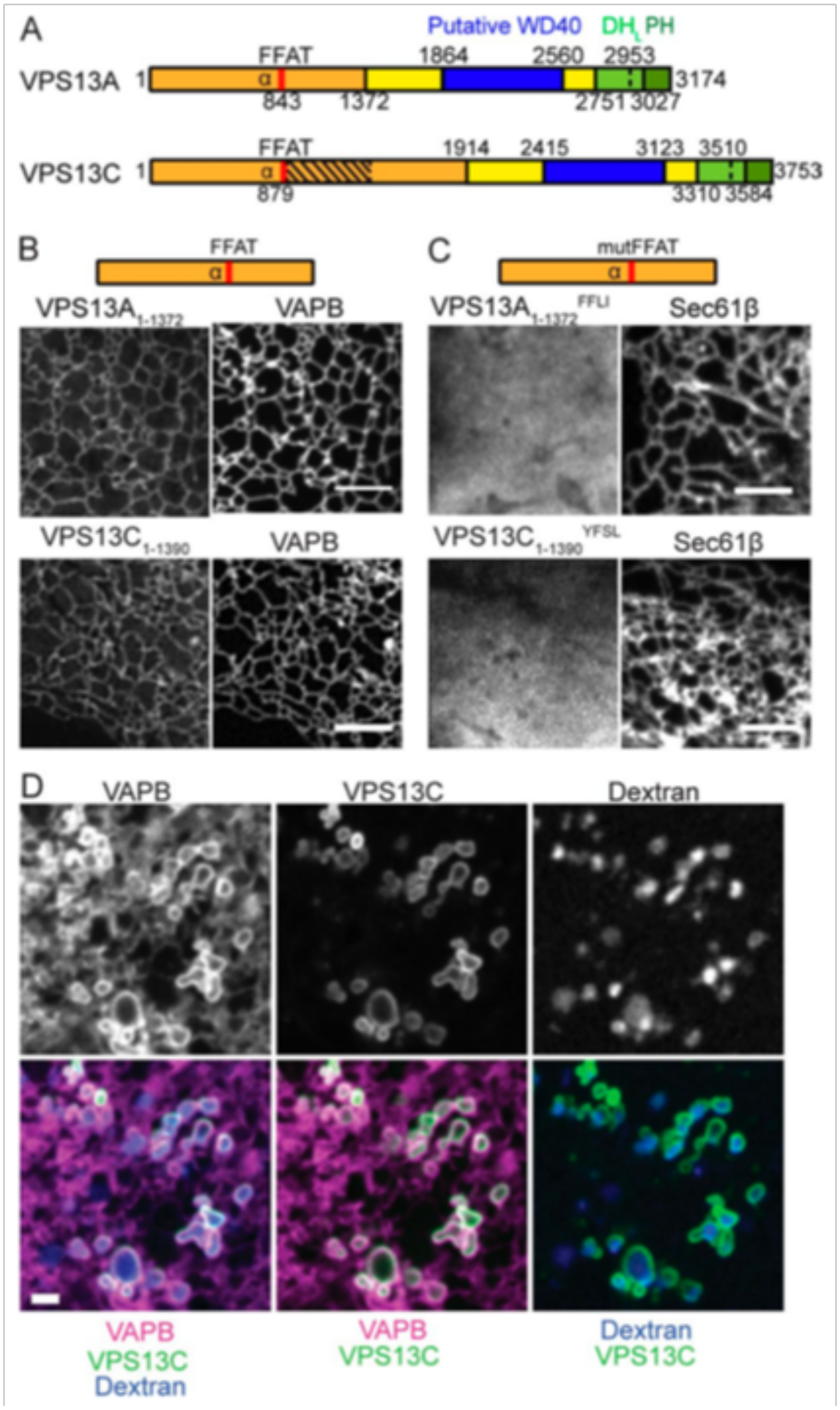

Figure 2.5 The predicted FFAT motif in VPS13A and VPS13C tethers them to the ER. **(A)** Schematic cartoon of the putative domain architecture of human VPS13A and VPS13C. The striped region in VPS13C represent an ~500-residue insertion likely arisen from the internal duplication of the region just upstream of it. The dashed line in the DH$_{L}$ domain defines the start

Figure 2.5 (Cont.) of the ATG homology region (see also Figure 2.8 A). **(B)** Cos-7 cells expressing VPS13A1–1,372-EGFP or VPS13C1–1,390-EGFP and mCherry-VAPB show robust enrichment of VPS13A and VPS13C N-terminal fragments on the ER. **(C)** Corresponding constructs bearing a mutant FFAT motif (VPS13A1–1,372$^{\text{FFLI}}$ and VPS13C1–1,390$^{\text{YFSL}}$) expressed in Cos-7 cells are instead cytosolic. Bar, 5 µm. **(D)** In VAPB-overexpressing cells, VPS13C populates VAP-enriched ER domains that completely surround endocytic vesicles filled with dextran. Bar, 2 µm. All amino acid numbers refer to human proteins.

2.3.3 C-Terminal regions of VPS13A and VPS13C contain binding sites for other organelles

A fragment of VPS13A comprising its entire WD40 region had a cytosolic distribution (Figure 2.7 A), while a corresponding fragment of VPS13C (VPS13C$_{2,415–3,309}$) fragment decorated the entire surface of vesicles positive for dextran (Figure 2.6 A), Rab7 (Figure 2.7 B), or LAMP1 (Figure 2.6 B), thus identifying the WD40 module as the binding site for late endosomes/lysosomes in VPS13C. Further analysis of the localization of deletion constructs of VPS13A and VPS13C identified the DH$_L$-PH domains as (i) the mitochondria-binding region of VPS13A and (ii) the lipid droplet–binding region of both proteins (Figure 2.7 C and D). The DH$_L$-PH domain sequence contains a region of high similarity to ATG2, which also binds lipid droplets (Tamura et al., 2017; Velikkakath et al., 2012). Accordingly, this region alone, fused to EGFP, labeled lipid droplets (Figure 2.7 E). Within this region, an amino acid stretch almost identical in VPS13A (aa 2,993–3,027) and VPS13C (aa 3,550–3,584) is predicted to fold as an amphipathic helix, a structural motif used by some proteins to interact with lipid droplets (Rowe et al., 2016). Mutation of one residue (conserved between VPS13A and VPS13C) on the hydrophobic face of such helix completely abolished its lipid droplet localization (Figure 2.7 F). An additional amphipathic helix was previously predicted within the same region of VPS13A (aa 2,959–2,982; (Drin et al., 2007)) but not in VPS13C and may justify the stronger recruitment on lipid droplets observed for VPS13A with respect to VPS13C.

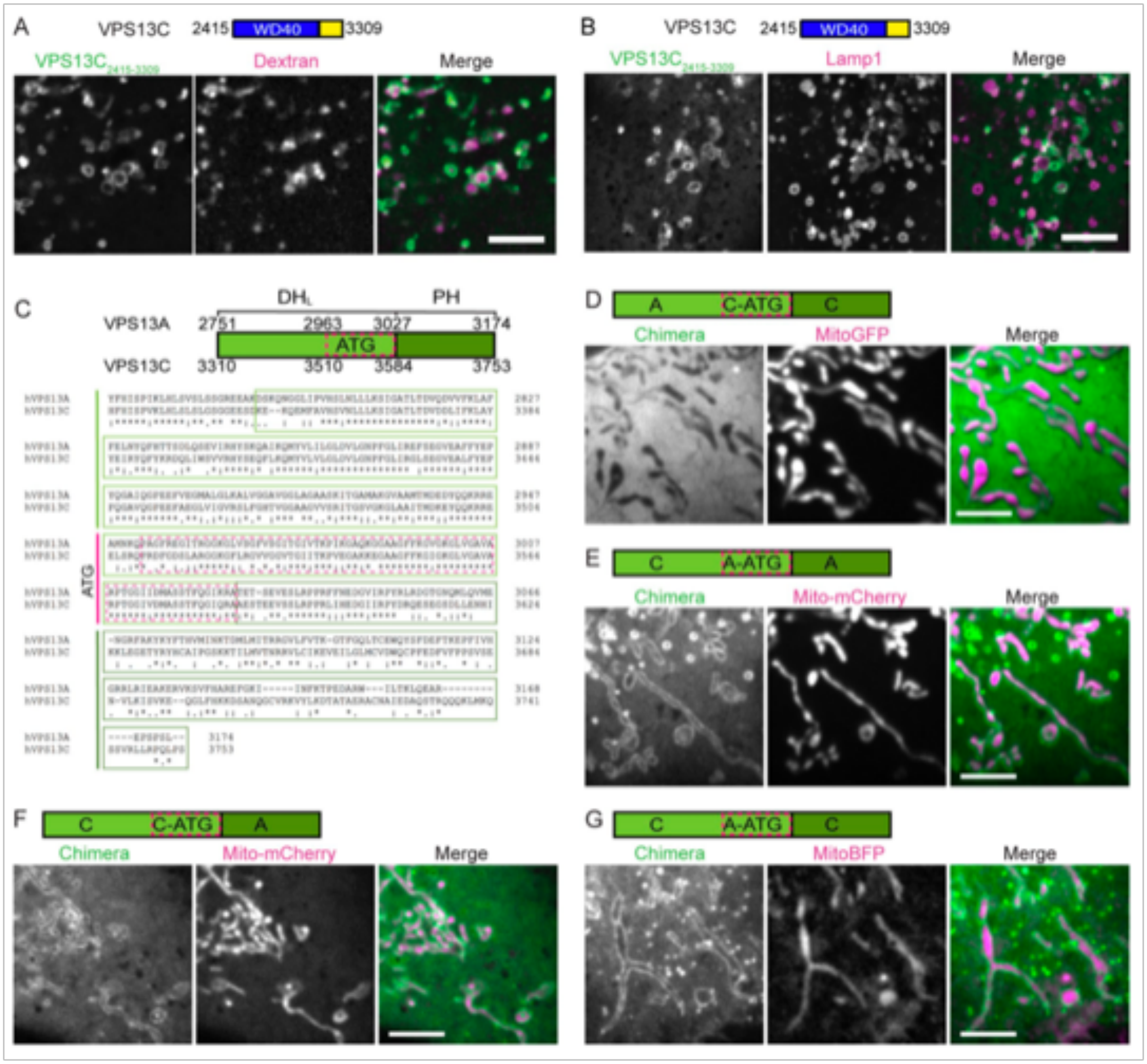

Figure 2.6 Regions of VPS13A and VPS13C that bind mitochondria and late endosomes/lysosomes.

A VPS13C fragment (residues 2,415– 3,309) including the WD40 region surrounds dextran-positive endocytic vesicles (A) and Lamp1-positive vesicles (B). **(C)** Alignment of predicted DHL-PH domains of VPS13A and VPS13C. The borders between regions defined in this figure were used to generate chimeric constructs that were used for the experiments shown in D–G. In the cartoons, the letters A or C denote whether the corresponding regions are from VPS13A or VPS13C, respectively. **(D–G)** Cos-7 cells expressing the indicated mitochondrial marker and the

Figure 2.6 (Cont.) indicated VPS13 chimeric construct fused at the N terminus to either mCherry (D) or mClover3 (E–G). Mitochondrial localization of the construct in E but not of the construct in D mapped the mitochondrial interacting region downstream of aa 2,953. Mitochondria appear as negative images in the VPS13 channel in D due to exclusion of the cytosol. The ability of both the chimeras in F and G to associate with the mitochondrial surface suggests the presence of two independent sequences sufficient for mitochondrial targeting: one in the ATG_C region and one in the PH domain. All micrographs were acquired by live-cell imaging. Bars, 5 µm.

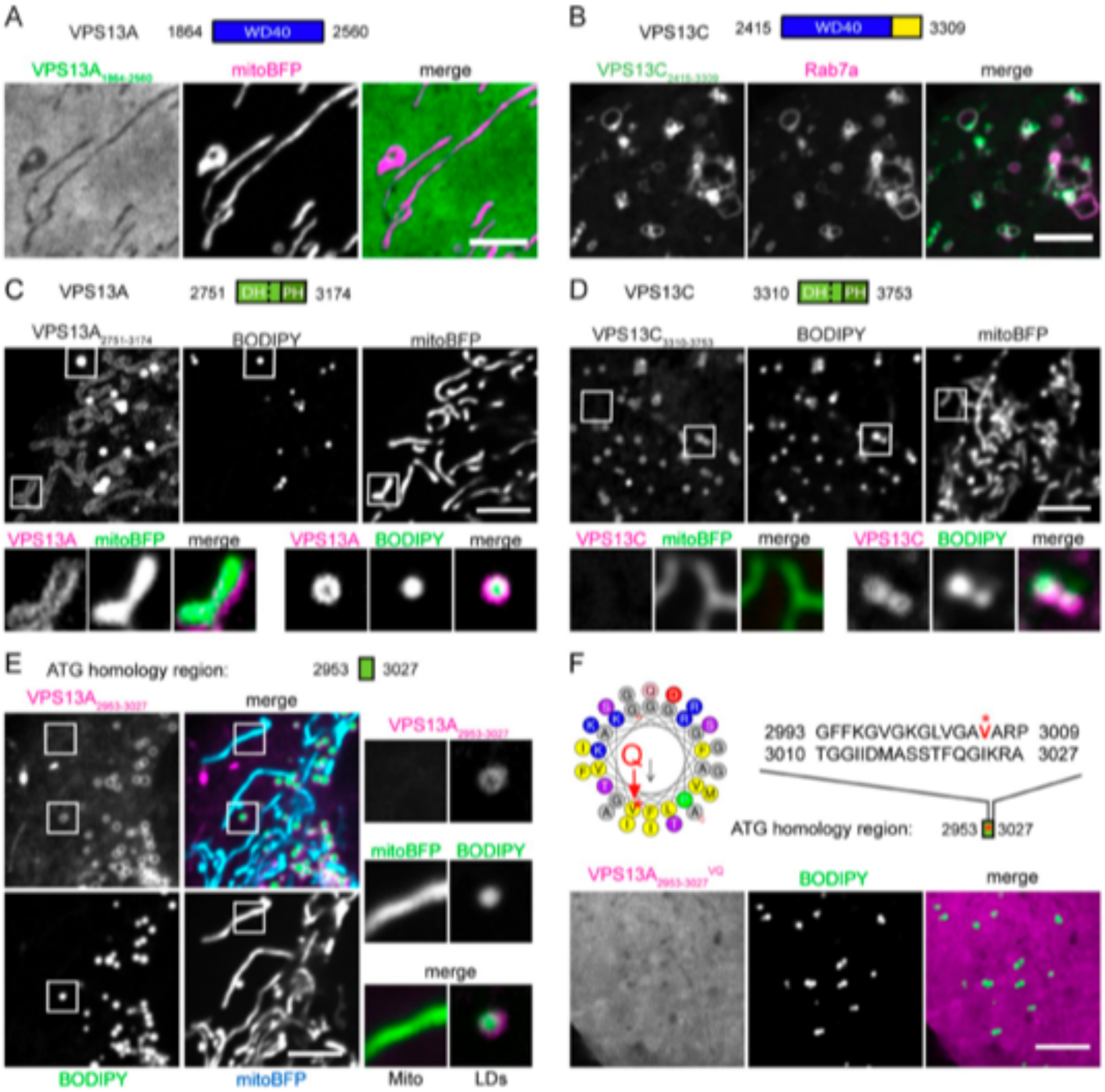

Figure 2.7 Binding regions for mitochondria or late endosomes lie in the C-terminal half of VPS13 proteins.

(A) Cos-7 cells expressing mClover3-VPS13C2,415–3,309 and Rab7a-mCherry show localization of VPS13C signal on Rab7a-positive vesicles. **(B)** EGFP-tagged VPS13A1,864–2,560 has a cytosolic localization with no accumulation at the surface of mitochondria, which appear dark in the EGFP channel due to the exclusion of cytosol. **(C)** Cos-7 cells coexpressing mCherry-tagged VPS13A2,751–3,174 and mito-BFP were incubated with BODIPY 493/503 for

Figure 2.7 (Cont.) lipid droplet (LD) labeling. VPS13A$_{2,751\text{–}3,174}$ fluorescence clearly outlines mitochondria and lipid droplets as shown in high-magnification panels below (2.33 × 2.33 µm). **(D)** Cos-7 cells expressing mClover3-VPS13C$_{3,310\text{–}3,753}$ and labeled with BODIPY 493/503 show VPS13C$_{3,310\text{–}3,753}$ signal surrounding BODIPY-positive puncta (lipid droplets) but not mitochondria as shown in high-magnification panels below (2.33 × 2.33 µm). **(E)** Cos-7 cells coexpressing the mitochondrial marker mito-BFP and an mCherry-tagged VPS13A fragment (VPS13A$_{2,953\text{–}3,027}$) corresponding with the ATG homology region show that this fragment surrounds lipid droplets (labeled with BODIPY 493/503) but not mitochondria. Regions indicated by the white squares are shown in high magnification on the right (2.33 × 2.33 µm). **(F)** Representation of the predicted helical arrangement of residues 2,993–3,010 of VPS13A generated via the HeliQuest tool (heliquest.ipmc.cnrs.fr; (Gautier et al., 2008). An mCherry-tagged VPS13A$_{2,953\text{–}3,027}$ construct bearing a single amino acid substitution (V3006Q; indicated by an asterisk) in the hydrophobic face of the predicted amphipathic helix had a cytosolic localization. All micrographs were acquired by live-cell imaging, and images shown are representative of at least two independent experiments. Bars, 5 µm. All amino acid numbers refer to human proteins.

A more precise identification of the mitochondria-binding region of VPS13A was achieved by generating chimeric constructs containing subdomains of the $\mathrm{DH_L}$-PH region from VPS13A and VPS13C (Figure 2.6 C). This demonstrated that both the ATG homology region and the PH domain of VPS13A are sufficient to drive mitochondrial localization (Figure 2.6, D–G), suggesting a bipartite binding site. This site resides downstream of the region shown to mediate binding to mitochondria in yeast Vps13. However, as the yeast mitochondrial Vps13 interactor MCP1 (John Peter et al., 2017) is not conserved in mammals, a nonconserved mode of binding to mitochondria appears likely.

2.3.4 The N-terminal portion of VPS13 has lipid transport properties

The localization of at least two VPS13 isoforms at organelle contact sites is consistent with a potential conserved role of VPS13 family proteins in lipid transport between adjacent organelles. Thus, we next tested directly the possibility that Vps13 might bind and transport lipids. Vps13 is a large protein (molecular weight > 340 kD), and so far, we could not produce full-length proteins from either humans or other organisms in sufficient quantities for biochemical analysis. Thus, we used VPS13 fragments. As the predicted WD-40, $\mathrm{DH_L}$, and PH domains are unlikely lipid transport modules, we focused on the N-terminal region Vps13α (Figure 2.8 A), whose structure and function were unknown. Not only is Vps13α well conserved within the VPS13 family across species, but the most N-terminal region (Chorein_N domain) shows homology with other proteins including ATG2 (De et al., 2017).

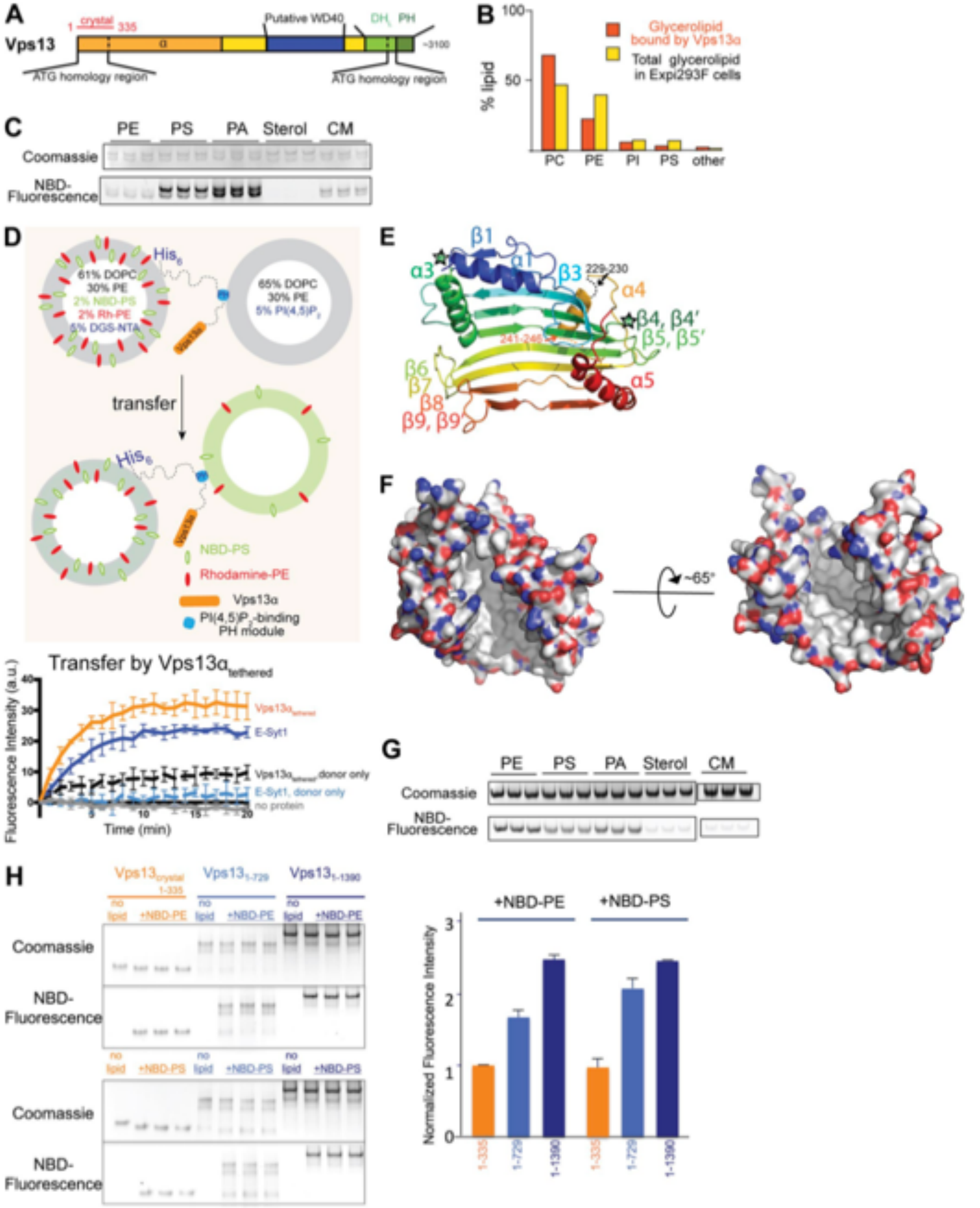
A
Vps13
1 crystal 335
α
Putative WD40
DH PH
~3100
ATG homology region
ATG homology region
B
% lipid
100
50
Glycerolipid bound by Vps13α
Total glycerolipid in Expi293F cells
PC
PE
PI
PS
other
C
PE
PS
PA
Sterol
CM
Coomassie
NBD-Fluorescence
D
His6
61% DOPC
30% PE
2% NBD-PS
2% Rh-PE
5% DGS-NTA
65% DOPC
30% PE
5% PI(4,5)P2
transfer
NBD-PS
Rhodamine-PE
Vps13α
PI(4,5)P2-binding PH module
Transfer by Vps13αtethered
Fluorescence Intensity (a.u.)
40
30
20
10
0
5
10
15
20
Time (min)
Vps13αtethered
E-Syt1
Vps13αtethered donor only
E-Syt1, donor only
no protein
E
β1
α1
α3
β3
229-230
α4
β4, β4′
β5, β5′
241-246
β6
β7
β8
β9, β9′
α5
F
~65°
G
PE
PS
PA
Sterol
CM
Coomassie
NBD-Fluorescence
H
Vps13crystal 1-335
Vps13 1-729
Vps13 1-1390
no lipid
+NBD-PE
no lipid
+NBD-PS
Coomassie
NBD-Fluorescence
Coomassie
NBD-Fluorescence
+NBD-PE
+NBD-PS
Normalized Fluorescence Intensity
3
2
1
0
1-335
1-729
1-1390
1-335
1-729
1-1390

Figure 2.8 N-terminal portions of Vps13 solubilize and transport lipids.

(A) Schematic of VPS13 domain architecture. The crystallized fragment from C. thermophilum is indicated. **(B)** LC/MS/MS analysis of lipids that copurify with Vps13α showed binding to glycerolipids, with a slight preference for PC. Cellular abundance of these glycerolipids is indicated (Lees et al., 2017). Sphingomyelin represented 1% of bound lipids. No sterol, di-, or triacylglycerides were detected. **(C)** Vps13α was incubated with NBD-tagged lipid including NBD-ceramide (CM) and then examined by native PAGE. Phospholipids, which were visualized by their fluorescence, comigrated with protein, visualized by Coomassie staining. **(D)** Donor liposomes (25 μM) containing fluorescent lipids (2% NBD-PS, 2% NBD-PE, 5% DGS-NTA, 61% DOPC, and 30% PE) were mixed 1:1 with acceptor liposomes (25 μM: 65% DOPC, 30% PE, and 5% PI(4,5)P2) in the presence or absence of Vps13αtethered (0.125 μM). This construct tethers the Vps13α fragment between acceptor and donor liposomes via a PI(4,5)P2-specific PH domain and a C-terminal hexahistidine sequence. The assay monitors the increase in NBD-PS fluorescence after lipid transfer from donor liposomes, where NBD fluorescence is quenched via FRET with Rhodamine-PE, to acceptor liposomes. The fluorescence increase observed is consistent with lipid transfer at a rate similar to that for

We were successful in purifying Vps13α from Saccharomyces cerevisiae (residues 1–1,350) and showed by negative-stain EM that it forms monomeric or dimeric rods, although the dimeric forms may not occur for the full-length protein (Figure 2.9 A and B). Potential lipid content of this fragment, expressed in Expi293F cells and affinity purified, was assessed by liquid chromatography–tandem mass spectrometry (LC/MS/MS). Vps13α bound to glycerophospholipids but not other lipid species, with enrichment of PC relative to the glycerolipid content of cellular membranes (Figure 2.8 B). Despite rigorous washes of the protein before lipid analysis, there were ∼10 glycerolipids associated per protein molecule. This indicates that Vps13α might bind multiple lipid molecules at once, consistent with studies described below. Further supporting that the protein harbors phospholipids, Vps13α comigrated with the fluorescently labeled lipids NBD-PS and NBD-PA and to a lesser extent with NBD-phosphatidylethanolamine (PE) and NBD-ceramide on a native gel (Figure 2.8 C).

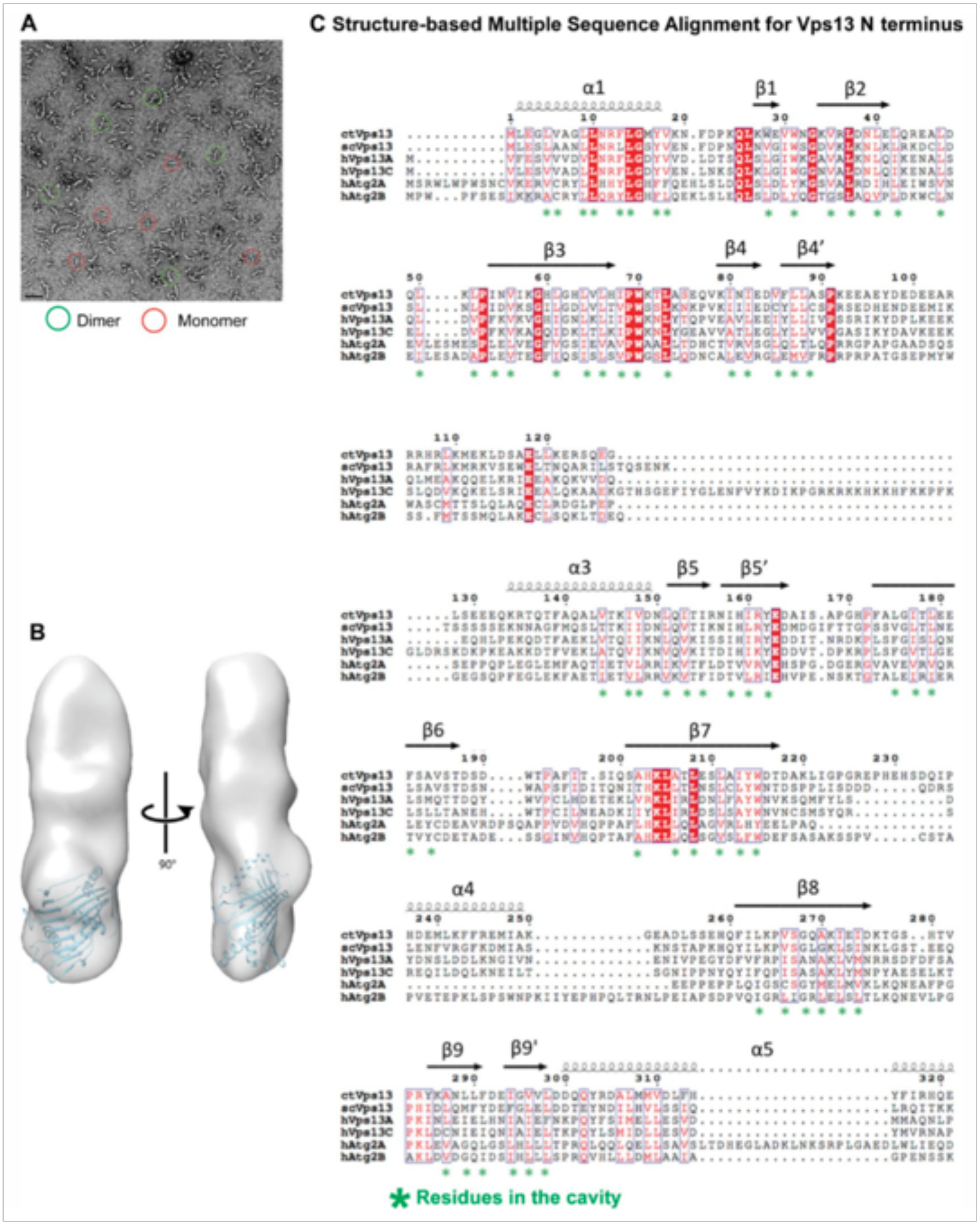
A
Dimer
Monomer
B
90°
C Structure-based Multiple Sequence Alignment for Vps13 N terminus
α1
β1
β2
β3
β4
β4′
α3
β5
β5′
β6
β7
α4
β8
β9
β9′
α5
ctVps13
scVps13
hVps13A
hVps13C
hAtg2A
hAtg2B
Residues in the cavity

Figure 2.9 Low-resolution characterization of the VPS13 N-terminal region.

(A) S. cerevisiae Vps13α (residues 1–1,350) was diluted to 50–100 nM in buffer (20 mM Hepes, pH 7.8, 300 mM NaCl, and 1 mM TCEP) immediately before staining. Vps13 (5 µl) was added onto glow-discharged copper grids covered in a thin layer of carbon and stained with 2% uranyl acetate. The grids were imaged using a Tecnai T12 electron microscope (FEI) with an operation voltage of 120 kV at a 67,000× magnification. Vps13α appears as monomers or dimers as indicated. **(B)** A total of 135 micrographs of purified S. cerevisiae Vps13$_{1–1,350}$ were collected at a nominal magnification of 52,000× (pixel size of 2.14 Å on the specimen level) and a defocus of −1.5 µm on a Tecnai T12 microscope operated at 120 kV. 36,905 particles picked in Relion 2.1 were classified into 200 2D classes, after which classes yielding poor averages were removed. The remaining 30,890 particles were reclassified into 100 2D classes, of which the best 12 (comprising 30,380 particles) were selected for initial model calculation by stochastic gradient descent as implemented in Relion 2.1.0. The resulting model was used as a template for 3D classification into four classes. The largest class, comprising 10,068 particles, was refined in Relion, reaching 21.7 Å resolution based on gold-standard Fourier shell correlation with a cutoff of 0.143. Vps13$_{\text{crystal}}$ is docked into the reconstruction to demonstrate that its diameter is similar to that of Vps13α. For comparison, a reconstruction of the full-length protein is reported by (De et al., 2017). **(C)** Secondary structure in Vps13$_{\text{crystal}}$ and a structure-based alignment for the N-terminal portions of VPS13 from S. cerevisiae, C. thermophilum, or humans (isoforms A and C) and human ATG2A and ATG2B. Structure-based sequence alignments were generated using the PROMALS3D web server (Pei et al., 2008) and rendered with ESPript 3.0 (Robert and Gouet, 2014). Columns containing 100% identical residues are highlighted red. Columns containing >70% equivalent residues are colored red, and columns containing identical or >70%

Figure 2.9 (Cont.) equivalent residues are boxed in blue. Green asterisks indicate residues within the cavity of the Vps13$_{\text{crystal}}$ construct, which are hydrophobic in all sequences.

We used these observations in designing a FRET-based in vitro assay to interrogate whether Vps13α can transfer lipids between membranes. We mixed donor liposomes containing DGS-NTA, NBD-PS, and rhodamine-PE with acceptor liposomes containing PI(4,5)P_2 and lacking fluorescent labeling, and then we added Vps13α_{tethered}. In this chimeric construct, the Vps13α fragment is tethered to the liposomes via a C-terminal hexahistidine sequence that interacts with DGS-NTA on the donor liposomes and an upstream N-terminal PH module that interacts with PI(4,5) P_2 on the acceptor liposomes (Figure 2.8 D and Figure 2.10, A and B). Initially, FRET between NBD and rhodamine in the donor liposomes quenched NBD fluorescence. If either NBD-PS or rhodamine-PE or both were transported to acceptor liposomes, the fluorophores were diluted, and the distance separating them increased, leading to decreased FRET and an increase in NBD fluorescence (Figure 2.8 D and Figure 2.10 A; (Saheki et al., 2016; Struck et al., 1981; Yu et al., 2016)).

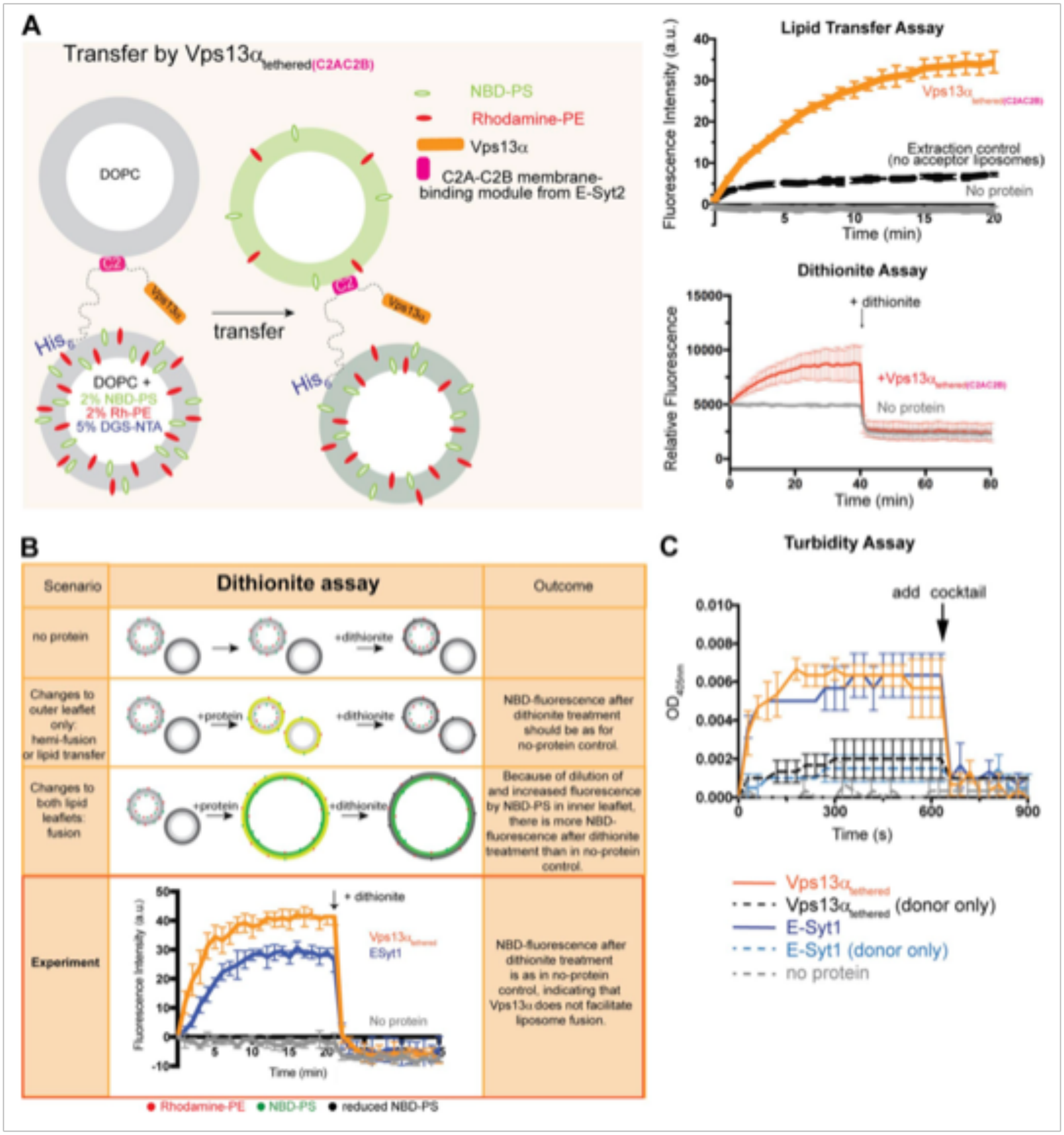

Scenario	Dithionite assay	Outcome
no protein	+dithionite	
Changes to outer leaflet only: hemi-fusion or lipid transfer	+protein +dithionite	NBD-fluorescence after dithionite treatment should be as for no-protein control.
Changes to both lipid leaflets: fusion	+protein +dithionite	Because of dilution of and increased fluorescence by NBD-PS in inner leaflet, there is more NBD-fluorescence after dithionite treatment than in no-protein control.
Experiment		NBD-fluorescence after dithionite treatment is as in no-protein control, indicating that Vps13α does not facilitate liposome fusion.

Figure 2.10 Lipid transfer assays: Vps13α does not promote membrane fusion or hemifusion.

(A) Lipid transfer experiment as in Figure 2.8 D but with a different tethering strategy and liposome compositions. Donor liposomes (50 μM) containing fluorescent lipids (2% NBD-PS, 2% NBD-PE, 5% DGS-NTA, and 91% DOPC) were mixed 1:1 with acceptor liposomes (50 μM

Figure 2.10 (Cont.) DOPC) in the presence or absence of Vps13α$_{\text{tethered-C2AC2B}}$ (1 μM). This construct tethers the Vps13α fragment between acceptor and donor liposomes via a membrane-binding module (C2A-C2B domains of Extended-Synaptotagmin2) and a C-terminal hexahistidine sequence. The assay was performed in the presence of calcium (1 μM), which allows C2A-C2B to associate with membranes in either donor or acceptor liposomes (Bian et al., 2018; Saheki et al., 2016; Yu et al., 2016). A dithionate assay as in B ruled out that Vps13α$_{\text{tethered-C2AC2B}}$ mediates liposome fusion. **(B)** The dithionite assay (Shi et al., 2013; Weber et al., 1998) shows that Vps13α$_{\text{tethered}}$ does not promote liposome fusion. In this assay, dithionite was added to the liposomes after the lipid transfer/mixing reaction. Dithionite reduced NBD-PS in the exposed outer leaflet of liposomes, abrogating its fluorescence, but did not affect NBD-PS in the inner leaflet. The fluorescent signal after dithionite treatment should have been the same as in the no-protein control in the cases of Vps13α-mediated lipid transport or hemifusion, where NBD-PS was redistributed between the outer leaflets of liposomes. In contrast, the signal was expected to be larger if liposomes had fused and thus NBD-PS concentrations in the inner leaflet of the liposomes had changed. **(C)** The turbidity before and after the transfer assay was the same, indicating that VPS13$_{\text{tethered}}$ does not facilitate either fusion or hemifusion. Increased turbidity during the reaction was due to tethering and was reversed upon addition of cocktail comprising imidazole and proteinase K. All experiments were performed in triplicate. SD is indicated.

In the transfer assay, NBD fluorescence increased after addition of Vps13α_{tethered}, consistent with a role for Vps13α in lipid transfer. Fluorescence increase was not due to fusion or hemifusion between donor and acceptor liposomes as the increase in turbidity of the liposome mixture after addition of Vps13α_{tethered} (due to the clustering of liposomes induced by this construct) was rapidly reversed by the addition of a protease (Figure 2.10). The fluorescence increase was due to lipid transfer by Vps13 and not to extraction from donor liposomes only, as in the absence of acceptor liposomes, i.e., in an extraction-only scenario, the assay resulted in a much smaller increase of fluorescence (Figure 2.8 D). Similar results were obtained by replacing Vps13α in the tethering construct with the lipid transport module of Extended-Synaptotagmin (Schauder et al., 2014; Yu et al., 2016), which served as a positive control (Figure 2.8 D). Thus, in vitro transfer assays showed that Vps13α can transfer glycerolipids between membranes in vitro. Since both the Extended-Synaptotagmins and Vps13α bind and thus likely also transport glycerolipids like PC and PE ((Schauder et al., 2014); see also LC/MS/MS analysis above), the major constituents of liposomes in the assay, overall lipid transfer by these proteins may be much faster than that observed for fluorescent lipids only.

2.3.5 The N-terminal region of VPS13 contains a hydrophobic cavity

Sequence similarity between the N-terminal regions of VPS13 and the autophagy protein ATG2 (De et al., 2017; Pfisterer et al., 2014) hinted that these proteins might share a common module at their N termini and guided construct design for structural studies. After crystallization trials with VPS13 N-terminal fragments from various species, we succeeded in crystallizing a fragment comprising residues 1–335 (Vps13$_{\text{crystal}}$) from the fungus Chaetomium thermophilum, and we solved its structure to a resolution of 3.0 Å using the single-wavelength anomalous dispersion method (Hendrickson, 1991). A poorly conserved, predicted loop (residues 228–236) was truncated to facilitate crystallization. Data collection and refinement statistics are in Table 2.1.

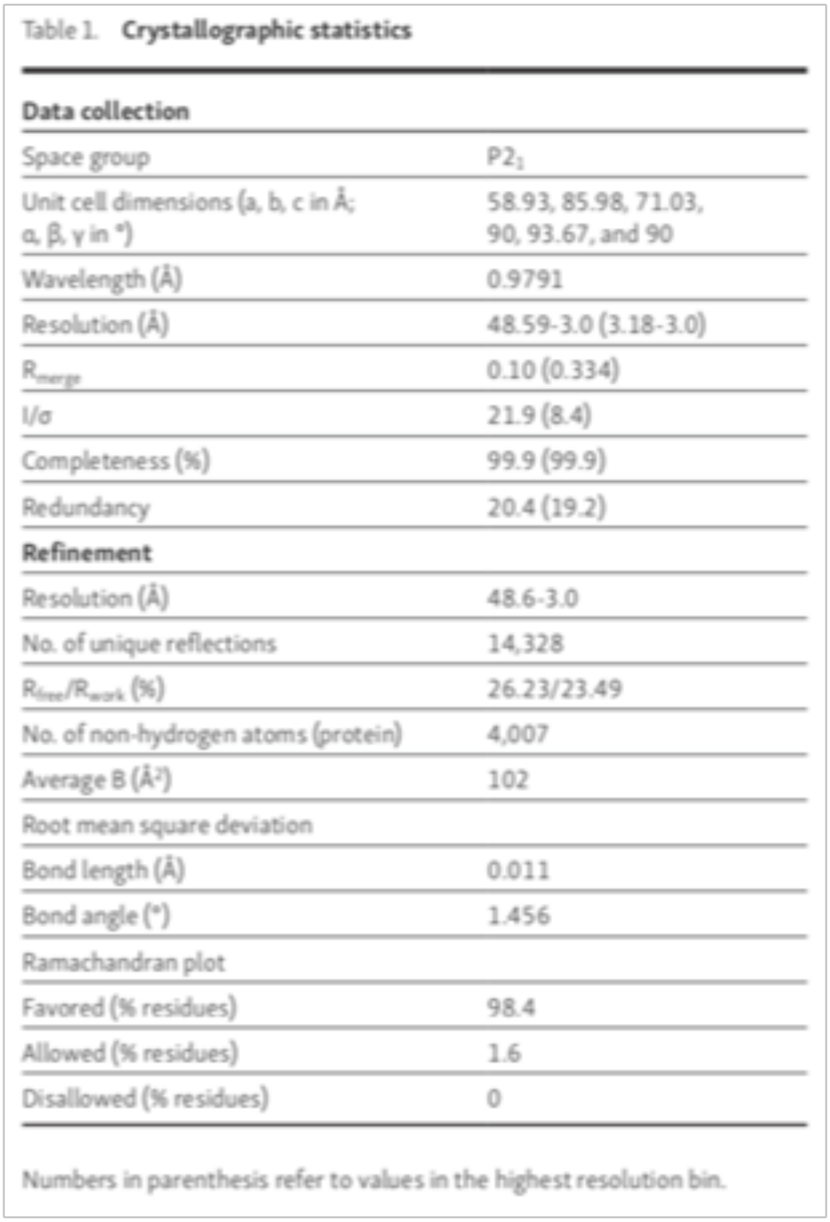

Table 1. **Crystallographic statistics**

Data collection	
Space group	$P2_1$
Unit cell dimensions (a, b, c in Å; α, β, γ in °)	58.93, 85.98, 71.03, 90, 93.67, and 90
Wavelength (Å)	0.9791
Resolution (Å)	48.59-3.0 (3.18-3.0)
R_{merge}	0.10 (0.334)
I/σ	21.9 (8.4)
Completeness (%)	99.9 (99.9)
Redundancy	20.4 (19.2)
Refinement	
Resolution (Å)	48.6-3.0
No. of unique reflections	14,328
R_{free}/R_{work} (%)	26.23/23.49
No. of non-hydrogen atoms (protein)	4,007
Average B (Å^2)	102
Root mean square deviation	
Bond length (Å)	0.011
Bond angle (°)	1.456
Ramachandran plot	
Favored (% residues)	98.4
Allowed (% residues)	1.6
Disallowed (% residues)	0

Numbers in parenthesis refer to values in the highest resolution bin.

Table 1: Crystallographic statistics

Vps13$_{\text{crystal}}$ folds to resemble a utility scoop lacking the handle, and based on DALI searches of the Protein Database, it bears no significant structural similarity to any previously characterized protein (Figure 2.8 E and Figure 2.10 C). N-terminal α-helices (α1 and α3) help to cap one end of the scoop, whereas loops and the most C-terminal α-helix (α5) define its edges. β-strand elements form the scoop base, whose convex backside is buttressed by helix α4. A long predicted helical segment (α2), which connects strand β4' to helix α3 (residues marked by stars in Figure 2.8 E) and thus must extend over and partially cover the concave face of the scoop, was not ordered in the crystal and was not modeled. While the convex backside of Vps13$_{\text{crystal}}$ is covered by hydrophilic residues, the concave face is lined exclusively by hydrophobic residues (Figure 2.8 F) and is therefore well suited for solubilizing hydrophobic fatty acyl chains of phospholipids. The hydrophobic cavity of Vps13$_{\text{crystal}}$, measuring ∼20 Å across, has approximately twice the diameter of the cavity of previously studied lipid transporters and so could accommodate several lipid molecules simultaneously.

Indeed, Vps13$_{\text{crystal}}$ retains some of the lipid-binding abilities of Vps13α (Figure 2.8 G). Secondary structure predictions are consistent with the presence of at least two more Vps13$_{\text{crystal}}$-like modules in the N-terminal portions of Vps13. To compare the number of fluorescent lipids bound by Vps13$_{\text{crystal}}$ versus longer constructs twice or four times its size (Vps13$_{1–729}$ comprising residues 1–729 or Vps13$_{1–1,390}$ comprising residues 1–1,390 of C. thermophilum Vps13), we used gel-shift experiments as described above. We found that Vps13$_{1–729}$ and Vps13$_{1–1,390}$ bind approximately twice and 2.5 times as many fluorescent lipids as Vps13$_{\text{crystal}}$ (Figure 2.8 H). Thus, we propose that Vps13$_{\text{crystal}}$ is part of a larger lipid-binding unit in the intact protein. Full-length Vps13 could harbor several Vps13$_{\text{crystal}}$-like modules, or alternatively, Vps13$_{\text{crystal}}$ could be part of an elongated tube reminiscent of lipid transporters like ERMES or bacterial lipopolysaccharide transporter complexes (AhYoung et al., 2015; Sherman et al., 2018). Vps13$_{\text{crystal}}$ could form one end of a tubular structure running the length of the Vps13α rod since their diameters match (Figure 2.9 B). The secondary structure predictions for Vps13 are consistent with either model (Figure 2.11).

	ScVps13	CtVps13	hVPS13A	hVPS13C
ScVps13	100	33	21	21
CtVps13	50	100	23	21
hVPS13A	37	39	100	45
hVPS13C	36	39	59	100

Based on MSA:

```
ScVps13 M-LESLAANLLNRLLGSYVENFDPNQLNVGIWSGDVKLKNLKLRKDCLDSLNLPIDVKSGILGDLVLTVPWSSLKNKPVK   79 IIIEDCYLLCSPRSEDHENDEEMIKRAFRLKMRKVSEWELTNQARILSTQSENK--------------------------  133
CtVps13 M-LEGLVAGLLNRFLGMYVKNFDPKQLKWEVWNGKVRLDNLELQREALDQLKLPINVIKGHLGHLVLHIPWKTLASEQVK   79 INIEDVFLLASPKEEAEYDEDEEARRRHRLKMEKLDSAELLKERSQEGLSEE----------------------------  131
hVps13A MVFESVVVDVLNRFLGDYVVDLDTSQLSLGIWKGAVALKNLQIKENALSQLDVPFKVKVGHIGNLKLIIPWKNLYTQPVE   80 AVLEEIYLLIVPSSRIKYDPLKEEKQLMEAKQQELKRIEEAKQKVVDQEQHLPE--------------------------  134
hVps13C MVLESVVADLLNRFLGDYVENLNKSQLKLGIWGGNVALDNLQIKENALSELDVPFKVKAGQIDKLTLKIPWKNLYGEAVV   79 ATLEGLYLLVVPGASIKYDAVKEEKSLQDVKQKELSRIEEALQKAAEKGTHSGEFIYGLENFVYKDIKPGRKRKKHKKHF  160
SS        hhhhhhhhhhhhhhhhhh   hhheeeeee  eeeeeee   hhhhhh    eeeeeeeeeeeeeeeeee      ee      eeee eeeeeee       hhhhhhhhhhhhhhhhhhhhhhhhhhhhhhh

ScVps13 ---------TSSSSSEKNNAGFMQSLTTKIIDNLQVTIKNIHLRYEDMDGIFTTGPSSVGLTLNELSAVSTDSNWAPSFI  204 DITQNITHKLLTLNSLCLYWNTDSPPLISDDD---------QDRSLENFVRGFKDMIA-SKNSTAPKHQYILKPVSGLGK  274
CtVps13 --------------EQKRTQTFAQALVTKIVDNLQITIRNIHIRYED-AISAPGHPFALGITLEEFSAVSTDSDWTPAFI  196 TSIQS-AHKLATLESLAIYWDTDAKLIGPGREPHEHSDQIPHDEMLKF----FREMIAKGEADLSSEHQFILKPVSGQAK  271
hVps13A -----------------KQDTFAEKLVTQIIKNLQVKISSIHIRYED-DITNRDKPLSFGISLQNLSMQTTDQYWVPCLH  196 DETEKLVRKLIRLDNLFAYWNVKSQMFYLSD----------YDNSLDD----LKNGIV-NENIVPEGYDFVFRPISANAK  261
hVps13C KKPFKGLDRSKDKPKEAKKDTFVEKLATQVIKNVQVKITDIHIKYED-DVTDPKRPLSFGVTLGELSLLTANEHWTPCIL  239 NEADKIIYKLIRLDSLSAYWNVNCSMSYQRS----------REQILDQ----LKNEIL-TSGNIPPNYQYIFQPISASAK  304
SS                        hhhhhhhhhhhhh  eeeeeeeeeeeeeee        eeeeeeeeeeeeeee                    eeeeeeee  eeeee   hhh                   hhhhhhhhhhh             eeeeeeeeeee

ScVps13 LSINKLGSTE-EQPHIDLQMFYDEFGLELDDTEYNDILHVLSSIQLRQITKKFKKARPS-FAVSENPTEWFKYIAACVIN  352 -EIHEKNKMWTWESMKEKCEQRRLYTKLWVEKLKLKNLEAPLRDPIQEAQLSELHKDLTYDEIILFRSVAKRQYAQYKLG  431
CtVps13 IEIDKTGSH--TVPRYKANLLFDEIGVVLDDQQYRDALMMVDLFHYFIRHQEYKKFQPKGVTPKEDPRAWFRFAGNAVLS  349 -KIHERNRRWSWDYFRERRDDRRRYIELFKKTKQNIQLTPEER-----EDLDKLEWKLSYEDLRFWRSLARNQLKKENAE  423
hVps13A LVMNRRSDFDFSAPKINLEIELHNIAIEFNKPQYFSIMELLESVDMMAQNLPYRKFKPD-VPLHHHAREWWAYAIHGVLE  340 VNVCPRLWMWSWKHIRKHRQKVKQYKELYKKKLTSKKPPGELL-----VSLEELEKTLDVFNITIARQTAEVEVKKAGYK  415
hVps13C LYMNPYAESELKTPKLDCNIEIQNIAIELTKPQYLSMIDLLESVDYMVRNAPYRKYKPY-LPLHTNGRRWWKYAIDSVLE  383 VHIRRYTQMWSWSNIKKHRQLLKSYKIAYKNKLTQSKVSEEIQ-----KEIQDLEKTLDVFNIILARQQAQVEVIRSGQK  458
SS      eee           eeeeeeeeeeeeeee hhhhhhhhhhhhhhhhhhhhhhhhhh          hhhhhhhhhhhhhh       hhhhhh    hhhhhhhhhhhhhhhhhhhhh       hhh  hhhhhhhhhhhhh  hhhhhhhhhhhhhhhhhhhhh

ScVps13 MTEDSPTPTASSNIEPQTSNKSATKNNGSWLSSWWNGKPTEEVDE---------DLIMTEEQRQELYDAIEFDENEDKGP  502 VLQVPRERVELRVTSLLKKGSFTIRKKKQ--NLNLGSIIFENCKVDFAQRP--DSFLSSFQLNKFSLED-GSPNALYKHI  577
CtVps13 ALKNKP--------------PPQPQQQQGWLSWVWGSKPVQPQQEEQQGDENTR---ITEAQRKELYEVIQWDEKAALAA  486 EIDVPRDSVRLLIETSLSTGSFTLRQNPHGDARDLISLHFDLFRAKGLTRP--DSFLIDISLGGFRVNDNTTPDSLYKEI  564
hVps13A IYKEGV---------------KDPEDNKGWFSWLWSWSEQNTNEQQPDVQPETLEEMLTPEEKALLYEAIGYSETAVD--  478 -PTLLKTFEALKFFVHLKSMSIVLRENHQ--KPELVDIVIEEFSTLIVQRPGAQAIKFETKIDSFHITGLPDNSEKPRLL  555
hVps13C LRKKSA---------------DTGEKRGGWFSGLWGKKESKKKDEESLI-PETIDDLMTPEEKDKLFTAIGYSESTHN--  520 -LTLPKQYVAHIMTLKLVSTSVTIRENKN--IPEILKIQIIGLGTQVSQRPGAQALKVEAKLEHWYITGLRQQDIVPSLV  597
SS      h                                                          hhhhhhhhhh                        eeeeeeeeee   eeeeee     eeeeeeeee   eeeeee      eeeeeee eeeee         eee

ScVps13 ISVRNSSKDQSSIDNHATGEEEEEDEP-LLRASFELNPLDGLADSNLNIKLLGMTVFYHVHFITEVHKFFKASNQHMETI  656 GNIVNAAEATVEGWTTQTRMGIESLLEDHKTVNVSLDLQAPLIILPLD-PHDWDTPCAIIDAGHMSILSDLVPKEKIKEI  735
CtVps13 VRVKDAPNTEGQKRYSIADLELTVDEEAFFELQVEQHPLDGQGDVAVTMKLKPLEIIWNPNVVVGIADFFRPPERHMESI  644 NALLETANATVEGLRAQTRAGLQFALEEHKTVNAKLDLQAPLIILPES-ITTPNSTCLIVDAGHISVNSELVDKETMKQV  723
hVps13A SSLDDAMS--------------------LFQITFEINPLDETVSQRCIIEAEPLEIIYDARTVNSIVEFFRPPKE--VHL  613 AQLTAATLTKLEEFRSKTATGLLYIIETQKVLDLKINLKASYIIVPQDGIFSPTSNLLLLDLGHLKVTS--------KSR  685
hVps13C ASIGDTTSS-------------------LLKIKFETNPEDSPADQTLIVQSQPVEVIYDAKTVNAVVEFFQSNKG--LDL  656 EQITSATLMKLEEIKERTATGLTHIIETRKVLDLRINLKPSYLVVPQTGFHHEKSDLLILDFGTFQLNS-----------  725
SS      eee                 hh      eeeeeee         eeeeeeeeeeeeee hhhhhhhhhh   hhhhhhhh      hhhhhhhhhhhhhhhhhhhhhhhhhhh   eeeeeee    eeee          eeeeee  eeee        hhhhh

ScVps13 KELSPEEYDKIDGNEINRLMFDRFQILSQDTQIFVGPDIQSTIGKINTASSTNDFRILDKMKLELTVDLSILPKAYKLPT  815 IRVFGHLPRLSLSINDIQYKTIMNLIANSIPSMIDDE------------------------------E--------NNGD  857
CtVps13 QSTQDRPCTEEDLRRLEELMYDRFLVKLTSTQVLIGPSVEITKQQLVQRDEKRQLHIVDQINLDFVVAMSILPKAPNLTK  803 LKISGHLPVLQVNASDSKYKHLMRIIEVAIPKLYDVEPVLAPSGSHPTIRPRLASDASTRSRRASFRK--------ASTQ  875
hVps13A SELPDVKQGEANLKEIMDRAYDSFDIQLTSVQLLYSRVGDNWREARKLSVSTQ--HILVPMHFNLELSKAMVFMDVRMPK  763 FKIYGKLPLISLRISDKKLQGIMELI-ESIPKPEPVTEVSAPVKSFQIQTSTSLGTSQISQKIIPLLELPSVSEDDSEEE  842
hVps13C KDQGLQKTTNSSLEEIMDKAYDKFDVEIKNVQLLFARAEETWKKCRFQHPSTM--HILQPMDIHVELAKAMVEKDIRMAR  803 FKVSGGLPLMHVRISDQKMKDVLYLM-NSIPLPQKSS-----AQSPERQVSSIPIISGGTKGLLGTSLLLDTVESESDDE  877
SS      h           hhhhhhhh   eeeeeeeeeeeee     hhhhh         eee    eeeeeeeee                eeeeeee  eeeee hhhhhhhhhhhhhh                                                hhh
- - - - - - - - - - - - - - - - - - - - - - - - - - - - - - - - - - - - - - - - - - - - - - - - - - - - - - - - - - - - - - - - - - - - - - - - - - - - - - - - - - - - - - - - - - - - - - -
ScVps13 FFQCIKNDSRNSEKLVDILCQRLNFNFDKRAKEMNLDLRVHSLDVEDYIELTDNKEFKNLISSGVEKVTRSQKDLFTLKY  989 KRVQRIVPHNDTLIELFDQDIVMHMSELQLVLTPRSVLTLMNYA--MLTFTDPNAPEMPADVLRHNKEDRDDAPQKINMK 1067
CtVps13 LYRSDPEGKHPDQLLVELVAENFGVEYHLRPYDMSAMVSLGSVTMDDFVE-NPPAEFKSIVSSGDIEDRKQARDLVRVKF 1010 VRVKKESPEFMSVYDGIETNVDVAISTINLVVTRKTLLTLLDFI--LVTFSNPQPAAPVATRMAVTDQESETNIIVQPPP 1088
hVps13A FYHLVGDCELS---VVEILVLGLGAEIEIRTYDLKANAFLKEFCLKCPEYLDENKKPVYLVTT----LDNTMEDLLTLEY  966 VKAEKNVPDLKSTYNNVLQLIKVNFSSLDIHLHTEALLNTINYLHNIL----PQSEEKSAPVSTTETEDKGDVIKKLALK 1042
hVps13C L---MKKSEKKGRPLHELNVLQLGMEAKVKTYDMTAKAYLKKISMQCFDFTDSKGEPLHIINS----SNVTDEPLLKMLL 1510 TKADSDGPEFKTIHDSTKQRLKVSFASLDLVLHLEALLSFMDFLSSAAPFSEPSSSEKESELKPLVGESRSIAVKAVSSN 1590
SS      eee          eeeeeee   eeeeeee   eeeeeeeeeeeeeeeeee       eee             eeeeee      eee             eeeeeeeeeeeeeeee hhhhhhhhhhh  hhh            hh

ScVps13 IK-------------MEAVNVIFNDDSIKLATLVLSAGEFTMVLLPERYNINLKLGGLELTDETNESFSRDSVFRKIIQM 1134 KGQELVELSYESFDPATNTKDY------DSFLKYSTGSMHVNFIESAVNRMVNFFAKFQKSKVSFDRARLAAYNQAPS-- 1206
CtVps13 IE----SGPIRVKVDLKSIRMILNNDGIRLATLSFNHADVGVYILGRYMRVSAKLGDLSLVDDVNLGVSEDSSLRQLVTI 1164 QGNELADFRYEYFDPDKPEKNPG----YDSSIYLRAGSVKVNFIEEPFRKIVDFLVKFGKMQAIYNAARMAAANQAQQ-- 1238
hVps13A LSTNEDIITLQILAELSCLQIFIQDQKCNISEIKIEGLDSEMIMRPSETEINAKLRNIIVLD-----SDITAIYKKAVYI 1117 TGKEVFSFKMVSYMDATAGSAYTDMNVVDIQVNLIVGCIEVVFVTKFLYSILAFIDNFQAAKQALAEATVQAAGMAATGV 1197
hVps13C IS-QKDVFDLKITAELNAFNVFVCDQKCNIADIKIHGMDASISVKPKQTDVFARLKDIIVMN-----VDLQSIHKKAVSI 1664 LGDEVFRFQLTLYPDATEGEAYADMSKVDGKLSFKVGCIQIVYVHKFFMSLLNFLNNFQTAKEALSTATVQAAERAASSM 1744
SS      ee             eeeeeeeeee   eeeeeee  eeeeeeee  eeeeeeee  eeeee               eee          eeeeeeee                 eeeeeeeeeeeeeeehhhhhhhhhhhhhhhhhhhhhhhhhhhhhhhhhh

ScVps13 ---IDAVNNMKMDIVIKAPIIQFPKLVGTQENNYDTMRFYLGEFFIENKFSVIDESHK-----INHIKLGVREGQLSSNL 1278 NFDGSSQQ-LYLVENIGLLFNIDRDPLPQ--DDTPELKVTSNFESFALDLTENQLTYLLEISNKVSSAFNITDENSGESG 1355
CtVps13 --LQQSQSRIKFDIVVKTPIVVFPRVVMSPKPKRDVITAYLGEIYAQNAFVPLDDSEKA--DMAMKLTTGIRNIRLTSHF 1314 HYSEGRDEVLELIDHVDLGFTIIYAEHKEG-IKRPDLEIEGSMSDFNLRITPYQLSALLAISQSVPTVFAADVEQHTADA 1393
hVps13A KELAQRSSRMALDINIKAPVVVIPQSPVSE----NVFVADFGLITMTNTFHMITESQSSPPPVIDLITIKLSEMRLYRSR 1273 FINDAYQEVLDLLLPLNLEVVVERNLCWEWYQEVPCFNVNAQLKPMEFILSQEDITTIFKTLHG-----NIWYEKDGSAS 1348
hVps13C KDLAQKSFRLLMDINLKAPVIIIPQSSVSP----NAVIADLGLIRVENKFSLVPMEHYSLPPVIDKMNIELTQLKLSRTI 1820 LQASLPQNDIEILKPVNMLLSIQRNLAAAWYVQIPGMEIKGKLKPMQVALSEDDLTVLMKIL----------LENLGEAS 1890
SS         h    eeeeeeee   eeeeee         eeeeee  eeeeeeeeee            eeeeeeeeeeeeeeee      eee    e eeee    eeeeeee           eeeeeee   eeeee hhhhhhhhhhhhh
```

Legend (Similar residues are colored as follows):

AGILMPV - hydrophobic

FHWY - aromatic

QN - polar

ST - polar

DE - acidic

KRH - basic

C - cysteine

Dashed Line indicates where a portion of poorly aligned MSA that was removed, including the following regions:

- ScVps13: 858-909
- CtVps13: 876-931
- hVps13A: 843-893
- hVps13C: 878-1437

Figure 2.11 Multiple sequence alignment for the VPS13 N terminus (Vps13α).

Experiments were performed using CLUSTALOmega. MSA, multiple sequence alignment.

Taken together with the lipid harboring data and transfer assays, the finding that Vps13α and $\text{Vps13}_{\text{crystal}}$ harbor a lipid-binding module or modules supports a lipid-transfer function for Vps13. Based on homology with ATG2, our findings raise the possibility that the N-terminal region of ATG2 may also transfer lipids. Preservation of lipid transfer function does not require high sequence conservation beyond that the residues in the cavity be hydrophobic and those outside hydrophilic (Figure 2.9 C).

2.4 Discussion

Collectively, our findings point to VPS13 proteins as lipid transporters at organelle contact sites (Figure 2.12). They further indicate that as the single Vps13 gene underwent duplications during evolution, specific functions have segregated in different paralogues. The robust localization of VPS13A at ER–mitochondria contacts is of special interest given the partially overlapping function of Vps13 and ERMES in yeast (Lang et al., 2015; Park et al., 2016). As a complex homologous to ERMES does not appear to be present in metazoans, VPS13A may have taken over its role. As loss of VPS13A function results in a neurodegenerative conditions but not in embryonic lethality, VPS13A likely cooperates with other proteins in lipid transport (Galmes et al., 2016; Hirabayashi et al., 2017). These may include VPS13B (whose C-terminal region we have found in preliminary experiments to bind mitochondria) or VPS13D, whose loss results in mitochondrial abnormalities (Anding et al., 2018; Seong et al., 2018). The localization of VPS13C at contacts of the ER with the endolysosomal system was somewhat unexpected since the study first reporting a causative link between VPS13 mutations and Parkinson's disease also reported a partial association of endogenous VPS13C with mitochondrial membranes and a role of VPS13 in mitochondrial function (Lesage et al., 2016). These findings were in line with strong evidence linking mitochondria defects to Parkinson's disease (Hang et al., 2015). However, mitochondrial dysfunction could be an indirect consequence of defects of the endolysosomal system, and several recent studies have linked genetic forms of Parkinson's disease to endolysosomal proteins (reviewed in (Abeliovich and Gitler, 2016)). Moreover, the clear association of VPS13C with late endosomes/lysosomes shown in this study is consistent with the many reported functional connections between VPS13 family members and the endolysosomal system in unicellular organisms (Lang et al., 2015; Munoz-Braceras et al., 2015; Samaranayake et al., 2011), Drosophila melanogaster (Vonk et al., 2017), and mammalian cells (Seifert et al., 2011; Seifert et al., 2015). The association with lipid droplets, which was previously reported in yeast lacking an ER– lipid droplet tethering complex (Grippa et al., 2015), raises the possibility that VPS13 may help transfer lipids not only between membranes but also between these lipid stores and specific cellular membranes. It remains possible that the localizations reported in this study may be subject to regulation depending upon the functional state of the cells as yeast Vps13 localizes at different organelle interfaces depending upon growth conditions (v-CLAMP versus NVJ; (Lang et al., 2015).

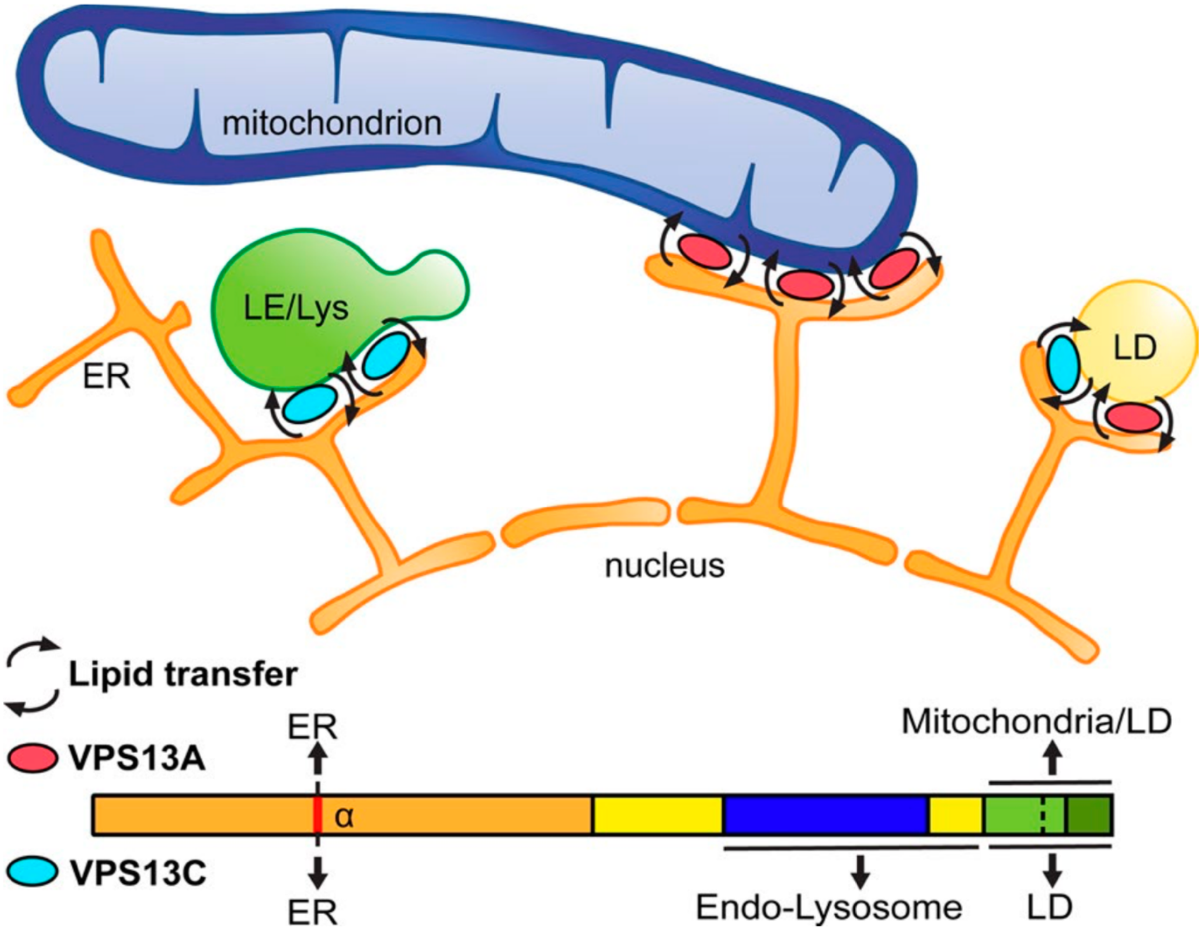

Figure 2.12 Diagram depicting sites of action of VPS13A and VPS13C.

Schematic of VPS13A and VPS13C localization and domains responsible for such localization.

LD, lipid droplet; LE, late endosome; Lys, lysosome.

The atomic structure of $\mathrm{Vps13}_{\mathrm{crystal}}$ and our in vitro lipid transport data indicate that the N-terminal portion of Vps13 forms a lipid transport domain. While these data were obtained with Vps13 from fungi, bioinformatic analysis predicts that the structure of Vps13α is conserved through evolution, suggesting preservation of function (Figure 2.11). The $\mathrm{Vps13}_{\mathrm{crystal}}$ fragment has no structural similarity to any characterized lipid-transfer module beyond the general feature of a hydrophobic cavity that shields lipids from the aqueous environment during their transport through the cytosol. The ability of Vps13α to solubilize multiple lipids at once is atypical (Wong et al., 2017), though it is shared by some lipid transporters in the tubular lipid–binding protein (TULIP) family like ERMES (Jeong et al., 2016) or the Extended-Synaptotagmins (Schauder et al., 2014). The Chorein_N domain has been noted in several other proteins (De et al., 2017; Pfisterer et al., 2014) including ATG2, and its presence likely indicates that they have lipid transport modules similar to Vps13. Indeed, VPS13 and ATG2 may be founding members of a protein family with bulk lipid transport properties.

Bulk lipid transfer by VPS13 family members, in addition to controlling the lipid homeostasis of different membranes, could provide a source of lipids for membrane generation and/or expansion. For example, yeast Vps13, which associates with the spindle pole body component Cdc31 (De et al., 2017), is required for the growth of the prospore membrane that nucleates around this site (Park and Neiman, 2012; Park et al., 2013). Interestingly, lipid droplets were shown to form direct contacts with this membrane (Hsu et al., 2017). ATG2, which has structural similarities to VPS13 both in its N-terminal and C-terminal (ATG_C) region (Pfisterer et al., 2014) and which also binds lipid droplets (Velikkakath et al., 2012), is required for an unrelated but similar process (Knorr et al., 2012): the maturation/closure of the autophagosome membrane (Pfisterer et al., 2014; Velikkakath et al., 2012). The most attractive scenario is that

ATG2's still unknown mechanism of action in this process may involve transfer of lipids from other membranes and, in cells that contain them, from lipid droplets.

A key implication of our study is that defects in lipid dynamics likely play an important role in the clinical manifestations of patients with mutations in VPS13 isoforms, which include major movement disorders such as chorea acanthocytosis (VPS13A) and Parkinson's disease (VPS13C). They also suggest that different properties of each isoform, rather than (or in addition to) their different pattern of cell and tissue expression, may explain the different manifestations of disrupting mutations in VPS13 isoform. An enigmatic feature of the disease resulting from VPS13A mutations (chorea and acanthocytosis, i.e., neurodegeneration and misshaped erythrocytes) is the abnormal shape of red cells (Bird et al., 1978), but it is intriguing that other similar conditions are caused by mutations in proteins involved in lipid metabolism (Aoun et al., 2017; Walsh et al., 2016) or organelle tethering (Holmes et al., 2001). Addressing the precise function of each isoform with loss-of-function studies in cells and intact organisms will be a priority of future investigations. It is expected that these studies may help shed new insight into pathological mechanisms of neurodegenerative conditions.

Chapter 3: The effects of VPS13C loss-of-function on lysosome biology.

A portion of this chapter is available as a preprint:

Hancock-Cerutti, W., Z. Wu, A. K. Tharkeshwar, S. M. Ferguson, G. S. Shadel and P. De Camilli (2021). "ER-lysosome lipid transfer protein VPS13C/PARK23 prevents aberrant mtDNA-dependent STING signaling." bioRxiv.

Author contribution

W. Hancock-Cerutti obtained funding, conceptualized the research, designed and performed the vast majority of experiments, data curation, and formal analysis, and prepared the figures and manuscript.

3.1 Introduction

Genetic studies have revealed many genes whose mutations cause or increase the risk of Parkinson's Disease (PD). Elucidating the functions of these genes, and the mechanisms by which their mutations cause PD, may provide insights into general PD pathophysiology and yield new therapeutic strategies. Several of these genes have been implicated in mitochondrial function (Malpartida et al., 2021), while many others play a role in the endolysosomal system (Abeliovich and Gitler, 2016; Vidyadhara et al., 2019). The extent of physiological and pathological crosstalk between these two organelle systems is a topic of increasing interest (Hughes et al., 2020; Kim et al., 2021; Yambire et al., 2019).

One of the genes whose mutations are responsible for familial early onset PD is VPS13C (Darvish et al., 2018; Lesage et al., 2016; Schormair et al., 2018). The VPS13C locus was also identified in multiple PD GWAS (Nalls et al., 2019). Additionally, loss-of-function mutations in VPS13C genes were detected in dementia with Lewy Bodies, peculiar protein aggregates enriched in alpha-synuclein and characteristic of PD(Smolders et al., 2021). The VPS13 gene family encodes lipid transfer proteins that localize to a variety of distinct contact sites between membranous organelles(Ugur et al., 2020). These proteins are thought to function as bridges that allow phospholipids to traverse the aqueous cytosolic environment between bilayers through a hydrophobic groove that runs along their length(Guillen-Samander et al., 2021; Kumar et al., 2018; Li et al., 2020).

Initial studies of VPS13C focused on a potential role in mitochondrial physiology (Lesage et al., 2016), as at the time studies of the single yeast Vps13 protein had suggested a role of this protein in the transport of lipids to these organelles(Lang et al., 2015). Such studies reported the presence of VPS13C in mitochondria-associated membrane fractions and showed that VPS13C knockdown causes mitochondrial dysfunction (Lesage et al., 2016). This seemed to be consistent with evidence for a major role of defects in mitochondrial clearance in some familial forms of PD (Pickrell and Youle, 2015). However, subsequent studies showed that while VPS13A (Kumar et al., 2018; Yeshaw et al., 2019) and VPS13D(Guillen-Samander et al., 2021) localize to contact sites between the ER and mitochondria, VPS13C localizes instead to contact sites between the ER and late endosomes/lysosomes (Kumar et al., 2018). The localization of VPS13C at endolysosomes, but not mitochondria, was also supported by proximity labeling experiments(Go et al., 2021; Liu et al., 2018)although genetic evidence for an impact of VPS13C on lysosome properties is still missing. A role of VPS13C in the endolysosomal system is not at odds with the established genetic links to PD, given that many PD genes that function in the endolysosomal system(Abeliovich and Gitler, 2016). How defects in this system promote PD, however, remains to be understood.

3.2 Results

3.2.1 Cis and trans determinants of VPS13C binding to late endosomes

We have previously shown that VPS13C localizes to contact sites between the ER and late endosomes/lysosomes positive for the GTPase Rab7(Kumar et al., 2018), a marker of these organelles(Gillingham et al., 2014). Moreover, VPS13C was a hit in a high-throughput screen for interactors of Rab7a(Gillingham et al., 2019). We have not only confirmed that VPS13C localizes to organelles positive for overexpressed Rab7a or constitutively active Rab7a^{Q67L}, but have now demonstrated that co-expression of VPS13C with a dominant negative mutant Rab7a (Rab7a^{T22N}), which cannot localize to late endosomes/lysosomes, causes VPS13C to have a diffuse cytosolic distribution (Figure 3.1 A). In this experiment, dispersal of VPS13C to the cytosol, rather than its accumulation in the ER, the other major VPS13C organelle, may reflect insufficient levels of VAP, its ER binding partner.(Kumar et al., 2018) We observed the same effect when expressing the β-propeller domain of VPS13C (VPS13C$^{\beta\text{-prop}}$) (Figure 3.1 B).

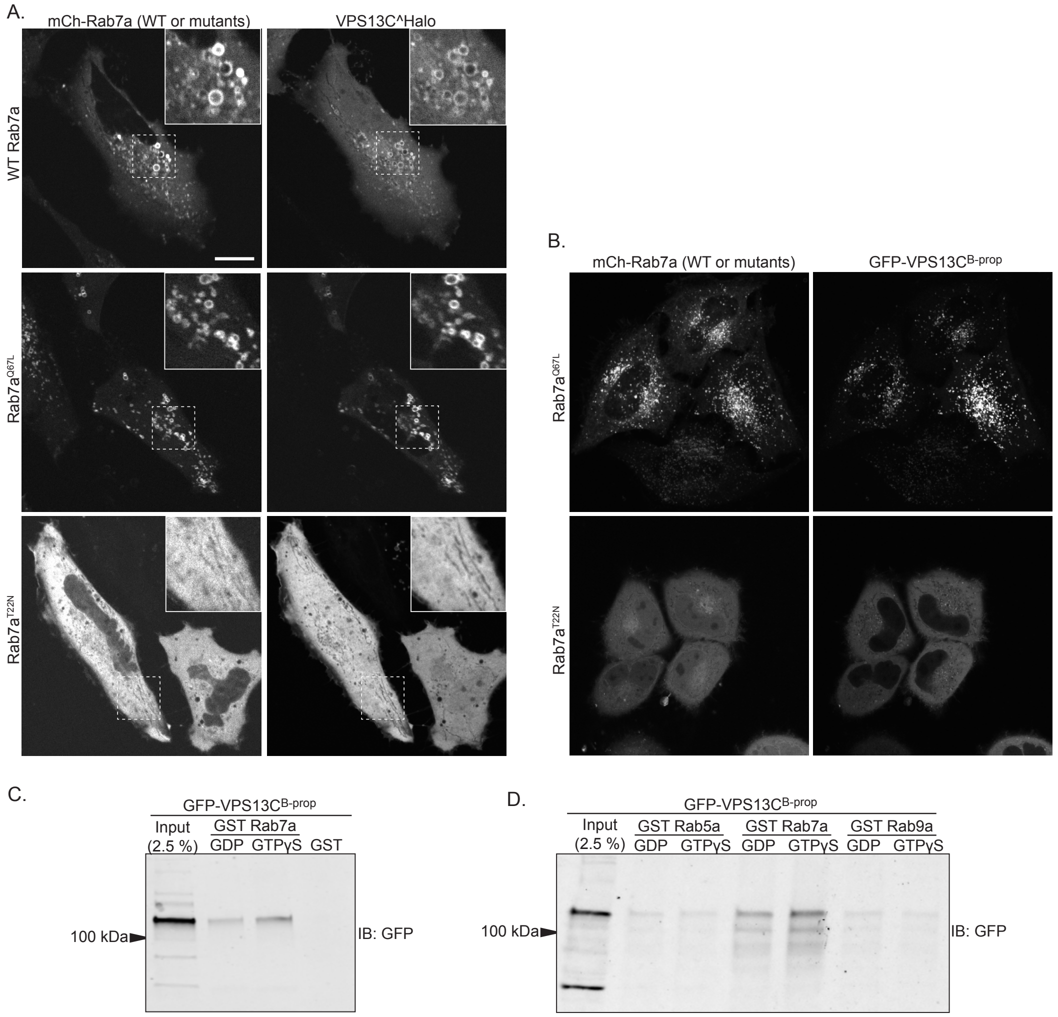

Figure 3.1 Trans binding factors of VPS13C on late endosomes

(A) Live HeLa cells expressing full length VPS13C^Halo with either WT mCherry-Rab7a (top row), constitutively active mCherry-Rab7a^{Q67L} (middle row), or mCherry-Rab7a^{T22N} (bottom row). (B) HeLa cells expressing GFP-VPS13C$^{\beta\text{-prop}}$ with mCherry-Rab7a^{Q67L} (upper row), or mCherry-Rab7a^{T22N} (lower row). (C) Immunoblot of pulldown of lysate from HeLa cells overexpressing GFP-VPS13C$^{\beta\text{-prop}}$ using immobilized GST, GST-Rab7a incubated with GDP, or GST-Rab7a incubated with GTPgS, a nonhydrolyzable analog of GTP. (D) Same as in (C) but including Rab5a and Rab9a.

We next sought to assess biochemically the interaction between VPS13C and Rab7 by performing a pulldown of lysate from cells overexpressing GFP-VPS13C$^{\beta\text{-prop}}$ using GST-bound Rab7 pre-incubated with either GDP or the non-hydrolysable GTP analogue GTPγS (Figure 3.1 C). Surprisingly, we found that both GDP and GTPγS-bound Rab7 pulled down, suggesting that GTP binding is not strictly necessary for VPS13C to interact with Rab7, though the GTPγS-bound Rab7 did pull down >2 fold as much GFP-VPS13C$^{\beta\text{-prop}}$ by densitometry. To confirm the specificity of this interaction, we repeated the experiment using purified GST-tagged Rab5 and Rab9 as controls, and found no interaction of either of them with GFP-VPS13C$^{\beta\text{-prop}}$, despite previous data that VPS13C may interact with Rab9 (Figure 3.1 D).(Huttlin et al., 2017) Together, these findings demonstrate a key role of Rab7 in the recruitment of VPS13C to late endosomes/lysosomes.

3.2.2 Mutation of multiple conserved asparagine residues in the β-propeller domain prevent binding to late-endosomes, but mutations associated with Lewy-Body dementia have no effect

It was previously reported that in yeast Vps13, a region coined the Vps13 adaptor binding (VAB) domain, which roughly corresponds to the predicted β-propeller domain, is responsible for binding Vps13's various adapter proteins (Ypt35 on endosomes/vacuole, Mcp1 on mitochondria, and Spo71 on the sporulation membrane).(Bean et al., 2018; Dziurdzik et al., 2020) Moreover, there are six conserved repeating elements in this domain, containing asparagine residues that are highly conserved across species (N1-N6) (Figure 3.2 A). Of these six asparagine residues, numbers 1 and 6 appear to be the most critical for adaptor binding, as mutation of these residues to alanine in yeast Vps13 reduced binding to all adaptors tested.(Dziurdzik et al., 2020) Since VPS13C binds to late-endosomes via its β-propeller domain (Figure 3.2 B), we investigated whether these residues remained critical for VPS13C$^{\beta\text{-prop}}$ binding.

We mutated each of these asparagine residues to serine in the VPS13C$^{\beta\text{-prop}}$ construct evaluated co-localization with Rab7a. We found that mutation of any single of these six asparagine residues failed to completely disrupt VPS13C binding to late endosomes (Figure 3.2 C, - N2, N3, and N4 mutations not shown). Because N1 and N6 had been shown to be the most critical for adaptor binding, and because a fragment containing only repeats 5 and 6 was sufficient for binding to all three yeast adaptor proteins,(Dziurdzik et al., 2020) we attempted to make double and triple mutants of N1, N5, and N6. Despite multiple cloning attempts using different strategies, we failed to generate the VPS13C$^{\beta\text{-prop-N1,6S}}$ mutant, however we were able to generate VPS13C$^{\beta\text{-prop-N5,6S}}$ and the VPS13C$^{\beta\text{-prop-N1,5,6S}}$ constructs. We found that VPS13C$^{\beta\text{-prop-N5,6S}}$ was still able to bind to late endosomes, though it appeared to bind less strongly and with greater cytosolic background. By contrast, VPS13C$^{\beta\text{-prop-N1, 5,6S}}$ completely failed to bind to late-endosomes and was instead diffuse throughout the cytosol, suggesting that these asparagine residues still play a role in binding to adaptors for VPS13C (Figure 3.2 C).

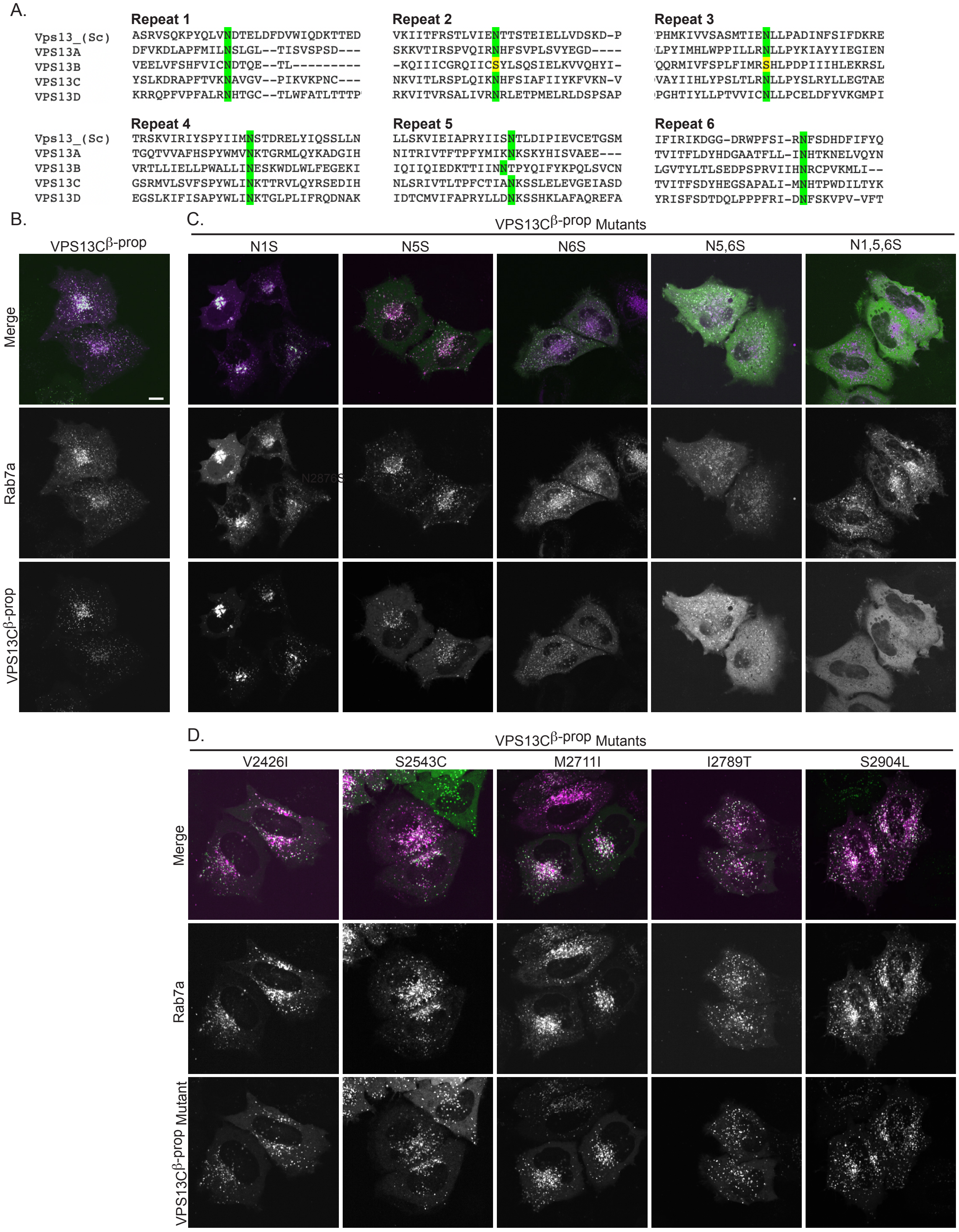
A.
Repeat 1
Vps13_(Sc) ASRVSQKPYQLVNDTELDFDVWIQDKTTED
VPS13A DFVKDLAPFMILNSLGL--TISVSPSD---
VPS13B VEELVFSHFVICNDTQE--TL---------
VPS13C YSLKDRAPFTVKNAVGV--PIKVKPNC---
VPS13D KRRQPFVPFALRNHTGC--TLWFATLTTTP
Repeat 2
VKIITFRSTLVIENTTSTEIELLVDSKD-P
SKKVTIRSPVQIRNHFSVPLSVYEGD----
-KQIIICGRQIICSYLSQSIELKVVQHYI-
NKVITLRSPLQIKNHFSIAFIIYKFVKN-V
RKVITVRSALIVRNRLETPMELRLDSPSAP
Repeat 3
PHMKIVVSASMTIENLLPADINFSIFDKRE
LPYIMHLWPPILLRNLLPYKIAYYIEGIEN
QQRMIVFSPLFIMRSHLPDPIIIHLEKRSL
VAYIIHLYPSLTLRNLLPYSLRYLLEGTAE
PGHTIYLLPTVVICNLLPCELDFYVKGMPI
Repeat 4
Vps13_(Sc) TRSKVIRIYSPYIIMNSTDRELYIQSSLLN
VPS13A TGQTVVAFHSPYWMVNKTGRMLQYKADGIH
VPS13B VRTLLIELLPWALLINESKWDLWLFEGEKI
VPS13C GSRMVLSVFSPYWLINKTTRVLQYRSEDIH
VPS13D EGSLKIFISAPYWLINKTGLPLIFRQDNAK
Repeat 5
LLSKVIEIAPRYIISNTLDIPIEVCETGSM
NITRIVTFTPFYMIKNKSKYHISVAEE---
IQIIQIEDKTTIINNTPYQIFYKPQLSVCN
NLSRIVTLTPFCTIANKSSLELEVGEIASD
IDTCMVIFAPRYLLDNKSSHKLAFAQREFA
Repeat 6
IFIRIKDGG-DRWPFSI-RNFSDHDFIFYQ
TVITFLDYHDGAATFLL-INHTKNELVQYN
LGVTYLTLSEDPSPRVIIHNRCPVKMLI--
TVITFSDYHEGSAPALI-MNHTPWDILTYK
YRISFSDTDQLPPPFRI-DNFSKVPV-VFT
B.
VPS13Cβ-prop
Merge
Rab7a
VPS13Cβ-prop
C.
VPS13Cβ-prop Mutants
N1S
N5S
N6S
N5,6S
N1,5,6S
N2873S
D.
VPS13Cβ-prop Mutants
V2426I
S2543C
M2711I
I2789T
S2904L
Merge
Rab7a
VPS13Cβ-prop Mutant

Figure 3.2 Cis binding factors of VPS13C

(A) Amino acid sequence alignments of repeat regions within the VPS13C β-propeller domain from S. Cerevisiae Vps13 and H. Sapiens VPS13A, VPS13B, VPS13C, and VPS13D. Conserved asparagine residues are highlighted in green. (B) WT VPS13C$^{\beta\text{-prop}}$ co-expressed with Rab7a in HeLa cells. (C) VPS13C$^{\beta\text{-prop}}$ constructs with mutations to conserved arginine residues co-expressed with Rab7a in HeLa cells. (D) VPS13C$^{\beta\text{-prop}}$ constructs with Lewy-Body Dementia-associated mutations co-expressed with Rab7a in HeLa cells.

Additional missense mutations in the VPS13C$^{\beta\text{-prop}}$ region were identified in Belgian patients with PD or dementia with Lewy Bodies (DLB),(Smolders et al., 2021) though whether these mutations are pathogenic is not well established. To investigate whether any of these mutations might abrogate binding of VPS13C to late endosomes, we generated VPS13C$^{\beta\text{-prop}}$ constructs with each of the five reported mutations and evaluated co-localization with Rab7a. All of these constructs still colocalized with Rab7a, suggesting that if they are indeed deleterious to protein function, it is not related to the ability to bind to Rab7a (Figure 3.2 D). As these experiments corroborate the idea that contacts between the ER and endolysosomes are a main site of action of VPS13C, we investigated whether the absence of VPS13C has an impact on lysosomal parameters.

3.2.3 Loss of VPS13C results in perturbation of lysosomal homeostasis

We generated two independent VPS13C^{KO} HeLa cell lines using CRISPR-Cas9 genome editing and confirmed indel mutations leading to premature stop codons by genomic sequencing (Figure 3.3 A). Loss of protein expression was validated by immunoblotting (Figure 3.3 B). Both VPS13C^{KO} clones had significantly elevated levels of the lysosomal membrane protein LAMP1 and of the luminal protease Cathepsin D, as assessed by western blotting (Figure 3.3 C and D). Moreover, imaging assays revealed an increased lysotracker signal (Figure 3.3 E and F), further supporting an increase in lysosome abundance and showing that these lysosomes have an acidic lumen.

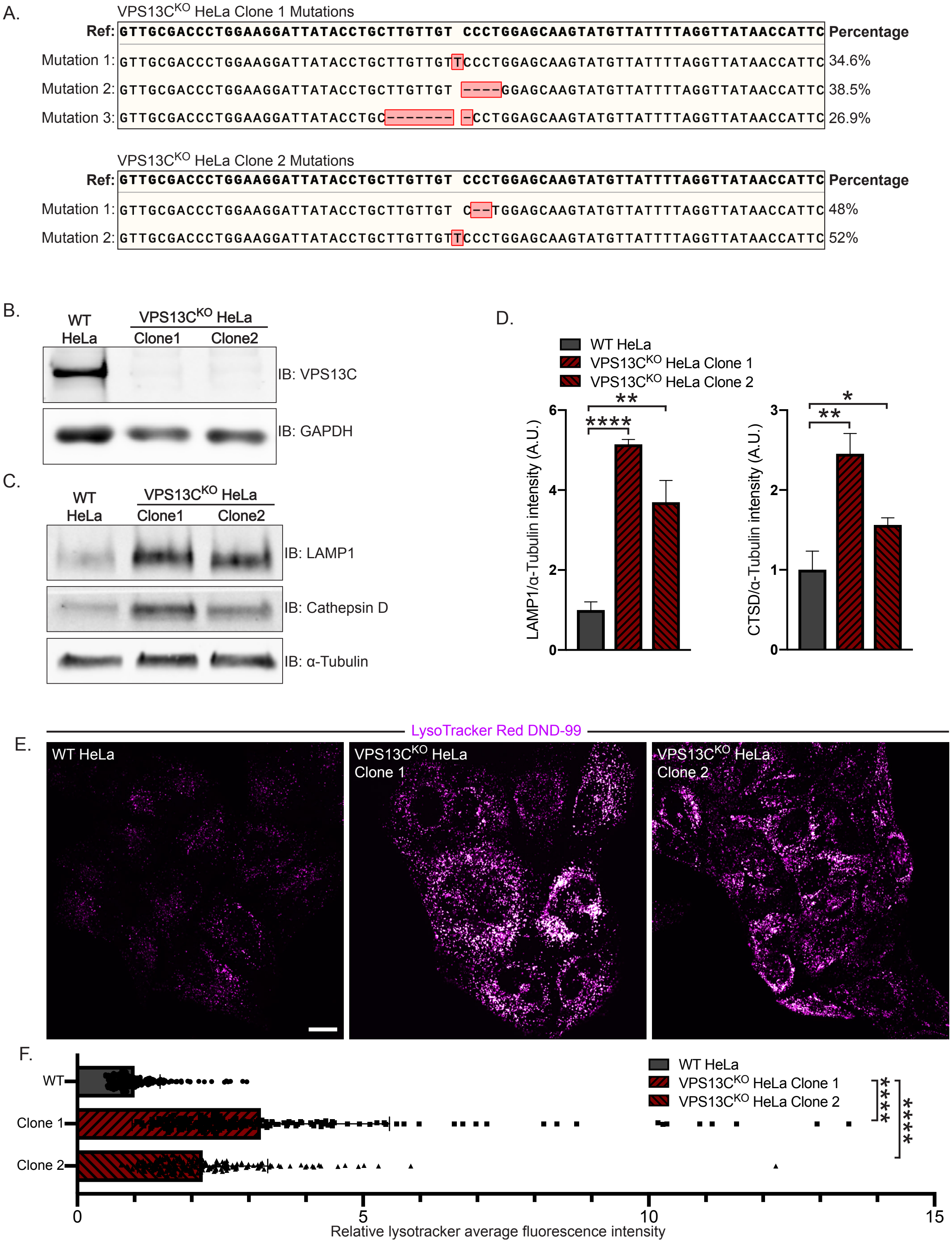
A.
VPS13C^{KO} HeLa Clone 1 Mutations
Ref: GTTGCGACCCTGGAAGGATTATACCTGCTTGTTGT CCCTGGAGCAAGTATGTTATTTTAGGTTATAACCATTC Percentage
Mutation 1: GTTGCGACCCTGGAAGGATTATACCTGCTTGTTGTTCCCTGGAGCAAGTATGTTATTTTAGGTTATAACCATTC 34.6%
Mutation 2: GTTGCGACCCTGGAAGGATTATACCTGCTTGTTGT ----GGAGCAAGTATGTTATTTTAGGTTATAACCATTC 38.5%
Mutation 3: GTTGCGACCCTGGAAGGATTATACCTGC------- -CCTGGAGCAAGTATGTTATTTTAGGTTATAACCATTC 26.9%
VPS13C^{KO} HeLa Clone 2 Mutations
Ref: GTTGCGACCCTGGAAGGATTATACCTGCTTGTTGT CCCTGGAGCAAGTATGTTATTTTAGGTTATAACCATTC Percentage
Mutation 1: GTTGCGACCCTGGAAGGATTATACCTGCTTGTTGT C--TGGAGCAAGTATGTTATTTTAGGTTATAACCATTC 48%
Mutation 2: GTTGCGACCCTGGAAGGATTATACCTGCTTGTTGTTCCCTGGAGCAAGTATGTTATTTTAGGTTATAACCATTC 52%
B.
WT HeLa
VPS13C^{KO} HeLa
Clone1
Clone2
IB: VPS13C
IB: GAPDH
C.
WT HeLa
VPS13C^{KO} HeLa
Clone1
Clone2
IB: LAMP1
IB: Cathepsin D
IB: α-Tubulin
D.
WT HeLa
VPS13C^{KO} HeLa Clone 1
VPS13C^{KO} HeLa Clone 2
LAMP1/α-Tubulin intensity (A.U.)
0
2
4
6
****
**
CTSD/α-Tubulin intensity (A.U.)
0
1
2
3
**
*
E.
LysoTracker Red DND-99
WT HeLa
VPS13C^{KO} HeLa Clone 1
VPS13C^{KO} HeLa Clone 2
F.
WT
Clone 1
Clone 2
WT HeLa
VPS13C^{KO} HeLa Clone 1
VPS13C^{KO} HeLa Clone 2
****
****
0
5
10
15
Relative lysotracker average fluorescence intensity

Figure 3.3 Deletion of VPS13C causes accumulation of lysosomes.

(A) Mutations in the VPS13C locus in VPS13C^{KO} clones 1 and 2. Percent abundance out of 48 bacterial colonies sequenced. The HeLa cells genome is known to be aneuploid. (B) Immunoblot of VPS13C in WT HeLa cells and two individual clonal cell lines after CRISPR-Cas9 mediated knockout of VPS13C. (C) Immunoblot of Lamp1 and Cathepsin D in WT and VPS13C^{KO} cells, quantified in (D). α-tubulin was used as a loading control. n=3 biological replicates. (E) Live WT and VPS13C^{KO} HeLa cells stained with LysoTracker Red DND-99 (50 nM), quantified in (F), n=3 biological replicates. Scale bars 20 μm. * $P < 0.05$, ** $P < 0.01$, **** $P < 0.0001$.

3.2.4 Loss of VPS13C causes alterations in lipid classes in whole cell and lysosomal lipidome

Whole cell lipidomics

Given the putative role of VPS13C as a lipid transfer protein, we next examined the impact of the absence of VPS13C on the cellular and lysosomal lipidome. Whole cell lipidomics revealed a number of changes. Phosphatidyl choline (PC) was decreased in both VPS13C^{KO} clones relative to WT, while ether linked PC (PC-O) was increased (Figure 3.4 A). Phosphatidylethanolamine (PE) was decreased substantially, while phosphatidylserine (PS) was elevated, suggesting a possible defect in either the Kennedy or PSD pathways of PE synthesis (Patel and Witt, 2017). Both ceramide (Cer) and hexosylceramide (HexCer) were increased, and lyso-PC (LPC) and lyso-PE (LPE) were decreased.

Lysosome lipidomics

Since VPS13C is localized at ER-late endosome/lysosome contact sites, we paid particular attention to the lysosomal lipidome. In order to isolate lysosomes, we pulsed (4 hrs) cells with dextran-coated superparamagnetic iron-oxide nanoparticles (SPIONs), which were taken up through bulk-endocytosis and trafficked to the endolysosomal compartment (Tharkeshwar et al., 2020; Tharkeshwar et al., 2017). Imaging of a fluorescently-tagged version of these nanoparticles at 15 hrs after the pulse confirmed their trafficking to vesicular structures which were positive for both LAMP1 and for a transfected construct comprising the beta-propeller region of VPS13C (VPS13C$^{\beta\text{-prop}}$), i.e. the Rab7-binding region of VPS13C (Figure 3.4 B). This observation confirmed the accumulation of the nanoparticles in a VPS13C-relevant compartment. Cell lysis and purification of nanoparticles-enriched lysosomes using a magnetic column yielded > 67-fold enrichment of the integral lysosomal membrane protein LAMP1 relative to the control protein GAPDH, as well as an enrichment of the late-endosomal marker Rab7, a peripheral membrane protein (Figure 3.4 C and D).

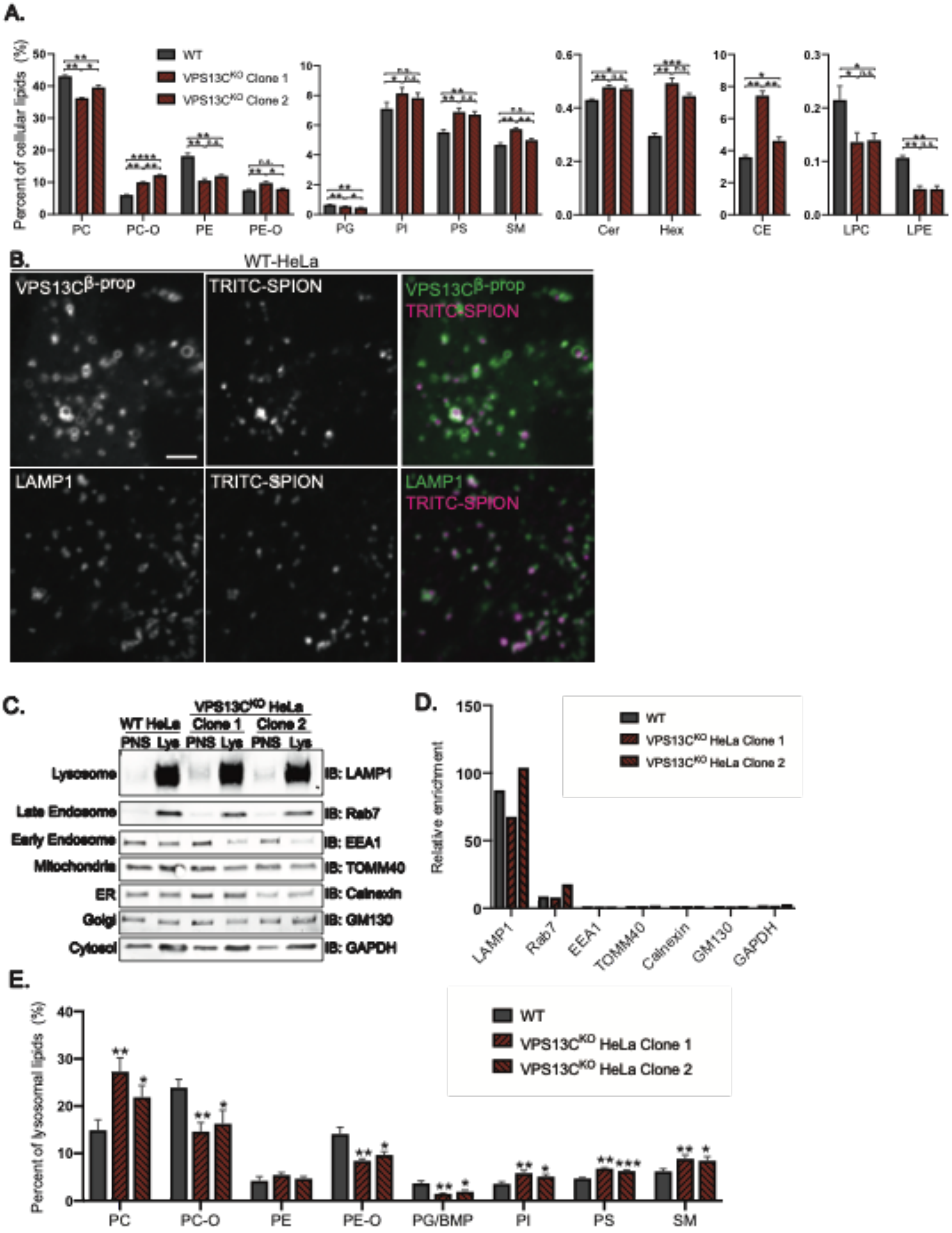
A.
Percent of cellular lipids (%)
WT
VPS13C^KO Clone 1
VPS13C^KO Clone 2
PC
PC-O
PE
PE-O
PG
PI
PS
SM
Cer
Hex
CE
LPC
LPE
B.
WT-HeLa
VPS13C^β-prop
TRITC-SPION
LAMP1
C.
VPS13C^KO HeLa
WT HeLa
Clone 1
Clone 2
PNS
Lys
Lysosome
Late Endosome
Early Endosome
Mitochondria
ER
Golgi
Cytosol
IB: LAMP1
IB: Rab7
IB: EEA1
IB: TOMM40
IB: Calnexin
IB: GM130
IB: GAPDH
D.
Relative enrichment
WT
VPS13C^KO HeLa Clone 1
VPS13C^KO HeLa Clone 2
LAMP1
Rab7
EEA1
TOMM40
Calnexin
GM130
GAPDH
E.
Percent of lysosomal lipids (%)
WT
VPS13C^KO HeLa Clone 1
VPS13C^KO HeLa Clone 2
PC
PC-O
PE
PE-O
PG/BMP
PI
PS
SM

Figure 3.4 Loss of VPS13C results in altered cellular and lysosomal lipid composition

(A) Percentages of lipid classes in WT and VPS13C^{KO} HeLa cell lysates normalized to total measured lipid content. N = 3 biological replicates. (B) Colocalization of TRITC-labelled SPIONs with overexpressed GFP-VPS13C$^{\beta prop}$ (top row) or LAMP1-GFP (bottom row) after 4 hour pulse and 15 hour chase. Scale bar 5 μm. (C) Immunoblot showing abundance of organelle markers in post-nuclear supernatant (PNS) and lysosomal fractions (Lys) from WT and VPS13C^{KO} HeLa cells. Equal amounts of total protein was loaded in each lane. Note the striking enrichment of LAMP1 in lysosomal fractions. (D) Quantification of band intensities from (C) normalized to GAPDH to show relative enrichment. (E) Percentages of phospho- and sphingolipid classes in WT and VPS13C^{KO} lysosomal fractions normalized to total measured lysosomal lipid content. N = 4 biological replicates. * $q < 0.05$, ** $q < 0.01$, *** $q < 0.001$, **** $q < 0.0001$.

Shotgun mass spectrometry-based lipidomic analysis of the major lipid classes in the lysosomal fractions revealed substantial differences between VPS13C^{KO} and controls on a percent molar basis (specific lipid class versus total lipids) that were consistent in both VPS13C^{KO} clones (Figure 3.4 E). There were increases in phosphatidylcholine (PC), phosphatidylserine (PS), phosphatidylinositol (PI), and sphingomyelin (SM), as well as a decrease in phosphatidylglycerol (PG). PG measurement may include bis(monoacylglycerol)phosphate (BMP), as PG and BMP are structural isomers that were not distinguished by this analysis (Figure 3.4 E). In addition, ether-lipid forms of both phosphatidylcholine (PC-O) and phosphatidylethanolamine (PE-O) were significantly reduced in the lysosomes of both VPS13C^{KO} clones (Figure 3.4 E), though there was no decrease in these lipids, and even a slight increase, in the total cell lipidome (Figure 3.4 A). Collectively, these findings reveal a perturbation of lysosomal lipid homeostasis in VPS13C^{KO} cells.

3.2.5 Enhanced levels of di-22:6-BMP in VPS13C^{KO} HeLa cells

We next analyzed individual lipid species in control and VPS13C^{KO} lysosomes. Among the 1161 species measured, we found that 123 of them were significantly altered in both VPS13C^{KO} clones relative to controls (Figure 3.5 A). In agreement with the class-level decreases, most of the downregulated hits were PC-O and PE-O species. The upregulated hits comprised a variety of classes including PC, PI, PE, and SM, many containing polyunsaturated fatty acid (PUFA) tails including arachidonic acid (20:4), eicosapentaenoic acid (20:5), docosapentaenoic acid (22:5), and docosahexaenoic acid (DHA, 22:6).

The most highly increased lipid species in one of the VPS13C^{KO} clones and the third highest in the other one, was PG(22.6_22.6) (Figure 3.5 A), black arrowhead), which, as stated above, could not be distinguished from its structural isomer di-22:6-BMP. As BMPs (also referred to as LBPA) are specific to the endolysosomal system (Gruenberg, 2020), we suspected that the majority of the species reported as PG(22.6_22.6) was actually di-22:6-BMP. This was intriguing, as di-22:6-BMP has been established as a biomarker for a number of neurodegenerative diseases, including Niemann Pick type C (Liu et al., 2014) and, more recently, LRRK2 G2019S mutation status (Alcalay et al., 2020). The increase of di-22:6-BMP in whole cell lysate was confirmed by a quantitative mass spectrometry assay specifically designed to assess this lipid (Figure 3.5 C). Moreover, di-18:1-BMP, which appears to be the most abundant species in HeLa cells and is a major species in most human tissues(Showalter et al., 2020) was decreased (Figure 3.5 C). This is consistent with our findings that total PG/BMP species are decreased by about half in VPS13C^{KO} lysosomes, revealing an overall decrease in total BMP but a specific increase in di-22:6-BMP (Figure 3.4 E and 3.5 B).

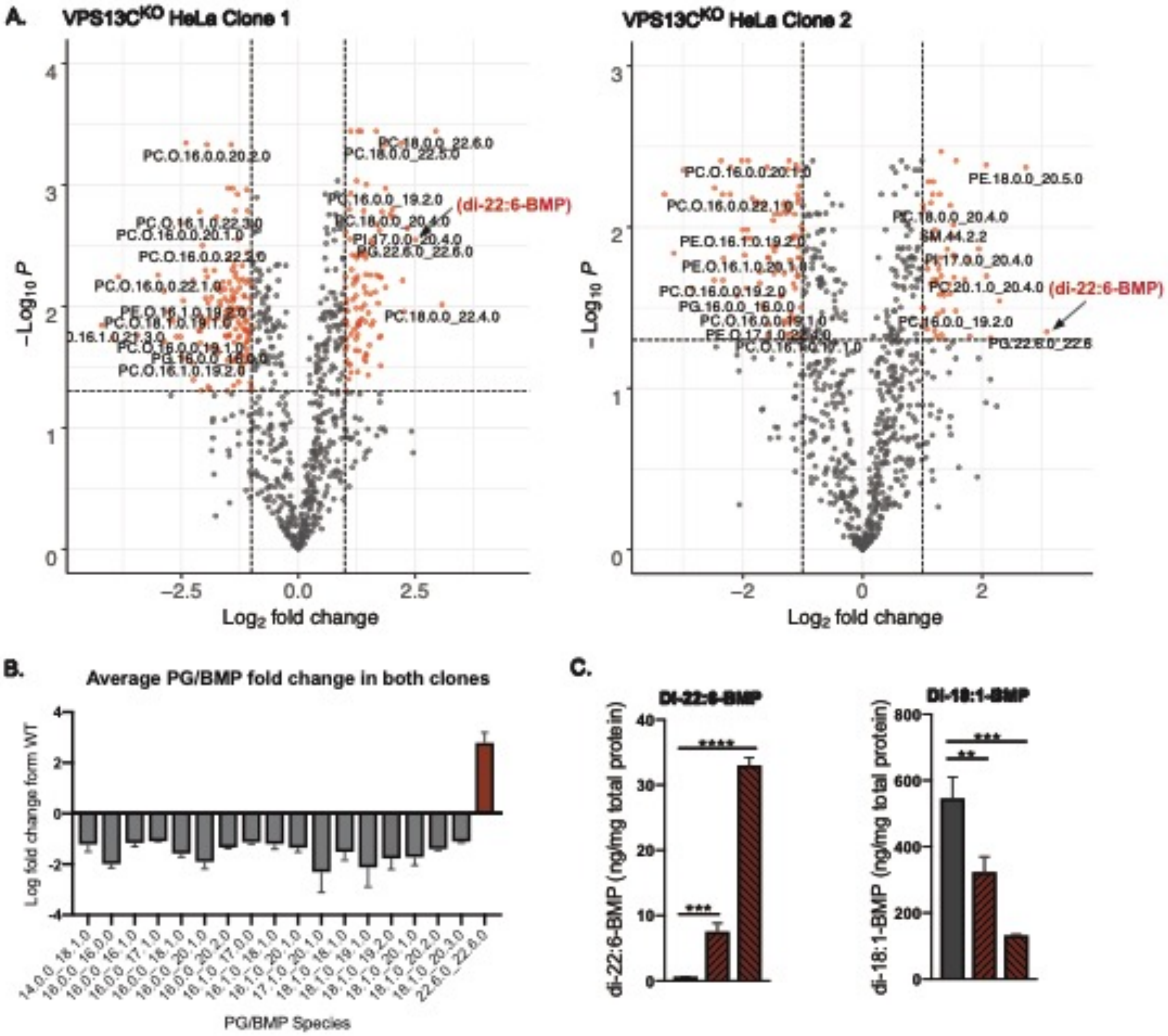

Figure 3.5 Analysis of lipid species and BMP levels

(A) Volcano plots of individual lipid species in VPS13C^{KO} purified lysosomes. Species that surpass the q-value and fold-change thresholds are shown as red dots. Lipid species labels are centered under corresponding dot. Arrows show PG.22.6.0_22.6.0/di-22:6-BMP. (B) Barplot showing the average fold change of PG/BMP species in both clones. Only species with q-values < 0.05 are shown. (C) Concentrations of di-22:6- and di-18:1-BMP normalized to total protein in WT and VPS13C^{KO} HeLa total cell lysate. N = 3 biological replicates. * $P < 0.05$, ** $P < 0.01$, *** $P < 0.001$, **** $P < 0.0001$ compared to WT control.

3.2.6 Enhanced levels of di-22:6-BMP in VPS13C^{KO} iPSC induced neurons

To determine whether VPS13C loss-of-function also disrupted lysosome homeostasis in a neuronal cell type, we used CRISPR-Cas9 to knock out VPS13C in an induced pluripotent stem cell (iPSC) line in which an expression cassette containing neurogenin-2 (NGN2) under a doxycycline inducible promoter had been stably integrated into the safe-harbor locus (Wang et al., 2017). After selecting single clones, we confirmed knockout of VPS13C by immunoblot and sanger sequencing (Figure 3.6 A). After 14 days of differentiation into i^{3}Neurons according to published protocols (Fernandopulle et al., 2018), we did not detect an increase in LAMP1 protein levels in the VPS13C^{KO} i^{3}Neurons compared to WT(Figure 3.6 A). We did however find, as in VPS13C^{KO} HeLa cells, that di-22:6-BMP was elevated by at least 7-fold in the two VPS13C^{KO} clones, while di-18:1-BMP was decreased by about half (Figure 3.6 B).

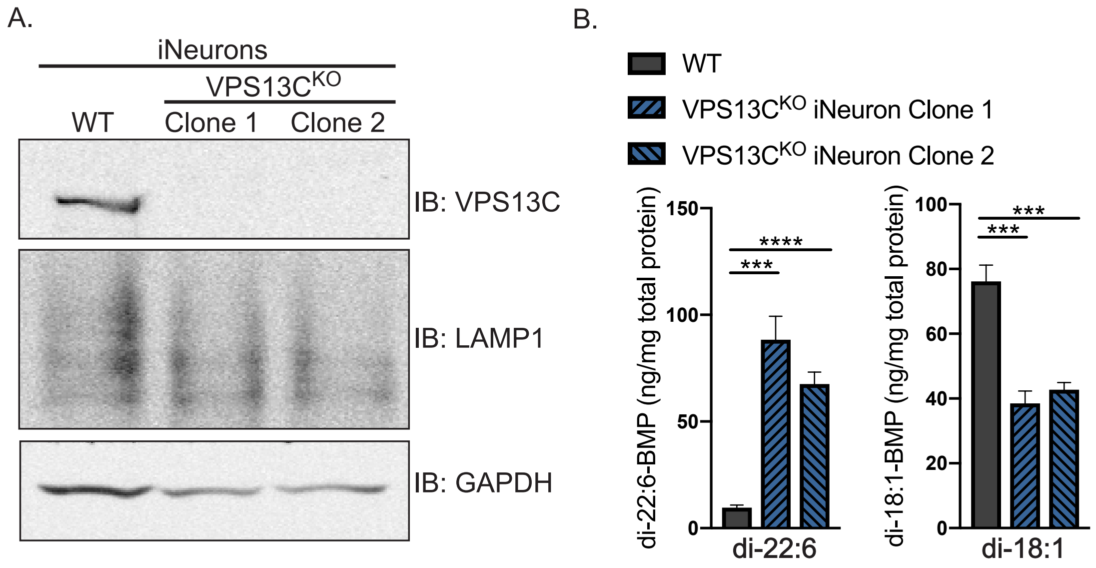

Figure 3.6 Analysis of BMP levels in VPS13C^{KO} iNeurons

(A) Immunoblot of VPS13C and LAMP1 in WT and VPS13C^{KO} iNeurons. GAPDH was used as a loading control. (D) Concentrations of di-22:6- and di-18:1-BMP normalized to total protein in WT and VPS13C^{KO} iNeuron total cell lysate. N = 3 biological replicates. *** $P < 0.001$, **** $P < 0.0001$ compared to WT control.

3.3 Discussion

We have previously shown a colocalization of VPS13C at the interface between the ER and organelles positive for Rab7, a marker of late endosomes and lysosomes. Moreover, VPS13C was identified in a screen for Rab7 effectors(Gillingham et al., 2019). Our present finding that dominant negative Rab7 completely blocks VPS13C recruitment to lysosomes proves its major role in controlling VPS13C localization. Importantly, we show that absence of VPS13C results in alterations in lysosome homeostasis, as demonstrated by an increase in the levels of lysosome markers LAMP1 and CTSD. We did not detect a defect in lysosomal acidification, and the increased lysotracker signal that we observed suggests that these lysosomes remain acidified, though a more sensitive assay of lysosomal pH may reveal a difference.

As predicted given the role of VPS13C as a lipid transfer protein at ER-late endosome/lysosome contact sites, we detected major alterations of the lipid composition of purified lysosomal fractions in the VPS13C^{KO} cells. Increases were observed in PC, PI, PS, and SM, with decreases in ether-linked phospholipids (PC-O and PE-O) and in BMP, a class of lipids characteristic of multivesicular bodies and lysosomes (Gruenberg, 2020). Whether these changes are directly or indirectly related to the property of VPS13C to transport lipids remains to be explored, as do the functional implications of these changes. We hypothesize that one function of VPS13C is to facilitate the transport of ether lipids from the ER, the site of the final steps of their synthesis, to late endosomes/lysosomes. The effects of the observed decreases in lysosomal ether lipid content remain to be characterized, but ether lipids have been proposed to play a role in membrane fusion and fission(Dean and Lodhi, 2018; Jimenez-Rojo and Riezman, 2019).

Of note was the robust and highly specific accumulation of di-22:6-BMP in both lysosomes and total cell lysates from HeLa cells, as well as cell lysates from iNeurons, in spite of the overall reduction of BMP. A specific increase in urinary di-22:6-BMP was reported to be a marker of LRRK2 G2019S mutation status (Alcalay et al., 2020). Like the absence of VPS13C, the LRRK2 G2019S mutation increases PD risk (West et al., 2005). Importantly, di-22:6-BMP was reported to be a marker of LRRK2 G2019S mutation status, and was elevated whether or not the subjects had clinical PD i.e. di-22:6-BMP levels in urine are not a biomarker for PD, but rather LRRK2 G2019S mutation status. This may suggest that increases in di-22:6-BMP may precede clinical PD symptoms, leaving open the possibility that this lipid plays an active role in the disease process. BMP plays an important role in a number of endo-lysosomal processes, including ILV formation (Matsuo et al., 2004). It also supports the function of numerous proteins of the late endsosome/lysosome including ALIX, Hsp70, NPC-2, and acid sphingomyelinase (ASM) (Showalter et al., 2020). Total BMP is reduced in certain subtypes of Neuronal Ceroid Lipofuscinosis (NCL)(Hobert and Dawson, 2007), and is also altered by knockout of Progranulin, a lysosomal protein whose loss-of-function mutation cause both NCL (homozygous) and Frontotemporal Dementia (FTD) (heterozygous) (Logan et al., 2020).

Whether and how BMP is involved in the pathogenesis of PD is an area of active study. While the significance of the specific increase in di-22:6-BMP and decrease of total BMP remains unclear, this finding is consistent with alteration of lysosomal function across multiple neurodegenerative conditions.

Loss of VPS13C function also has an impact on the overall cell lipidome. The significant reduction of PE is of interest, as PE is a major structural lipid of cell membranes. PE deficiency has also been proposed to play a role in PD pathogenesis(Calzada et al., 2016; Patel and Witt, 2017). Deficiency of PE has been shown to impair oxidative phosphorylation and alter mitochondrial morphology (Tasseva et al., 2013) and perturb a-synuclein homeostasis (Wang et al., 2014). PE was found to be reduced in the substantia nigra(Riekkinen et al., 1975) and cerebrospinal fluid (CSF)(Manyam et al., 1988) of PD patients compared to controls. The increases in Cer and HexCer are also of interest, given that HexCer is the substrate of GBA1 and accumulates in the context of GBA1 deficiency (Ishibashi et al., 2013).

Chapter 4: VPS13C loss-of-function in HeLa cells causes activation of the STING pathway by cytosolic mtDNA.

A portion of this chapter is available as a preprint:

Hancock-Cerutti, W., Z. Wu, A. K. Tharkeshwar, S. M. Ferguson, G. S. Shadel and P. De Camilli (2021). "ER-lysosome lipid transfer protein VPS13C/PARK23 prevents aberrant mtDNA-dependent STING signaling." bioRxiv.

Author contribution

W. Hancock-Cerutti obtained funding, conceptualized the research, designed and performed the vast majority of experiments, data curation, and formal analysis, and prepared the figures and manuscript.

4.1 Introduction

Recent studies have implicated activation of the innate immune response in PD pathogenesis. Specifically, it has been reported that defective mitochondrial clearance in mice with Parkin and PINK1 loss-of-function mutations subjected to additional mitochondrial stressors may result in mitochondrial DNA (mtDNA) leakage into the cytosol, leading to activation of the cGAS-STING pathway (Sliter et al., 2018). Such activation, in turn, induces the transcription of interferon-stimulated genes (ISGs) and an NF-κB-mediated inflammatory response (Motwani et al., 2019). While cGAS and STING are primarily expressed in non-neuronal cells in brain, including microglia and astrocytes (Saunders et al., 2018), there is growing evidence that some other genes involved in neurodegenerative diseases, including PD, are also expressed primarily in non-neuronal cells including immune cells(Cook et al., 2017). Interestingly, activation of the cGAS-STING pathway due to elevated cytosolic mtDNA was observed in bone marrow-derived macrophages (BMDMs) and mouse embryonic fibroblasts (MEFs) lacking LRRK2(Weindel et al., 2020), a PD gene associated with lysosomes (Bonet-Ponce et al., 2020). Moreover, absence of C9orf72, an ALS gene and a component of a signaling complex associated with lysosomes (Amick et al., 2016), results in hyperresponsiveness to activators of STING likely due to impaired degradation of STING in lysosomes (McCauley et al., 2020). As multiple groups have shown that activation of STING, an ER resident protein, triggers its transport from the ER to lysosomes, where it is degraded, defective lysosomal function may delay clearance of activated STING (Gonugunta et al., 2017; Gui et al.). These previous studies raise the possibility that an interplay of mitochondrial defects (such as mtDNA leakage) and lysosomal defects (such as impaired STING degradation) may synergize in the activation of the innate immune response leading to neuroinflammation in some neurodegenerative diseases.

Intriguingly, the single yeast VPS13 gene is required both for mitochondrial integrity(Lang et al., 2015; Park et al., 2016) and for proper function of the endolysosomal system(Brickner and Fuller, 1997). Moreover, this yeast protein was identified in a genetic screen for mutations that cause the escape of mtDNA to the nucleus, hence its alias YME3 (Yeast Mitochondrial Escape)(Thorsness and Fox, 1993). Follow-up studies of another YME gene, the ATP-dependent mitochondrial metalloprotease YME1, revealed that escape of mtDNA required degradation of mitochondrial compartments in the vacuole, the yeast equivalent of the lysosome(Campbell and Thorsness, 1998). Moreover, recent studies of mammalian YME1L demonstrate that loss-of-function results in mtDNA leakage and activation of the cGAS-STING pathway (Sprenger et al., 2021). All these findings prompted us to explore a potential activation of the cGAS-STING pathway by mtDNA in VPS13C depleted cells and its potential relationship to lysosome dysfunction.

4.2 Results

4.2.1 Activation of the cGAS/STING pathway

Having previously defined an impact of the lack of VPS13C on lysosomal homeostasis, we next addressed the hypothesis that the absence of VPS13C could result in an activation of the cGAS-STING pathway (Figure 4.1 A). First, as a readout of potential cGAS-STING activation, we analyzed a subset of interferon-stimulated genes (ISGs) (IFIT1, IFIT3, ISG15, OASL and STAT1) by qPCR and saw increased expression in both VPS13C^{KO} HeLa clones (Figure 4.1 B). This increase was no longer observed when cGAS (Figure 4.1 F) or STING (Figure 4.1 D) were knocked down by siRNA (Figure 4.1 C). Knockdown of cGAS or STING also decreased ISG expression in the WT cells, suggesting some basal level of STING signaling in HeLa cells.

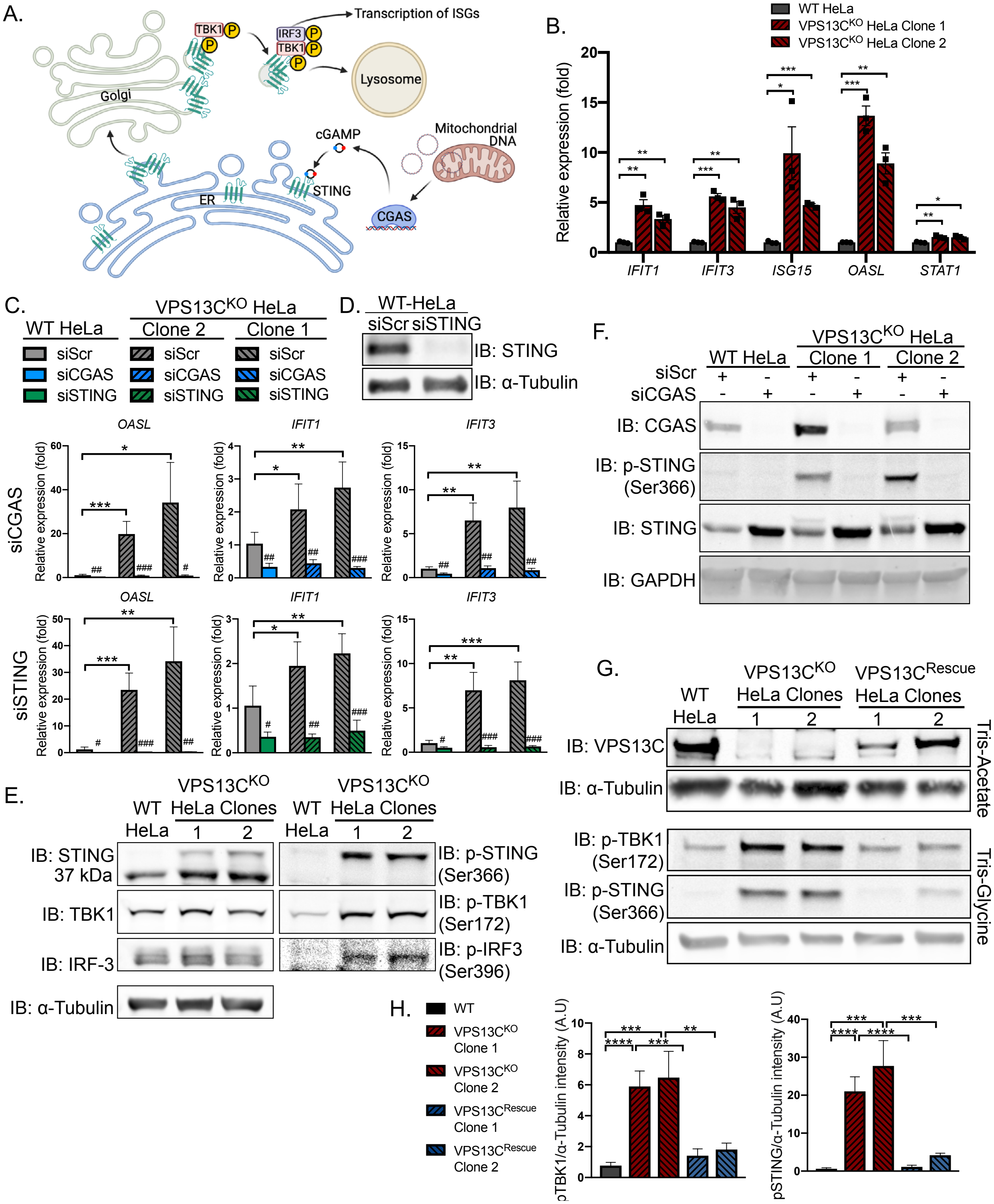

Figure 4.1 Loss of VPS13C results in activation of the cGAS/STING pathway

(A) Cartoon schematic of cGAS/STING signaling pathway and STING trafficking through the Golgi to lysosomes for degradation. Created with BioRender.com (B) qPCR of five ISG transcripts (*IFIT1, IFIT3, ISG15, OASL, STAT1*) shows increased expression in VPS13C^{KO} HeLa cells. N = 3 biological replicates. (C) qPCR of three ISG transcripts after treatment with siRNA against cGAS (top row) or STING (bottom row). N = 4 biological replicates. (D) Immunoblot showing efficiency of STING depletion after treatment with anti-STING siRNA. (E) Immunoblot showing increased levels of phosphorylated STING, TBK1, and IRF3, indicating activation of the cGAS/STING pathway. Note that the upper band in lanes 2 and 3 of the anti-STING blot corresponds to p-STING (lanes 2 and 3 of the p-STING blot. (F) Treatment of siRNA against cGAS significantly depletes cGAS and also returns p-STING to WT levels in the VPS13C^{KO} clones. cGAS-knockdown also causes an increase in total STING levels in both WT and VPS13C^{KO} cells. (G) Immunoblot showing lack of VPS13C band in VPS13C^{KO} cells and return of band in repaired VPS13C^{Rescue} clones. P-TBK1 and p-STING are returned toward WT levels in VPS13C^{Rescue} clones, quantified in (H). N = 3 biological replicates. * $P < 0.05$, ** $P < 0.01$, *** $P < 0.001$, **** $P < 0.0001$. # $P < 0.05$, ## $P < 0.01$, ### $P < 0.001$ in siCGAS or siSTING compared to siScr treated cells.

Upon binding to cGAMP, activated STING undergoes a conformational change, oligomerizes, traffics through the Golgi, and recruits the kinase TBK1, which phosphorylates STING at ser366 as well as itself at ser172(Liu et al., 2015b; Shang et al., 2019; Zhang et al., 2019). Phosphorylated STING subsequently recruits IRF3, which is phosphorylated and activated by TBK1(Liu et al., 2015b) and undergoes translocation to the nucleus to induce ISG expression (Figure 4.1 A)(Lin et al., 1998). Again consistent with cGAS-STING activation, phosphorylated forms of STING, TBK1, and IRF3 were all significantly elevated in VPS13C^{KO} HeLa cells (Figure 4.1 E). Total STING levels were also slightly increased (Figure 4.1 E). Additionally, siRNA knockdown of cGAS abolished STING-Ser366 phosphorylation in VPS13C^{KO} HeLa cells, while global levels of STING were slightly increased consistent with lower basal degradation in the absence of cGAS (Figure 4.1 F).

We next investigated whether activation of cGAS/STING could be rescued by VPS13C expression. Because transfected plasmid DNA can activate cGAS, we used CRISPR-Cas9 mediated homology directed repair (HDR) to correct one of the mutant VPS13C alleles in each of the VPS13C^{KO} clones (Figure 4.1 G). In clones in which VPS13C protein expression had been successfully restored (VPS13C^{Rescue}), phospho-STING and phospho-TBK1 were also restored to WT or near WT levels (Figure 4.1 G and H).

4.2.2 *Role of mtDNA escape in cGAS/STING activation in VPS13C^{KO} cells.*

Since mtDNA is a ligand for cGAS and hence an activator STING (West et al., 2015), and mutations in the single yeast Vps13 protein results in escape of mtDNA(Thorsness and Fox, 1993), we considered the possible role of mtDNA leakage in the activation of STING observed in VPS13C^{KO} cells. While VPS13C localization does not suggest a direct impact of this protein on mitochondrial function, recent studies have revealed that alteration of lysosome function can indirectly impact mitochondria (Hughes et al., 2020; Kim et al., 2021; Yambire et al., 2019). Moreover, mitochondrial defects were reported in Cos7 cells upon siRNA-mediated VPS13C knockdown (Lesage et al., 2016). To assess whether STING activation in VPS13C^{KO} cells was dependent on mtDNA, we treated VPS13C^{KO} cells with ethidium bromide (EtBr) for 72 hours to deplete mtDNA (Khozhukhar et al., 2018). The efficacy of this treatment was verified by qPCR of the D-loop region of mtDNA, which demonstrated a >97% depletion in mtDNA levels (Figure 4.3 A). Depletion of mtDNA in VPS13C^{KO} cells reversed both the elevated expression of ISGs and the increased levels of phospho-STING and phospho-TBK1 (Figure 4.2 A and B). Consistent with these results, we also observed a 2-4 fold increase in mtDNA (Figure 4.2 C) in cytosolic fractions of VPS13C^{KO} cells, in which absence of mitochondria was documented by immunoblotting for the mitochondrial marker HSP60 (Figure 4.3 B). However, no gross differences in either mitochondrial morphology or nucleoid structure or distribution in VPS13C^{KO} cells were observed by immunofluorescence (Figure 4.3 C). Together these results support the hypothesis that cytosolic mtDNA is a major source of cGAS/STING activation in VPS13C^{KO} cells.

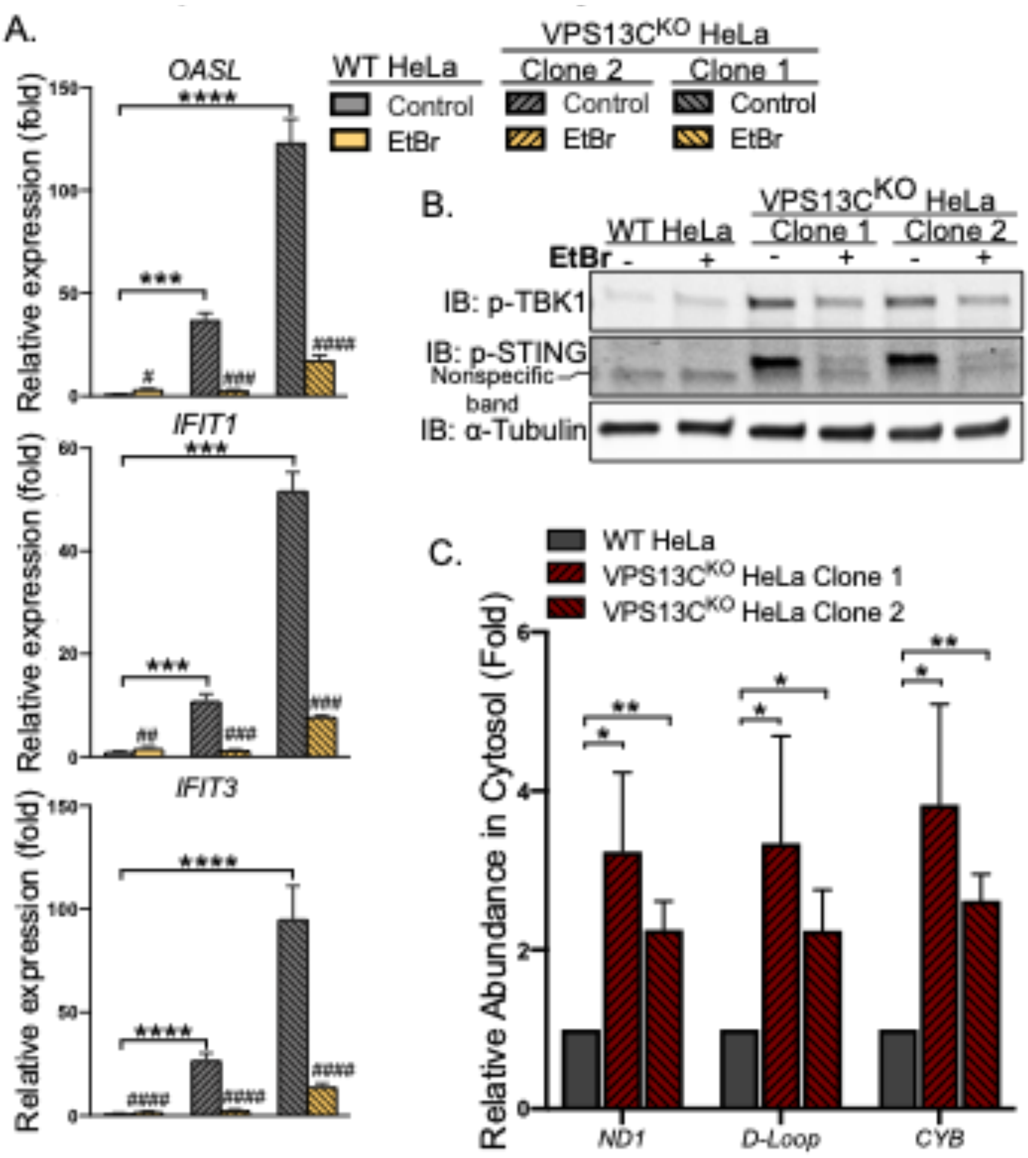

Figure 4.2 Activation of the cGAS/STING pathway in VPS13C^{KO} cells is dependent on increased cytosolic mtDNA

(A) qPCR of three ISG transcripts shows that depletion of mtDNA with EtBr reduces ISG levels in VPS13C^{KO} cells to or near WT levels. N = 3 biological replicates. (B) p-TBK1 and p-STING are reduced in EtBr treated VPS13C^{KO} cells. (C) Levels of three mtDNA amplicons (ND1, D-Loop, CYB) are elevated in the cytosolic fraction of VPS13C^{KO} cells. N = 3 biological replicates. * $P < 0.05$, ** $P < 0.01$, *** $P < 0.001$, **** $P < 0.0001$. # $P < 0.05$, ## $P < 0.01$, ### $P < 0.001$, #### < 0.0001 in EtBr compared to untreated cells.

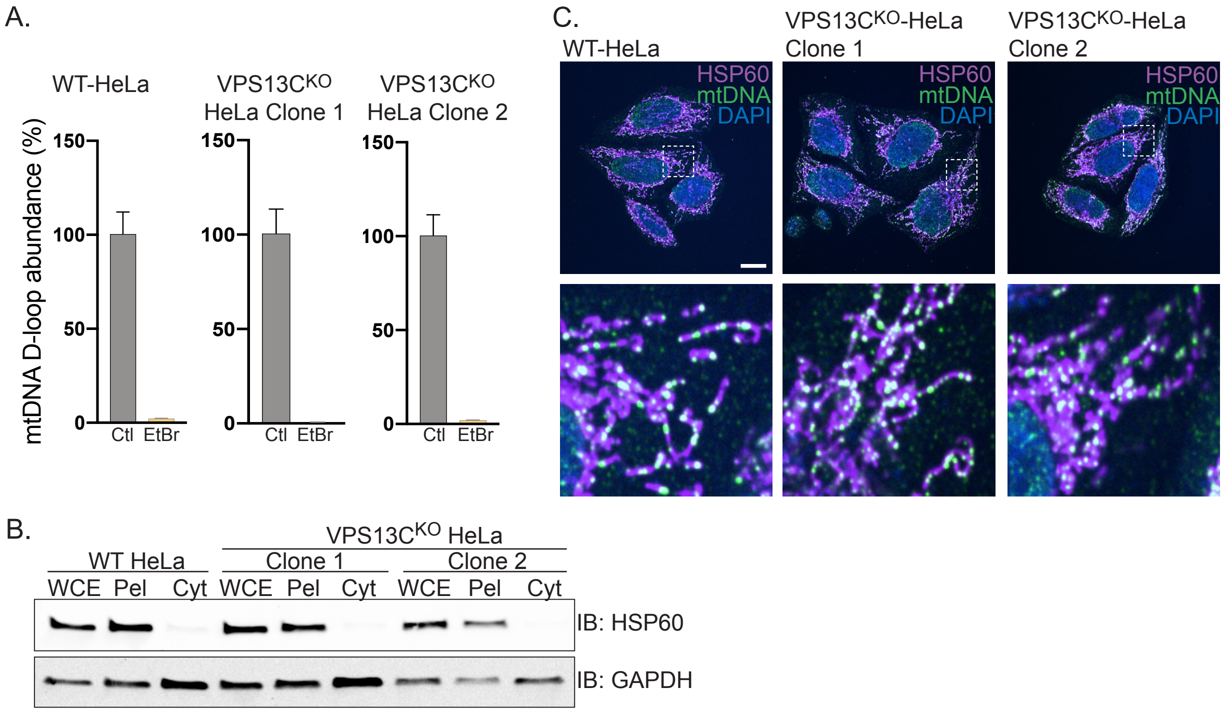

Figure 4.3 Control experiments for Figure 4.2 and normal mtDNA nucleoid morphology in VPS13C^{KO} cells

(A) qPCR of a D-Loop mtDNA amplicon shows efficient depletion of mtDNA after treatment with EtBr. (B) Immunoblot showing that mitochondrial marker HSP60 is present in the whole cell extract (WCE) and pellet (Pel) but absent in the cytosolic fraction (Cyt), while the cytosolic marker GAPDH is present in all fractions. (C) Immunofluorescence showing that mitochondria (magenta) and mtDNA nucleoids (green) have grossly normal morphology in VPS13C^{KO} HeLa cells. Scale bar 20 µm.

4.2.3 Steady-state change in the localization of STING in VPS13C^{KO} cells

The cGAMP-dependent oligomerization of STING leading to its activation also triggers its transport from the ER via the Golgi complex to lysosomes, where it is degraded leading to termination of signaling (Gonugunta et al., 2017; Gui et al., 2019). Thus, we tested whether the constitutive activation of STING observed in VPS13C^{KO} cells is accompanied by a change in its steady-state localization. As transient transfection, which involves acute introduction of plasmid DNA, can activate cGAS/STING, we generated cell lines stably expressing STING-GFP in control and VPS13C^{KO} HeLa cells via retroviral transduction. STING-GFP expression was similar in control and VPS13C^{KO} cells (Figure 4.5 A), and phospho-STING(Ser366) and phospho-TBK1(Ser172) remained elevated in the VPS13C^{KO} cells (Figure 4.5 B and C). In WT cells STING-GFP was almost exclusively localized to the ER, as expected (Figure 4.4 A and B). Treatment with cGAMP, the product of cGAS that binds to STING, caused STING to concentrate in a Golgi complex-like pattern within 15 minutes and then to disperse throughout the cells as punctate structures, previously shown to overlap in part with lysosomes over the next six hours (Figure 4.4 A)(Gui et al., 2019). In contrast, in VPS13C^{KO} cells (not exposed to exogenous cGAMP), STING-GFP already had a predominantly punctate localization (Figure 4.4 B and C) similar to the localization of STING-GFP in WT cells at 12 hrs after cGAMP stimulation (Figure 4.4 D and E).

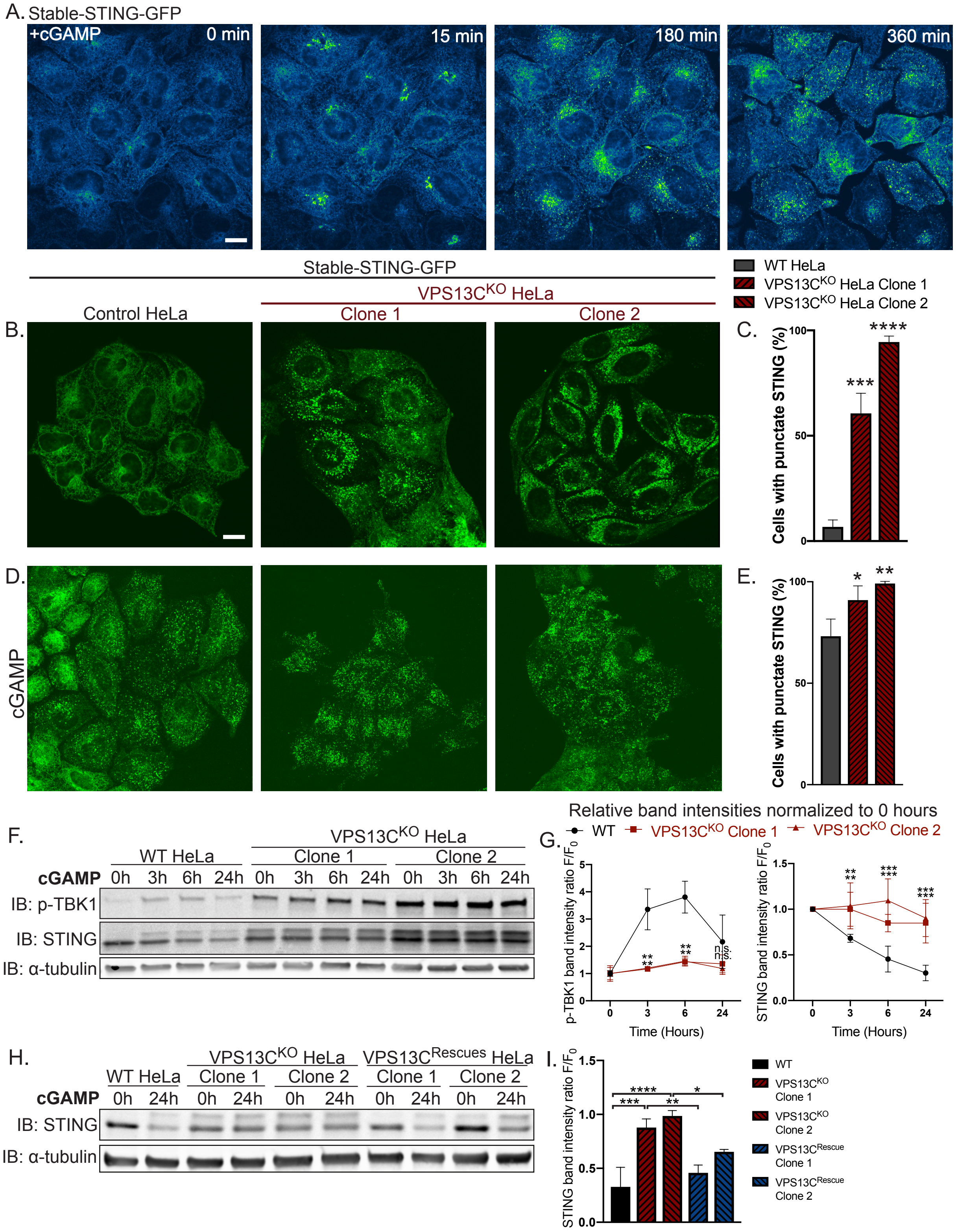
A. Stable-STING-GFP
+cGAMP
0 min
15 min
180 min
360 min
Stable-STING-GFP
VPS13C^KO HeLa
Control HeLa
Clone 1
Clone 2
B.
D.
cGAMP
WT HeLa
VPS13C^KO HeLa Clone 1
VPS13C^KO HeLa Clone 2
C.
Cells with punctate STING (%)
100
50
0
***
****
E.
*
**
F.
WT HeLa
VPS13C^KO HeLa
Clone 1
Clone 2
cGAMP 0h 3h 6h 24h 0h 3h 6h 24h 0h 3h 6h 24h
IB: p-TBK1
IB: STING
IB: α-tubulin
G.
Relative band intensities normalized to 0 hours
WT
VPS13C^KO Clone 1
VPS13C^KO Clone 2
p-TBK1 band intensity ratio F/F0
STING band intensity ratio F/F0
Time (Hours)
0 3 6 24
n.s.
n.s.
H.
WT HeLa
VPS13C^KO HeLa
VPS13C^Rescues HeLa
Clone 1
Clone 2
Clone 1
Clone 2
cGAMP 0h 24h 0h 24h 0h 24h 0h 24h 0h 24h
IB: STING
IB: α-tubulin
I.
STING band intensity ratio F/F0
1.5
1.0
0.5
0.0
****
*
***
**
WT
VPS13C^KO Clone 1
VPS13C^KO Clone 2
VPS13C^Rescue Clone 1
VPS13C^Rescue Clone 2

Figure 4.4 STING is activated and translocated out of the ER at baseline in VPS13C^{KO} cells (A) Selected frames from timelapse of stable STING-GFP in WT HeLa cells after treatment with 50 ug/mL cGAMP (Video 1). STING-GFP is localized in an ER-like pattern at 0 min post-treatment, traffics to a Golgi-like pattern 15 min post-treatment, a Golgi/vesicular pattern by 180 minutes post-treatment, and a largely vesicular pattern by 360 min. (B) Under unstimulated basal conditions, STING-GFP is localized in an ER distribution in WT HeLa cells but a vesicular distribution in the majority of VPS13C^{KO} cells. The percentage of cells with vesicular pattern is quantified in (C). N = 3 biological replicates. (D) treatment with cGAMP had only minimal effect on the already punctate distribution of STING-GFP in VPS13C^{KO} cells, but induces a vesicular pattern in the majority of WT cells, quantified in (E). N = 3 biological replicates. (F) In WT cells, treatment with 8 ug/mL cGAMP causes an increase in p-TBK1 at 3h and 6h timepoints and a return to baseline at 24h, along with a concomitant decrease in total STING levels over 24 hours as STING is degraded. In VPS13C^{KO} cells, the same treatment fails to cause a significant increase in p-TBK1, STING upper band (phospho-STING), or decrease in total STING levels. (G) Band intensity of p-TBK1 and STING at each timepoint is quantified relative to the 0h value for each cell line. N = 3 biological replicates. (H) Treatment with 8 ug/mL cGAMP in VPS13C^{Rescue} cells for 24h results in STING degradation closer to WT levels, but fails to induce significant STING degradation in VPS13C^{KO} cells, quantified in (I). N = 3 biological replicates. Scale bars 20 μM. * $P < 0.05$, ** $P < 0.01$, *** $P < 0.001$, **** $P < 0.0001$ compared to WT control.

We complemented these localization studies with biochemical experiments. In WT cells, addition of herring testes (HT)-DNA to activate cGAS (Figure 4.5 D), or of cGAMP to directly activate STING (Figure 4.4 F) resulted in the appearance of the upper STING band (the phosphorylated form) and increased levels of phospho-TBK1, but also in the degradation of total STING over time, as reported (Gonugunta et al., 2017; Gui et al., 2019). After 24 hrs, total levels of STING were reduced to 25% (for HT-DNA)(Figure 4.5 D and E) and 30% (for cGAMP)(Figure 4.4 F and G) of baseline and phospho-TBK1 also returned towards baseline (Figure 4.4 F and G). In contrast, in VPS13C^{KO} cells both phospho-TBK1 and phospho-STING were already elevated at baseline (total STING was also elevated), and addition of cGAMP did not promote degradation of these proteins (Figure 4.4 F and G). These differences from WT were rescued in the VPS13C^{Rescue} cells where the VPS13C mutation had been repaired (Figure 4.4 H and I). Collectively, these findings, i.e. elevated levels of both total STING and phospho-STING, and lack of its responsiveness to stimulation, raised the questions of whether the cGAS-STING pathway could still be activated by exogenous cGAMP in VPS13C^{KO} cells and whether degradation of STING might also be impaired.

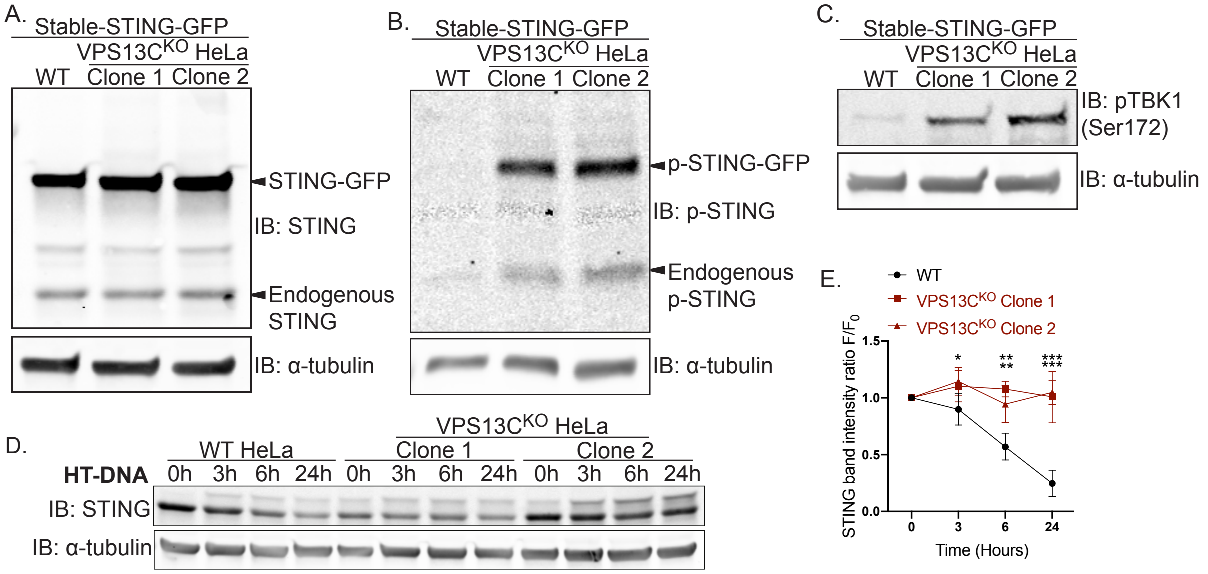

Figure 4.5 STING signaling is elevated in VPS13C^{KO} cells lines stably expressing STING-GFP

(A) Immunoblot showing similar levels of stable STING-GFP expression in WT and VPS13C^{KO} cells. (B) Immunoblot showing increased levels of p-STING in VPS13C^{KO} cells (both endogenous and STING-GFP). (C) Immunoblot showing increased levels of p-TBK1 in VPS13C^{KO} cells. (D) Timecourse of WT and VPS13C^{KO} cells treated with HT-DNA (500 ng/mL) for 0, 3, 6, and 24 hours. As with cGAMP treatment, STING is not significantly degraded in VPS13C^{KO} cells, quantified in (E). N = 2 biological replicates. * $P < 0.05$, ** $P < 0.01$, *** $P < 0.001$.

4.2.4 Silencing of cGAS unmasks cGAMP responsiveness of VPS13C^{KO} cells and reveals impaired STING degradation

To determine whether VPS13C^{KO} cells can still respond to cGAMP, these cells were treated with siRNA against cGAS (with scrambled siRNA as a control), to suppress basal STING activation. cGAS knock-down reverted STING-GFP to an ER localization (Figure 4.6 A and B), similar to untreated WT cells, while scrambled siRNA had no effect (Figure 4.6 A and C).

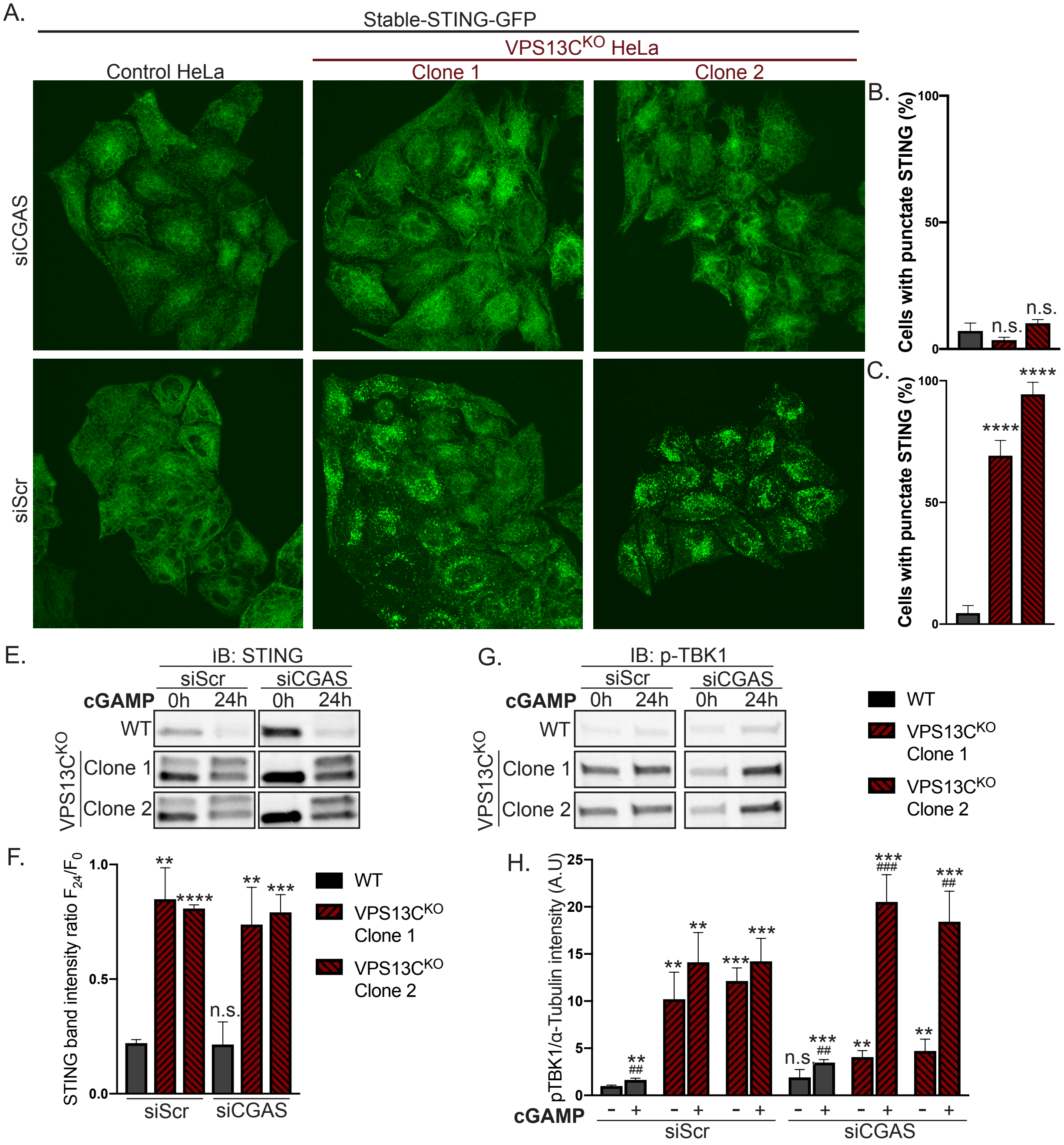
A.
Stable-STING-GFP
VPS13C^{KO} HeLa
Control HeLa
Clone 1
Clone 2
siCGAS
siScr
B.
Cells with punctate STING (%)
100
50
0
n.s.
n.s.
C.
Cells with punctate STING (%)
100
50
0
****
****
E.
IB: STING
siScr
siCGAS
cGAMP
0h
24h
0h
24h
WT
VPS13C^{KO}
Clone 1
Clone 2
G.
IB: p-TBK1
siScr
siCGAS
cGAMP
0h
24h
0h
24h
WT
VPS13C^{KO}
Clone 1
Clone 2
WT
VPS13C^{KO} Clone 1
VPS13C^{KO} Clone 2
F.
STING band intensity ratio F_{24}/F_0
1.0
0.5
0.0
**
****
n.s.
**
***
siScr
siCGAS
WT
VPS13C^{KO} Clone 1
VPS13C^{KO} Clone 2
H.
pTBK1/α-Tubulin intensity (A.U)
25
20
15
10
5
0
**
##
**
**
***
***
n.s
***
##
**
***
###
**
***
##
cGAMP
- + - + - + - + - + - +
siScr
siCGAS

Figure 4.6 Silencing of cGAS unmasks cGAMP responsiveness and reveals impaired STING degradation in VPS13C^{KO} cells

(A) Treatment with siRNA against cGAS returns STING-GFP to an ER distribution in VPS13C^{KO} cells, similar to untreated WT cells, quantified in (B), while siScr has no effect, quantified in (C). N = 3 biological replicates. (D) Immunoblot against STING in WT and VPS13C^{KO} cells treated with either scrambled siRNA or siRNA against CGAS, followed by treatment with 8 ug/mL cGAMP for 24h. Treatment with siRNA against CGAS returns STING to the unphosphorylated state in VPS13C^{KO} cells, rendering them responsive to cGAMP. In VPS13C^{KO} cells, the activation of STING is not followed by degradation, compared to WT cells. (E) Quantification of the total STING signal remaining at 24h after cGAMP treatment (F_{24}) relative to 0h (F_0). (F) Immunoblot against p-TBK1 under the same conditions as (E). WT cells behaved similarly in response to cGAMP treatment regardless of siScr or siCGAS pretreatment, with p-TBK1 levels returning to baseline after 24h of cGAMP treatment, as shown by the timecourse of Figure 5F and G. In VPS13C^{KO} cells pretreated with siScr, p-TBK1 remained at baseline after 24h of cGAMP treatment, presumably never having increased, based on the timecourse in Figure 5F and G. In VPS13C^{KO} cells pretreated with siCGAS however, p-TBK1 was significantly elevated after 24h of cGAMP, in accordance with the defect in STING degradation and continued STING signaling (E and F). (G) Quantification of p-TBK1 band intensity. N = 3 biological replicates. ** $P < 0.01$, *** $P < 0.001$, **** $P < 0.0001$ compared to untreated WT cells. ## $P < 0.01$, ### $P < 0.001$ value at 24h cGAMP treatment compared to corresponding 0h cGAMP treatment.

Biochemical experiments confirmed the restoration of responsiveness to cGAMP of VPS13C^{KO} cells. Both phospho-TBK1 (Figure 4.6 F and G), and phospho-STING (Figure 4.7 B), (also reflected by the upper total STING band (Figure 4.6 D)) returned to unstimulated WT levels following treatment with anti-cGAS siRNA (Full blot in Figure 4.7 A). Upon addition of cGAMP, we observed only a very modest reduction of total STING levels at 24h in VPS13C^{KO} cells compared to significant STING degradation in WT cells, suggesting a bona fide defect in STING degradation (Figure 4.6 D and E). Furthermore, phospho-TBK1(Figure 4.6 F and G) and phospho-STING (Figure 4.7 B) remained elevated in VPS13C^{KO} cells at 24h, in agreement with sustained STING signaling.

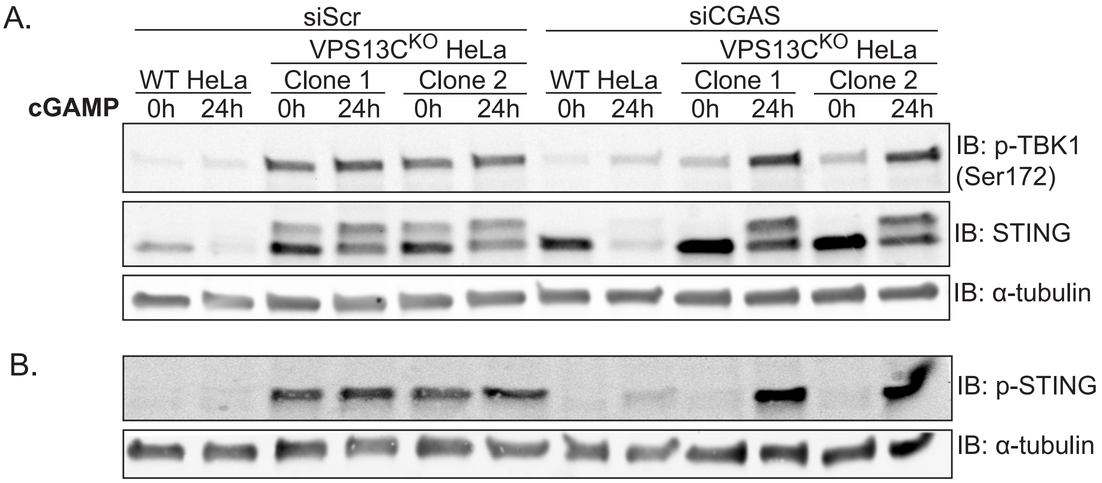

Figure 4.7 Silencing of cGAS unmasks cGAMP responsiveness and reveals impaired STING degradation in VPS13C^{KO} cells

(A) Intact blot from which the data from Figure 6E and 6G were extracted. (B) Immunoblot of the same samples as in (A) with anti p-STING antibody.

The defect in STING degradation did not reflect an overall defect in protein degradation in lysosomes, as we found no difference in the kinetics of EGFR degradation in response to EGF stimulation between VPS13C^{KO} and WT cells (Figure 4.8 A and B). Likewise, we found no difference in LC3 degradation after induction of macro autophagy by starving cells in EBSS (Figure 4.8 C). Interestingly, the ratio of lipidated LC3-II to LC3-I under basal conditions was increased in the VPS13C^{KO} cells (Figure 4.8 C), consistent with the reported property of activated STING to induce LC3 lipidation(Fischer et al., 2020; Gui et al., 2019).

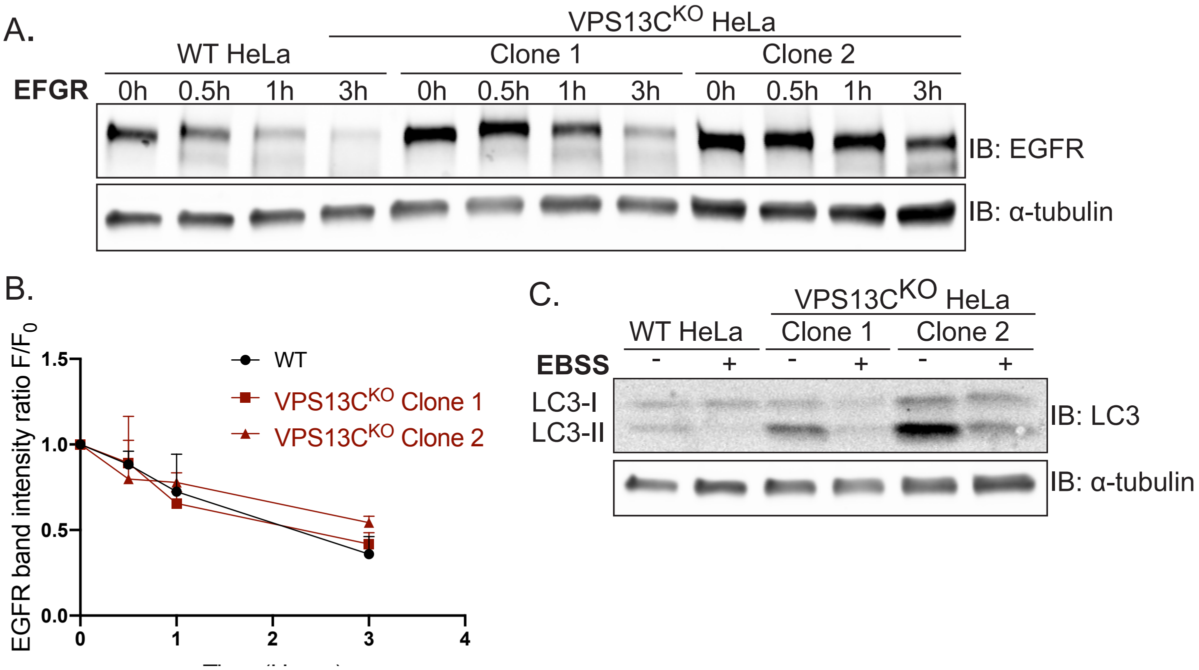

Figure 4.8 EFGR and LC3 degradation are not impaired in VPS13C^{KO} cells

(A) Immunoblot of EGFR in WT and VPS13C^{KO} cells treated with 100 ng/mL EGF for 0.5, 1, and 3h. (B) Quantification from (A) of band intensity at various timepoints (F) normalized to EGFR intensity at 0h (F_0), showing no defect in EGFR degradation kinetics. N = 3 biological replicates. (C) Immunoblot of LC3 in WT and VPS13C^{KO} cells after 6h starvation in Earle's Balanced Salt Solution (EBSS). Note that the ratio of lipidated LC3-II to LC3-I is elevated under basal conditions in VPS13C^{KO} cells, possibly downstream of STING activation as previously reported (Fischer et al., 2020; Gui et al., 2019).

4.3 Discussion

Our results support a role of VPS13C in regulating lysosome function and show that cellular perturbations produced by the absence of VPS13C result in activation of the cGAS-STING pathway. Such activation is of special interest as VPS13C is a PD gene and aberrant activation the cGAS-STING pathway has been implicated in PD pathogenesis(Sliter et al., 2018).

Our finding that the cGAS/STING signaling pathway is activated in VPS13C^{KO} cells adds to evidence for a potential involvement of this pathway in PD pathogenesis, as first suggested by studies of PINK1 and Parkin mouse models (Sliter et al., 2018). The role of activation of this pathway in PD, and more generally in neurodegenerative diseases, is an area of intense investigation (McCauley et al., 2020; Sliter et al., 2018; Weindel et al., 2020; Yu et al., 2020a). Our results suggest that the increase of STING signaling may result both from a leakage of mtDNA, which in turn would activate cGAS and thus generation of the STING ligand cGAMP, and from a delayed degradation of activated STING in VPS13C^{KO} cells. The mechanisms underlying this delayed degradation remain elusive. Presumably, STING must remain facing the cytosol (and not be internalized in the lysosomal lumen) to continue activating TBK1 and IRF3. A defective or incomplete fusion of STING-positive vesicles with late endosomes/lysosomes or a defect in the incorporation of STING into intraluminal vesicles of late endosomes are potential mechanisms. We speculate that alterations to the lysosomal lipidome may be responsible for these defects. Interestingly, defective lysosomal degradation of activated STING, leading to higher levels of innate immune signaling, was reported in cells deficient in C9orf72, another neurodegeneration gene associated with lysosomes (McCauley et al., 2020)

An attractive unifying scenario is that alteration of lysosome function is the most proximal consequence of VPS13C depletion, and that such alteration is upstream of mitochondrial dysfunction and STING activation. More specifically, defective lysosomal function may be the primary event leading to mtDNA leakage. A similar scenario may apply to STING activation by the absence of LRRK2, another PD protein implicated in lysosome function (Bonet-Ponce et al., 2020; Weindel et al., 2020). Indeed, it is now appreciated that genetic or pharmacologic disruption of lysosome function can lead to mitochondria dysfunction in a number of contexts (Hughes et al., 2020; Kim et al., 2021; Yambire et al., 2019). This cross-talk may be mediated by soluble factors (Hughes et al., 2020; Yambire et al., 2019) or by direct mitochondria lysosome contacts (Wong et al., 2018). It is also possible that leakage of mtDNA may occur during mitophagy by defective lysosomes. While mtDNA can escape directly from mitochondria into the cytosol (Riley and Tait, 2020; West and Shadel, 2017), as in the case of TFAM deficiency(West et al., 2015) or TDP-43 mutations (Yu et al., 2020a), it may also escape during the process of mitophagy/autophagy (Gkirtzimanaki et al., 2018; Oka et al., 2012).

An important question for future studies will be the elucidation of how these results relate to VPS13C loss-of-function in brain cells. VPS13C is ubiquitously expressed in cells of the central nervous system. In contrast, cGAS and STING are primarily expressed in microglia (Saunders et al., 2018). Interestingly, several other genes relevant to neurodegeneration are primarily expressed in microglia (Hickman et al., 2018). We have attempted to differentiate human iPS VPS13C^{KO} cells into microglia to assess potential defects resulting from the absence of VPS13C. However, while the differentiation protocol used was successful in yielding WT microglial cells, it failed to yield VPS13C^{KO} microglial cells, revealing a possible importance of

VPS13C in microglia. So far we have not observed obvious defects in VPS13C^{KO} mice, a finding that also applies to other PD genes, including PINK1 and Parkin (Sliter et al., 2018).

In conclusion, we have shown that in a model human cell line the absence of VPS13C results in late-endosome/lysosomal defects, as had been predicted by the localization of VPS13C at contacts between the ER and lysosomes and by the proposed role of VPS13C in mediating lipid exchange between these two organelles(Kumar et al., 2018; Leonzino et al., 2021). We have further discovered that these defects correlate with abnormally elevated STING signaling, most likely due to direct and indirect effects of the perturbation of lysosome function. While it remains to be seen how these findings can be generalized to other cell types and to intact tissues, our findings provide further support for the hypothesis that activation of innate immunity may be one of the factors involved in pathogenetic mechanisms resulting from mutations in PD genes.

Chapter 5: Discussion and future directions

5.1 VPS13: a novel class of lipid transfer proteins at membrane contact sites

We have established that the VPS13 family of proteins, which in humans play a critical role in maintaining the health of the central nervous system, function as lipid transfer proteins at distinct membrane contact sites. Specifically, we have established a role for VPS13C as a lipid transfer protein that operates at contact sites between the ER and late endosome/lysosomes, as well as between the ER and LDs (Kumar et al., 2018). VPS13A, which shares the ER-LD localization with VPS13C, is additionally found at ER-mitochondria contact sites. It was also recently shown by other members of our group that VPS13D also populates ER-mitochondria contact sites as well as ER-peroxisome contact sites. It remains to be determined whether VPS13B, which localizes to the Golgi, forms contact sites as well (Da Costa et al., 2020; Du et al., 2020).

Moreover, in a collaboration with the Reinisch Lab we have demonstrated that these proteins share a common structure in which an N-terminal fragment of the protein forms a wide (~20 Å) hydrophobic groove capable of binding phospholipids and transferring them between membranes(Kumar et al., 2018). This finding constitutes the first demonstration of structure and function for chorein-domain containing proteins and defines a new class of lipid transfer protein. A more recent cryo-electron microscopy (Cryo-EM) structure reveals that this groove runs uninterrupted along the entire N-terminal half of the protein, well suited for the bulk transfer of phospholipids between membranes(Li et al., 2020) (Figure 5.1). ATG2, an essential protein for autophagy with regions of high sequence homology to VPS13 proteins, has since been shown to also be a lipid transfer protein(Osawa et al., 2019; Valverde et al., 2019). In-situ cryo-EM images of VPS13C at its native localization at ER-Lysosome contact sites (unpublished data of lab member Shujun Cai) show that it forms bridges between membranes, suggesting that lipids may flow between membranes via the hydrophobic groove in a “tunnel model.”

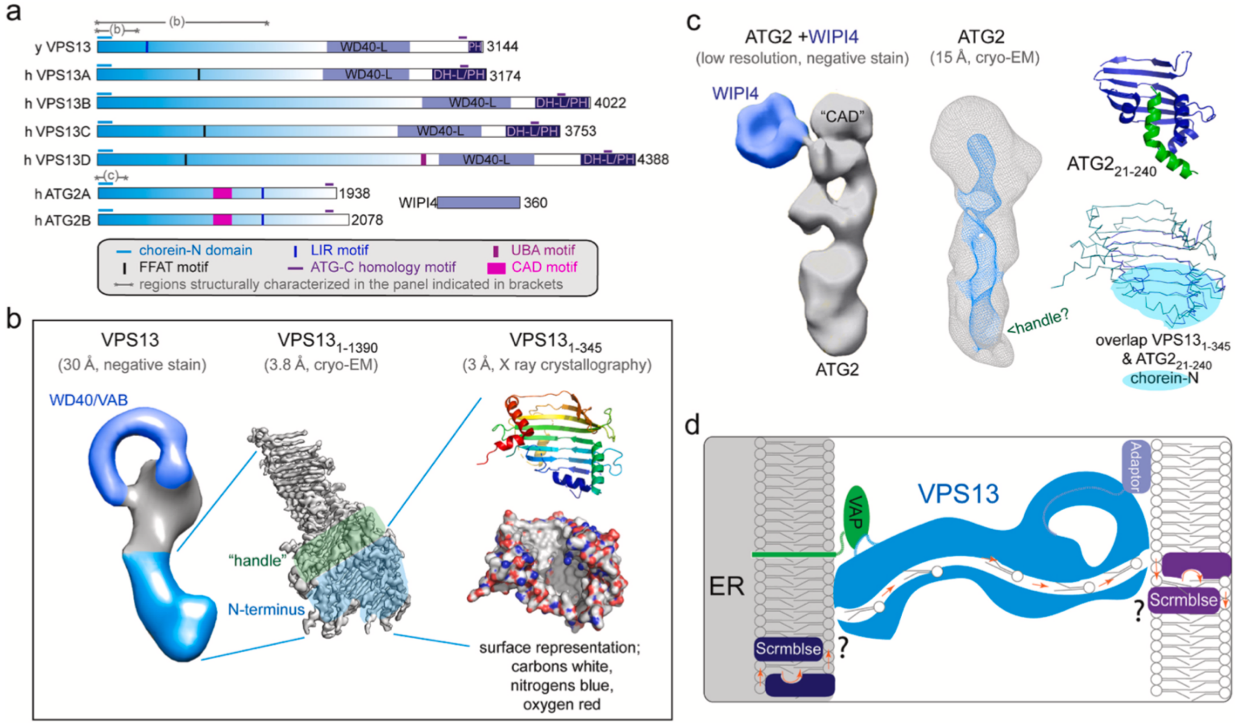

Figure 5.1 Structures and proposed function of VPS13 family and related proteins

A) Architecture of VPS13 and ATG2 proteins, including known and predicted domains and motifs. B) Negative stain of the entire Vps13 protein, cryo-EM and crystal structure of N-terminal portions demonstrate continuous hydrophobic channel capable of transferring phospholipids between membranes. C) Negative stain and cryo-EM of ATG2 with its binding partner WIPI4 (possibly analogous to the VPS13 β-propeller domain), showing similar extended hydrophobic cavity. D) Proposed model for VPS13-mediated lipid transfer, including the putative scramblases and accessory interacting proteins in the two tethered membranes. Figure adapted from (Leonzino et al., 2021)

5.2 Possible mechanisms driving lipid transfer

Major questions remain regarding the mechanistic details of lipid transfer by VPS13 proteins as well their specificity for different lipid classes. It remains unknown if the lipid transfer is bi-directional, unidirectional, or both depending on the specific VPS13 protein and context. Whether lipid transfer occurs by a passive mechanism, i.e. lipids flow along their concentration gradient, or by an active mechanism, is an area of ongoing investigation. Potential active mechanisms include accessory proteins functioning as lipid pumps, scramblases, membrane tension, or metabolic sinks in which the metabolism of a particular type of lipid in one membrane drives diffusion gradient-based transfer or counter-current transfer (Figure 5.2). Recently, VMP1 and TMEM41B were shown to function as scramblases that may partner with lipid transfer proteins to allow for continued lipid transfer(Ghanbarpour et al., 2021; Li et al., 2020). Theoretically, a scramblase, flippase, or floppase must be present in the receiving membrane to allow equilibration of the inner and outer leaflets. Such a partnership is likely to occur between ATG2, a VPS13-related lipid transfer protein, and ATG9, which has now been shown to be a scramblase, to facilitate membrane expansion of the growing autophagososome (Ghanbarpour et al., 2021; Maeda et al., 2020; Matoba et al., 2020).

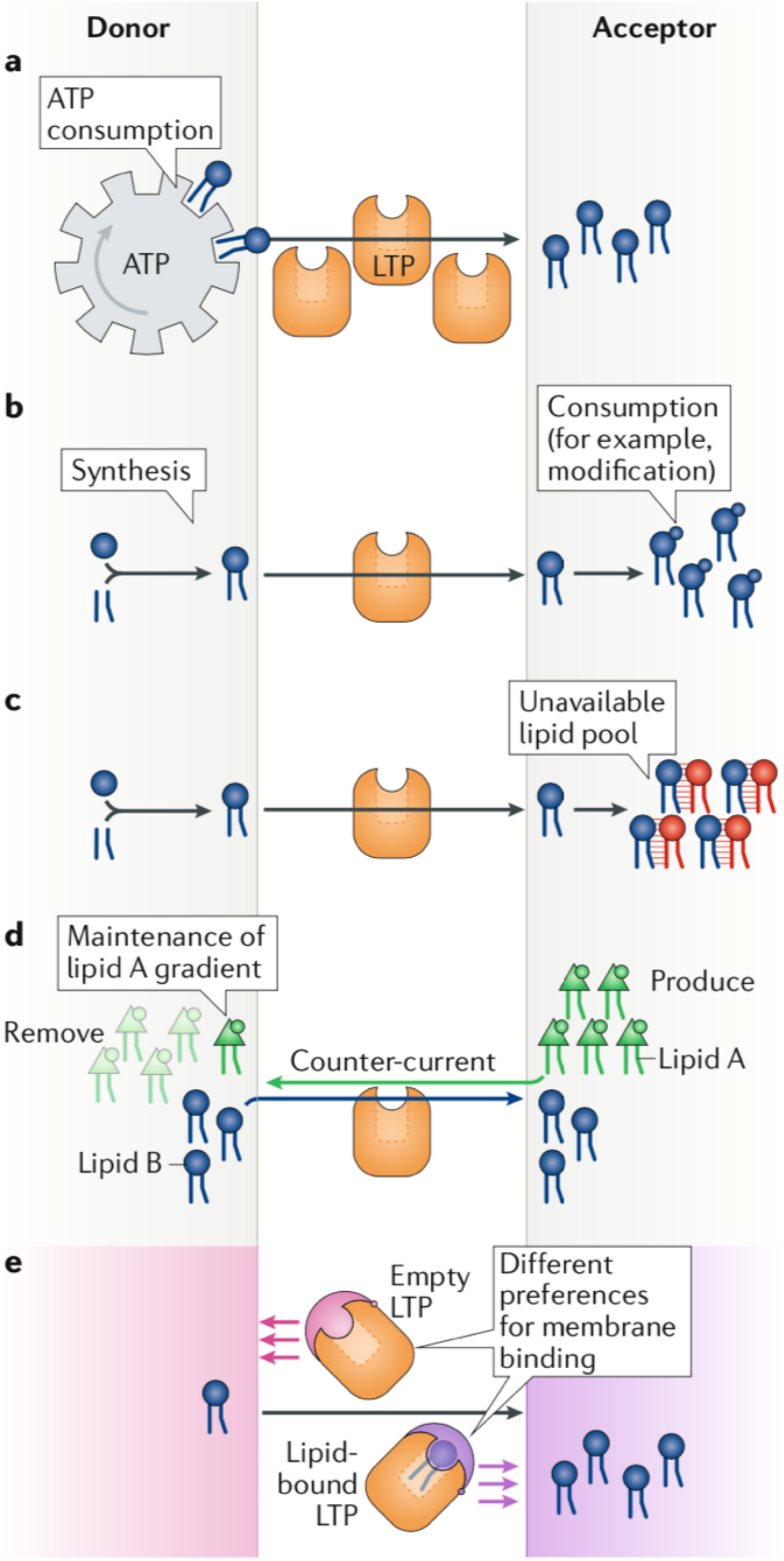
Donor
Acceptor
a
ATP consumption
ATP
LTP
b
Synthesis
Consumption (for example, modification)
c
Unavailable lipid pool
d
Maintenance of lipid A gradient
Remove
Produce
Counter-current
Lipid A
Lipid B
e
Empty LTP
Different preferences for membrane binding
Lipid-bound LTP

Figure 5.2 Possible mechanisms driving lipid transfer

Active transport of lipids between membranes can occur via a number of different mechanisms. A) ATP hydrolysis by accessory proteins can pump lipids through LTPs against a concentration gradient. B) and C) Lipids in the acceptor membrane can be either depleted through a metabolic process (B), or made unavailable by strong interactions with other lipids or proteins (C), thus generating a concentration gradient of the free lipid. D) Lipids can be transfer against their concentration gradient by a counter-current, in which one lipid flowing down its concentration gradient is exchanged for another flowing against its gradient. E) LTPs can change their conformation in response to binding specific lipids, and may have a preference for loading or unloading at specific membranes based on the local lipid or protein environment. Note that one or more scramblase, flippase, or floppase must be present on the donor and acceptor membranes in order allow continued flow of lipids. Figure adapted from (Wong et al., 2019)

5.3 Possible cellular functions of VPS13C germane to PD

5.3.1 Function of VPS13C in glial cells

Our findings that VPS13C loss-of-function results in perturbations to the lysosomal lipidome is consistent with its role as a lipid transfer protein at ER-late endosome/lysosome contact sites. Though we propose that these are the primary function and localizations of VPS13C, the cellular pathways impacted by this lipid transfer are yet to be fully elucidated. Our results suggest that VPS13C loss-of-function may have indirect effects on mitochondrial biology, triggering the release of mtDNA and subsequent activation of the cGAS/STING pathway. Though the mechanism by which loss of VPS13C triggers mtDNA release is not yet determined, this result is plausible given that yeast Vps13 was a hit in a screen for mutations that cause escape of mitochondrial DNA(Thorsness and Fox, 1993). Activation of the cGAS/STING pathway by mtDNA was recently shown to be central to PD pathogenesis in PINK1 and Parkin knockout mouse models exposed to additional mitochondrial stress(Sliter et al., 2018). Since neurons do not express cGAS or STING at detectable levels, (our unpublished data), the pertinent effects of cGAS/STING activation may either be systemic or mediated by glia in the CNS. Indeed, VPS13C seems to be highly expressed in microglia(Saunders et al., 2018) (our unpublished data), and it was recently shown in a drosophila model that cell-type specific deletion of Vps13 in microglia exacerbates α-synuclein pathology and neuron loss (Olsen and Feany, 2021). VPS13C may play other important roles in glia unrelated to the cGAS/STING pathway, related to its direct role in lysosomal lipid biology. Of not VPS13C was also a hit in multiple studies of the phagosomal proteome(Guo et al., 2015; Rogers and Foster, 2007; Shui et al., 2008), indicating a possible role in phagocytosis.

5.3.2 Lipid changes in relation to PD

Numerous lines of evidence have pointed to lipids playing a key role in PD pathogenesis (Brekk et al., 2020; Fanning et al., 2020). We observed multiple changes in the lipid composition of VPS13C^{KO} HeLa cells, both at the whole cell and lysosome-specific levels. Some of these changes, including whole cell loss of PE, and accumulation of Cer and HexCer, have been already been associated with PD (Calzada et al., 2016; Ishibashi et al., 2013; Manyam et al., 1988; Patel and Witt, 2017; Riekkinen et al., 1975; Taguchi et al., 2017; Tasseva et al., 2013). Of novel interest are the roles of the lysosome specific lipid BMP as well as ether-linked lipids in PD pathogenesis. It will be interesting to determine whether LRRK2 gain of function mutations, as well as other PD alleles, cause similar changes to BMP species as VPS13C mutations. A comparative study could be carried out with VPS13C^{KO} and LRRK2^{KI} iNeurons, which are being generated as part of a collaboration between the NIH and Jackson Labs. The downstream effects of these BMP changes should be characterized, including changes to ILV formation by electron microscopy, changes in function of BMP-binding proteins such as ALIX, Hsp70, NPC-2, ASM can be assayed. Of particular interest is the effect of VPS13C^{KO} or LRRK2 gain-of-function on exosome formation. Exosomes, a subset of extracellular vesicles, are heterogeneous in nature but generally consist of ILVs released into the extracellular space by fusion of MVBs with the plasma membrane (Kalluri and LeBleu, 2020). Exosomes have been proposed to play a number of roles in PD, including facilitating the intercellular spread of a-synuclein, mediating neuroinflammation, and transporting micro RNAs(Pinnell et al., 2021; Yu et al., 2020b; Yuan and Li, 2019). Disruption of lysosome function by inhibition of VPS34 causes increased secretion of exosomes which contain higher levels of BMP as well as amyloid precursor protein C-terminal fragments (Miranda et al., 2018).

Additionally, further study should be conducted on whether the changes in lysosomal lipid composition, especially the alterations in BMP and ether lipids, molecules known to have intriguing biophysical characteristics (Jimenez-Rojo and Riezman, 2019; Showalter et al., 2020), are directly related to observed increased STING signaling in the VPS13C^{KO} HeLa cells. A number of questions are of particular mechanistic interest: 1) whether the mtDNA leakage occurs from mitochondria directly, or rather from defective lysosomes with internalized mitochondria resulting from mitophagy, and 2) whether the observed defect in STING degradation can be attributed to a defect of internalization of STING from the limiting membrane of lysosomes. The trafficking steps of STING after it leaves the Golgi remain poorly elucidated, and an intriguing hypothesis is that STING-positive vesicles fuse with lysosomes, which would maintain the topology of STING and allow it to continue signaling. STING would then have to be internalized in order to be degraded, which may occur by ILV formation or a related process. BMP has been shown to mediated this process (Matsuo et al., 2004).

5.3.3 A role for VPS13C in de novo membrane formation?

The large hydrophobic channel in VPS13 and other chorein domain containing proteins is well suited for the rapid flow of lipids required for formation of de novo membranes. Indeed, multiple VPS13 family members have been shown to be essential for specific processes that require de novo membrane formation. The best-known of these is the role of ATG2 in expansion of the autophagosome membrane (Figure 5.3). Yeast Vps13 is essential for formation of the prospore membrane during sporulation, while VPS13B is required for acrosome membrane growth in sperm cells. If VPS13A, VPS13C, and VPS13D have roles in analogous processes, they are yet to be identified.

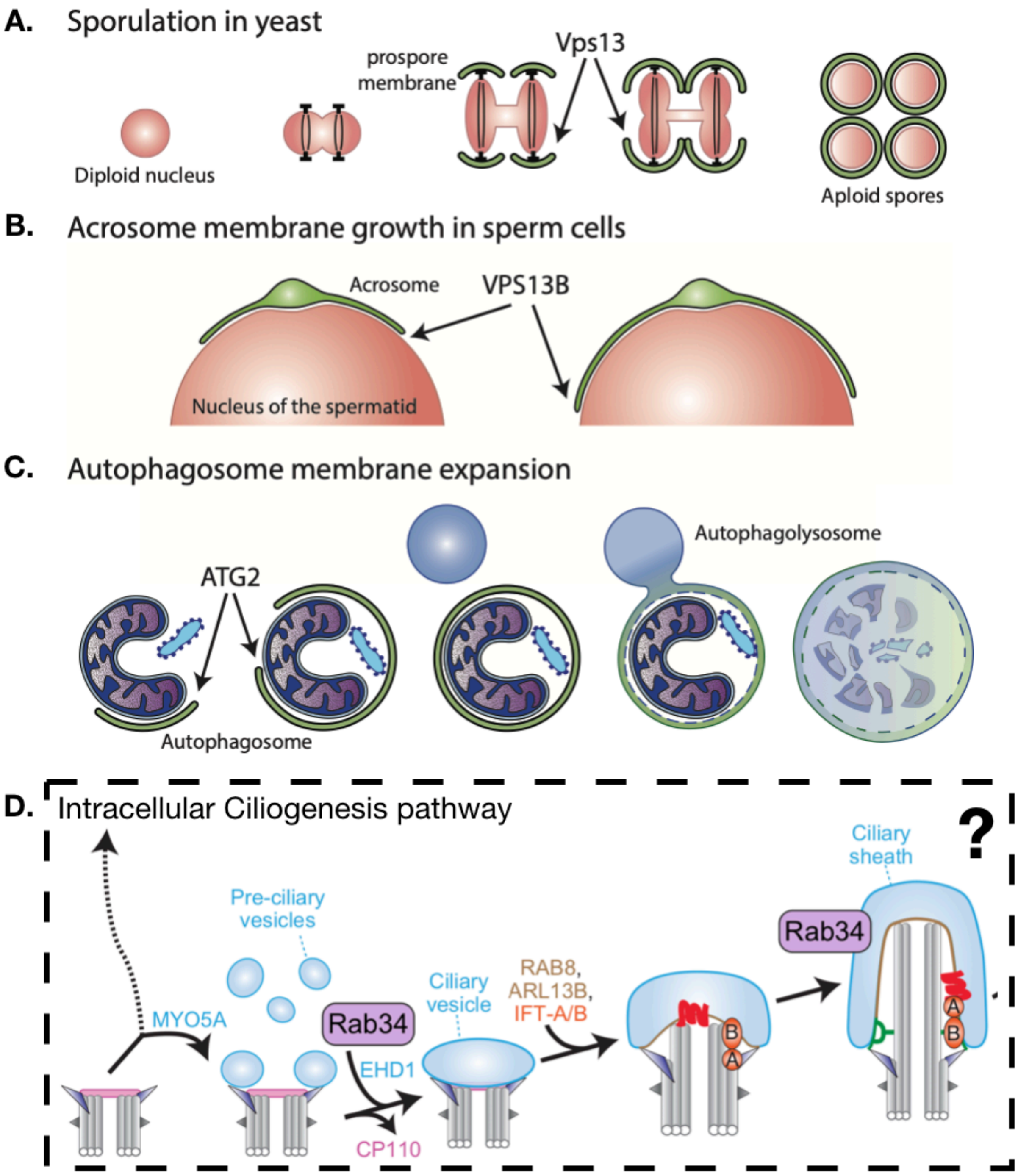
A.
Sporulation in yeast
prospore membrane
Vps13
Diploid nucleus
Aploid spores
B.
Acrosome membrane growth in sperm cells
Acrosome
VPS13B
Nucleus of the spermatid
C.
Autophagosome membrane expansion
ATG2
Autophagolysosome
Autophagosome
D.
Intracellular Ciliogenesis pathway
?
Pre-ciliary vesicles
MYO5A
Rab34
EHD1
CP110
Ciliary vesicle
RAB8,
ARL13B,
IFT-A/B
B
A
Ciliary sheath
Rab34
A
B

Figure 5.3 Known and hypothesized roles of VPS13 family and ATG2 in de novo membrane expansion.

(A) Yeast Vps13 is involved in the process of sporulation, in which the prospore membrane grows in a Vps13 dependent manner around daughter nuclei. (B) Expansion of the acrosome membrane in mammalian spermatids requires VPS13B. (C) Expansion of the autophagic membrane requires ATG2. (D) The process of intracellular ciliogenesis involves the growth of a de novo membrane, the ciliary sheath, around the growing cilia, a membrane growth process analogous to (A, B, and C). It is an intriguing hypothesis that VPS13 or VPS13-related proteins may be involved in growth of the ciliary sheath and promote ciliogenesis. Adapted from (Leonzino et al., 2021) and (Ganga et al., 2021).

One intriguing hypothesis is that VPS13C may play a role in the process of intracellular ciliogenesis. VPS13C was identified in a proximity labeling screen of cilia, and the process of intracellular ciliogenesis requires growth of a double membrane structure called the ciliary sheath – a process that has striking similarity to acrosome, prospore membrane, and autophagosome biogenesis (Figure 5.3). Cilia have recently been proposed to play a role in LRRK2-associated PD, as LRRK2 gain-of-function mutations impair the ciliation of cholinergic neurons in the striatum that participate in a neuro-protective circuit to maintain the health of dopaminergic neurons in the SNpc (Dhekne et al., 2018).

5.4 Conclusion

We have established the VPS13 proteins as founding members of a new class of LTPs which high relevance to human health and disease, especially of the central nervous system. Furthermore, we have established a key role for VPS13C in lysosomal lipid biology and innate immune signaling with relevance to PD. Though much remains to be learned about the fascinating role of VPS13C in cell biology and PD, these findings represent a significant step forward in our understanding of intracellular lipid transfer and common pathways of PD pathogenesis.

Chapter 6: Materials and Methods

6.1 Materials and methods for Chapter 2

6.1.1 Reagents

Halo tag ligands JF549 and JF647 were a kind gift from L. Lavis (Janelia Farm, Ashburn, VA). Human VPS13A (transcript variant 1A) and VPS13C (transcript variant 2A) ORFs were purchased from Origene. The following constructs were kind gifts: mito-BFP and mCherry-Rab7a from G. Voeltz (University of Colorado Boulder, Boulder, CO; 49151 and 61804, respectively; Addgene), GFP-Rab5a from M. Zerial (Max Planck Institute of Molecular Cell Biology and Genetics, Dresden, Germany), EGFP-Rab7 from B. van Deurs (University of Copenhagen, Copenhagen, Denmark), EGFP-Lamp1 from S. Ferguson (Yale University, New Haven, CT), RFP-Lamp1 from W. Mothes (Yale University, New Haven, CT), and Sec61b-GFP and RFP from T. Rapoport (Harvard University, Cambridge, MA). mCherry-VAPB was previously generated in our laboratory (Dong et al., 2016). All the other ORFs used are listed in Table S1. Primary antibodies against HA (3F10; Roche), VPS13A (NBP1-85641; Novus Biological), VPS13C (HPA043507; Sigma-Aldrich Prestige), and GAPDH (40-1246; Proteus) were purchased commercially. Secondary antibodies (Alexa Fluor 594– conjugated goat anti-rat and Alexa Fluor 594–conjugated donkey anti-goat) were purchased from Thermo Fisher Scientific.

All EM reagents were purchased from Electron Microscopy Sciences. Lipids were purchased from Avanti Polar Lipids: DOPC (850357), NBD-PE (810144), NBD-PS (810198), NBD-PA (810138), NBD-ceramide (810211), Rhodamine-PE (810150), DGS-NTA (Ni; 790404), PI(4,5)P_2 (840046), liver PE (840026), and NBD-cholesterol (810252).

6.1.2 Bioinformatic analysis

Secondary structure prediction was performed through Dis-Meta software (Huang et al., 2014), and structure prediction was performed through RaptorX (Källberg et al., 2012) and Phyre2 (Kelley et al., 2015).

6.1.3 Generation of constructs

The coding sequences for Vps13 from C. thermophilum corresponding with residues 1–335 or 1–729 were cloned from genomic DNA into a modified pET-Duet vector containing a C-terminal 6×His tag. The coding sequence corresponding with residues 1–1,390 was cloned into a pCMV-6 vector containing an N-terminal 3×FLAG tag. The coding sequence for Vps13 from S. cerevisiae corresponding with residues 1–1,350, or Vps13α, was amplified from genomic DNA and cloned using the same strategy. For Vps13α_{tethered}, the same sequence was fused the unstructured region of human E-Syt2 (649–739)–His$_6$, with the PH domain of rat PLCΔ (11–140) inserted after residue 689 using overlap extension PCR, and was cloned into a pCMV-6 vector containing an N-terminal 3×FLAG tag. E-Syt1 (93–327) containing the synaptotagmin, mitochondrial, and lipid-binding protein (SMP) lipid transport domain was fused to the PH domain of rat PLCΔ (11–140) and cloned into a pET-28a vector containing an N-terminal His$_6$ tag (Bian et al., 2018). Most constructs were generated with regular cloning protocols or through site-directed mutagenesis. Desired ORFs were amplified by PCR and inserted in vectors through enzymatic digestion and ligation. Unless otherwise stated, pmCherry and pEGFP (Takara Bio Inc.) were used as cloning vectors. Primer sets, enzymes, and vectors used for each construct are displayed in Table S1.

For internal tagging of VPS13A, the EGFP ORF was removed from the pEGFP vector through enzymatic digestion (XhoI/NotI), and the PCR-amplified VPS13A sequence was ligated. Restriction enzyme sites (SalI/ApaI) were introduced after aa 1,372 via site-directed mutagenesis, and mCherry or Halo tag ORFs flanked by short linkers (AGG/GG) were then inserted. Mito-GFP and mito-mCherry were generated from mito-BFP by swopping the fluorescent protein sequence using BamHI/NotI digestion. Internally tagged VPS13C and chimeric constructs were generated using InFusion cloning according to the manufacturer's protocol. All ORFs were fully sequenced after cloning.

6.1.4 Protein expression and purification

A fragment of Vps13 from C. thermophilum corresponding with residues 1–335 or 1–729 was expressed in BL21 (DE3) Codon Plus (Agilent) Escherichia coli cells. Cells were grown at 37°C to an OD_{600} of 0.6–0.8, when protein expression was induced with 0.5 mM IPTG, and then cells were cultured at 18°C for another 16–20 h. Selenomethionine-substituted protein was expressed as previously described (Doublié, 1997). Cells were pelleted, resuspended in buffer A (20 mM Hepes, pH 7.8, 300 mM NaCl, 20 mM imidazole, and 5% glycerol) containing 1× complete EDTA-free protease inhibitor cocktail (Roche) and lysed in an Emulsiflex-C5 cell disruptor (Avestin). Cell lysates were clarified via centrifugation at 27,000 g for 30 min. To collect the protein, supernatant was incubated with Ni-NTA resin (QIAGEN) for 1 h at 4°C, and then the resin was washed with 3× 10 bed volumes of buffer A. Retained protein was eluted from the resin with buffer A supplemented with 300 mM imidazole, concentrated in a 10-kD molecular weight cutoff (MWCO) Amicon centrifugal filtration device, and loaded onto a Superdex 75 16/60 column (GE Healthcare) equilibrated with buffer B (20 mM Hepes, pH 7.8, and 150 mM NaCl) or buffer C (20 mM Hepes, pH 7.8, 300 mM NaCl, 1 mM Tris(2-carboxyethyl)phosphine [TCEP], and 2.5% glycerol) for selenomethionine-substituted protein. Peak fractions containing pure Vps13 were recovered and concentrated.

$Vps13_{1-1,390}$ (from C. thermophilum), Vps13α, and $Vps13\alpha_{tethered}$ (from S. cerevisiae) were each expressed in Expi293 cells (Invitrogen) according to the manufacturer's instructions for 72 h. Cells were pelleted, resuspended in buffer C, and lysed via sonication. Cell lysates were clarified via centrifugation at 27,000 g for 20 min, and the supernatant was incubated with preequilibrated anti-FLAG M2 affinity resin (Sigma-Aldrich) for 2 h. The resin was washed with 3× 10 bed volumes of buffer C and incubated for 16 h with buffer C containing 1 mM ATP and 2 mM $MgCl_2$. The protein was eluted with buffer C supplemented with 0.2 mg/ml 3× FLAG peptide and concentrated in a 30-kD MWCO Amicon centrifugal filtration device.

6.1.5 Protein crystallization, structure determination, and refinement

Crystals of selenomethionine-substituted C. thermophilum Vps13 (1–335 Δ228–236)–His_6 at 6 mg/ml were grown at 37°C using the sitting-drop vapor-diffusion method. Equal volumes of protein were mixed with mother liquor containing 100 mM Bis-Tris, pH 6.5–6.7, and 34–38% 15/4 pentaerythritol ethoxylate (Hampton). Drops were equilibrated against well solution containing 1 M NaCl. Crystals, which belonged to spacegroup $P2_1$ and had two copies of $Vps13_{crystal}$ in the asymmetric unit, were harvested in cryoloops and flash frozen. Diffraction data were collected at NE-CAT beamline 24-ID-C at the Advanced Photon Source and integrated, scaled, and merged using X-ray Detector Software and Aimless (Kabsch, 2010; Evans, 2011). Data from four crystals collected at the selenium edge were combined in the final dataset, and phases were calculated using the single-wavelength anomalous dispersion method

(Hendrickson, 1991). We identified the selenium positions, calculated experimental phases and density-modified maps, and built an initial model using the phenix AutoSol pipeline (Adams et al., 2010). Because diffraction was anisotropic, completeness dropped abruptly at resolutions better than 3 Å, and maps calculated at higher resolutions showed no improvement. Accordingly, the final model was refined to a resolution of 3.0 Å by multiple cycles of manual model rebuilding in coot (Emsley et al., 2010) followed by positional, individual isotropic B-factor and Translation Libration Screw refinement with phenix.refine (Adams et al., 2010) using secondary structure restraints. We modeled residues 2–228, 231–240, and 247–317 (numbering refers to the loop-deleted sequence) in one of the $\text{Vps13}_{\text{crystal}}$ copies; some of these residues were disordered in the second copy (2–5, 19–22, 30–33, 221–226, and 240–247) and were omitted from the model. Figures were made using PyMOL (v1.8.6.0) software.

6.1.6 Lipid analysis of Vps13 by mass spectrometry

S. cerevisiae Vps13α (aa 1–1,350) was expressed and purified as described above with the following modifications. Following immunoprecipitation, FLAG resin–bound Vps13α was washed with 3× 20 bed volumes of buffer C for 30 min, after which it was incubated for 16 h with buffer containing 1 mM ATP and 2 mM $MgCl_2$. The protein was eluted with buffer supplemented with 0.2 mg/ ml 3× FLAG peptide and concentrated in a 30-kD MWCO Amicon centrifugal filtration device to ~0.5 mg/ml final concentration. The purified protein sample was sent to Avanti Polar Lipids for lipid analysis, where bound lipids were extracted in 2:1 (vol/vol) methanol:choroform. The chloroform layer was dried, and lipids were reconstituted with internal standards for phosphatidylcholine (PC), PE, phosphatidylinositol (PI), phosphatidylserine (PS), phosphatidic acid (PA), phosphatidylglycerol (PG), sphingomyelin (SM), triacylglycerol (TAG), DAG, and cholesterol-d7 for quantitation. The sample was injected into a reversed-phase C8 column with a gradient elution profile for the resolution of each lipid class and detected by an AB Sciex 5500 tandem mass spectrometer. The molecular species of lipids was quantified based on internal standards and summed by lipid class.

6.1.7 Liposome preparation

To prepare liposomes for lipid-transfer assays, lipids in chloroform were mixed in the indicated ratios and dried to thin films. Lipids were subsequently reconstituted in buffer containing 20 mM Hepes, pH 7.8, 300 mM NaCl, and 5% glycerol at a total lipid concentration of 1 mM and subjected to 10 freeze–thaw cycles alternating between liquid nitrogen and 37°C water bath. Crude liposomes were then extruded through a polycarbonate filter with 100 nm pore size a total of 21 times via a mini extruder (Avanti Polar Lipids) and used within 24 h.

6.1.8 In vitro lipid-binding assay

1 µl of either NBD-labeled PE, PS, PA, cholesterol, or ceramide (1 mg/ml in methanol) was incubated with 19 µl purified Vps13α or $\text{Vps13}_{\text{crystal}}$ (2 mg/ml) for either 30 min at 37°C or 2 h at 4°C. Samples were visualized on 10% native PAGE gels. NBD fluorescence was visualized using an ImageQuant LAS4000 (GE Healthcare), and total protein was visualized with Coomassie staining.

6.1.9 In vitro lipid-transfer FRET assays

Lipid-transfer reactions were performed in 50-µl volumes in 96-well plates (Nunc) containing a protein:lipid ratio of 1:400, with 0.125 µM protein, 25 µM donor liposomes (61%

DOPC, 30% liver PE, 2% NBD-PS, 2% Rhodamine-PE, and 5% DGS-NTA [Ni]) and 25 µM acceptor liposomes (65% DOPC, 30% liver PE, and 5% PI(4,5P)$_2$). Fluorescence intensity of NBD was measured via excitation at 460 nm and detection at 538 nm every 1 min for 30 min at 30°C using a Synergy H1 Plate Reader (BioTek). All data were corrected by subtracting baseline from no-protein controls.

For the liposome fusion–control assay, we used the dithionite assay as previously described (Weber et al., 1998; Shi et al., 2013). Briefly, after performing a lipid-transfer reaction (as described above), 2.5 µl freshly prepared dithionite buffer (100 mM dithionite [Sigma-Aldrich] in 50 mM Tris, pH 10) was added to reactions, and NBD fluorescence was monitored for an additional 20 min.

The turbidity assay, which rules out fusion and hemifusion, was performed as previously described (Bian et al., 2018). We used the same constructs and concentration of proteins and liposomes in the same volume as for the lipid-transfer assay. Following addition of the protein to the liposomes, absorbance at 405 nm was measured every 30 s for 10 min; then, cocktail (10 µl) containing 1.8 M imidazole and 1.15 mg/ml proteinase K (Sigma-Aldrich) was added, and absorbance was monitored for an additional 10 min. All data were corrected by subtracting background signal before protein addition.

6.1.10 Cell culture and transfection

HeLa and Cos-7 cells (obtained from ATCC) were maintained at 37°C in a humidified atmosphere at 5% of CO_2 in DMEM (Thermo Fisher Scientific) supplemented with 10% FBS (Thermo Fisher Scientific), 100 U/ml penicillin, 100 mg/ml streptomycin, and 2 mM GlutaMAX (Thermo Fisher Scientific). EXPI293 were grown in EXPI293 expression medium upon constant shaking. All cell lines were routinely tested and always resulted as free from mycoplasma contamination.

6.1.11 Generation of 2×HA-tagged VPS13A and VPS13C CRISPR– knock-in HeLa cell line

For the insertion of a 2×HA tag in the endogenous locus of either VPS13A or VPS13C in HeLa cells, asymmetric single-stranded DNA (ssDNA) donor repair templates designed as described by Richardson et al. (2016) were used. Cas9-mediated cut was directed by single-guide RNA obtained by mixing a fluorescent tracrRNA ATTO 550 (IDT) and a specific CRISPR RNA (crRNA; see Table S1). Ribonuclear complexes were obtained by incubating the two RNA components with the purified Cas9 (IDT) and the donor ssDNA (see Table S1) and then transfected into low-passage HeLa cells using Mirus TransIT-X2 transfection reagent. 24 h after transfection, cells containing the fluorescent tracrRNA were selected by FACS sorting, and single positive cells were seeded in 96-well plates. Single clones were allowed to grow and then were tested for HA expression by Western blotting. Positive clones were used for subsequent IF. As expected for such large proteins (>360 kD), the endogenous levels of expression are so low that a conventional IF protocol with rat anti-HA primary antibody (MBL) followed by Alexa Fluor 594–conjugated goat anti-rat secondary antibody did not produce a signal strong enough to be detected by microscopy. To amplify the signal, an additional incubation with a tertiary Alexa Fluor 594–conjugated donkey anti-goat antibody was used. Moreover, to improve the signal-to-noise ratio, each of the antibodies used was subjected to a clearing procedure as follows: WT HeLa cells were fixed in 4% PFA, washed in 50 mM glycine in PBS, double-rinsed in PBS, and then scraped in PBS containing 1% BSA and 1% Triton X-100. Antibodies were added to the fixed cell lysate at a concentration 3.5× higher than the final concentration used for IF and were incubated by rotation on a wheel overnight at 4°C. Cell debris were then pelleted by spinning the tubes at 17,000 g for 20 min at 4°C, and the supernatant containing cleared antibodies was diluted 3.5× in PBS containing 1% BSA.

6.1.12 Fixed- and live-cell imaging

For microscopy, cells were seeded on glass-bottomed Mat-Tek dishes (Mat-Tek Corporation) 5,500/cm^2 in complete media without antibiotics and transfected 16 h later with FugeneHD (Promega). Spinning-disk confocal imaging was performed 20–24 h after transfection using a Nikon Ti-E inverted microscope equipped with the Improvision UltraView VoX system (PerkinElmer) and controlled by Volocity (Improvision) software. Images were acquired with a Plan Apochromat objective (60× 1.45 NA). During imaging, cells were maintained in live-cell imaging buffer (Thermo Fisher Scientific) in a humidified atmosphere at 37°C.

Halo tag ligands JF549 and JF647 were used at a final concentration of 200 nM. Cells were incubated with the dye for 1 h, rinsed, and then incubated in complete media for 1 h before imaging. For dextran internalization, cells were incubated with 10 µg/ ml dextran–Alexa Fluor 488 or dextran–Alexa Fluor 647 (3,000 molecular weight; Thermo Fisher Scientific) for 30 min or overnight in complete culture media. Live staining of lipid droplets with BODIPY 493/503 (Sigma-Aldrich) was performed in complete media (final concentration of 1 µM) for 20 min at 37°C followed by a 10-min wash in complete media right before imaging. For staining of lipid droplets with LipidTox reagent (Thermo Fisher Scientific) in fixed cells, cells were fixed in freshly prepared PFA (4% in phosphate buffer, pH 7.5) for 20 min at room temperature and then washed in PBS. PBS-diluted LipidTox reagent was added to cells following manufacturer's instructions.

6.1.13 Correlative fluorescence and EM microscopy

Cells were seeded on gridded glass-bottomed Mat-Tek dishes and transfected with VPS13A^mCherry and GFP-Sec61β as described above. Cells expressing VPS13A and showing doughnut-shaped structures positive for both VPS13A and the ER marker were identified with the spinning-disk microscope (see above for settings) and localized on the grid using the transmitted light channel. Cells were then fixed in 2.5% glutaraldehyde–0.1 M sodium cacodylate and post-fixed with 1% OsO_4 in 1.5% $K_4Fe(CN)_6$ and 0.1 M sodium cacodylate, followed by en bloc staining with 2% uranyl acetate, dehydration in ethanol, and embedding in Embed 812. Using the grid as a guide, the selected cells were identified under a light microscope and then cut and contrasted with uranyl acetate and lead citrate. Samples were imaged with a Philips CM-10 transmission electron microscope. ER–lipid droplet contact sites (defined as region of <20 nm distance between membranes) were counted and measured in length using iTEM software (Olympus).

6.1.14 Image processing, analysis, and statistics

Florescence images presented are representative of cells imaged in at least three independent experiments and were processed with FIJI (ImageJ; National Institutes of Health) software. Unsharp Mask and Gaussian blur filters were applied on some of the images presented, and the dimension of higher-magnification insets were doubled using the Scale function of FIJI.

Quantifications were performed on unprocessed single-plane ROIs of 400 μm^2 obtained from at least three independent experiments. Area of overlap between VPS13A signal and ER or mitochondria were obtained by generating a mask of the thresholded signal from Sec61β or mito-

BFP channels, respectively, and then adding this mask on the thresholded VPS13A channel. The percentage of VPS13A signal within the mask over the total thresholded VPS13A signal area was then calculated. ER–mitochondria contacts were quantified with an analogous approach, generating a mask of the thresholded mito-BFP channel and calculating the percentage of the thresholded Sec61β-positive area that overlaps with that mask. Quantification of the area of overlap between endogenous VPS13A-HA or VPS13C-HA signal with mitochondria or late endosomes was performed by making a mask of the thresholded signal from Mito-GFP or EGFP-Rab7 signal and adding this mask on the thresholded HA channel. The percentage of HA signal within the mask over the total thresholded HA signal area was then quantified on a per-cell basis. Comparisons between conditions were conducted using one-way ANOVA followed by Tukey's honest significant difference test using GraphPad Prism software.

For the evaluation of ER–lipid droplet contacts in EM images, three cells per condition from two independent experiments were analyzed. For each cell, a single section of the middle plane of the cell was used. Statistical analysis was performed with Prism. Groups were compared using a two-tailed Student's t test, and results were deemed significant when $P > 0.05$.

6.2 Materials and methods for Chapter 3 and 4

6.2.1 DNA plasmids

A plasmid containing codon-optimized cDNA encoding human VPS13C, with a Halo protein flanked by SacII restriction enzyme sites after amino acid residue 1914, was generated by and purchased from GenScript Biotech. mCherry-Rab7a was obtained from Addgene (#61804). mCherry-Rab7a^{Q67L} and mCherry Rab7a^{T22N} were generated in our lab as previously reported (Guillen-Samander et al., 2019). Lamp1-mGFP was obtained from Addgene (#34831). GFP-VPS13C$^{\beta prop}$ was generated in our lab as previously described (Kumar et al., 2018). For CRISPR mediated gene editing, candidate guide RNAs (gRNAs) against the human VPS13C genomic locus were identified using Benchling. gRNAs were ordered as complementary single-stranded oligonucleotides from Integrated DNA Technologies (IDT) then cloned into the PX459 plasmid (Addgene plasmid #62988) using a one-step ligation protocol (Ran et al., 2013), and gRNAs were sequence verified using the U6 forward promoter. For CRISPR repair of the mutated VPS13C locus, gRNA was ordered (IDT) that incorporated a single nucleotide insertion present in one VPS13C allele in both of the VPS13C^{KO} clones. This was again cloned into the PX459 plasmid (Addgene plasmid #62988) using a one-step ligation protocol (Ran et al., 2013). To generate pMX-STING-GFP, STING-V1 plasmid was obtained from Addgene (Addgene #124262) and the STING coding sequence was amplified by PCR and ligated into pEGFP-N1 by using XhoI and SacII restriction sites. The STING-GFP coding sequence was then cut from the pEGFP-N1 backbone and ligated into a pMXs-IRES-Blasticidin Retroviral Vector backbone (RTV-016, Cell Biolabs) using XhoI and NotI restriction sites. Oligos used in this study are listed in Table S1. All oligos were purchased from IDT.

6.2.2 Antibodies

Primary antibodies used: mouse α-tubulin (T5168, Sigma-Aldrich), rabbit calnexin (ADI-SPA-860-D, Enzo), rabbit cathepsin D (Ab75852, Abcam), rabbit CGAS (D1D3G, CST), mouse DNA (CBL186, EMD Millipore), rabbit EEA1 (PA1063A, Thermo), mouse GAPDH (1D4, Enzo), mouse GM130 (610822, BD), rabbit HSP60 (12165S, CST), rabbit IRF3 (D83B9, CST), mouse LAMP1 (H4A3, DSHB), rabbit Phospho-IRF3 (S396) (4D4G, CST), rabbit Phospho-STING (S366) (D7C3S, CST), rabbit Phospho-TBK1 (S172) (D52C2, CST), rabbit Rab7 (D95F2, CST), rabbit STING (D2P2F, CST), rabbit TBK1 (D1B4, CST), rabbit VPS13C (custom, Proteintech)

6.2.3 Cell culture and transfection

HeLa-M cells were cultured at 37°C in 5% CO_2 and DMEM containing 10% FBS, 100 U/ml penicillin, 100 mg/ml streptomycin, and 2 mM L-glutamine (all from Gibco). For live-cell imaging experiments, cells were seeded on glass-bottomed dishes (MatTek) at a concentration of 35,000 cells per dish and transfected after 24h using FuGene HD (Promega). For biochemical experiments, cells were plated at such density so as to be approximately 90% confluent at the time of lysis. Transfection of siRNA was accomplished using Lipofectamine RNAiMax (ThermoFisher). Introduction of cGAMP was accomplished using Lipofectamine RNAiMax (ThermoFisher) as previously reported (Swanson et al., 2017). Transfection of HT-DNA was accomplished using Lipofectamine 2000 (ThermoFisher). Plat-A cells for retroviral packaging were cultured at 37°C in 5% CO_2 and DMEM containing 10% FBS, 1 100 U/ml penicillin, 100 mg/ml streptomycin, 2 mM L-glutamine, 1 μg/mL puromycin, and 10 μg/mL blasticidin.

6.2.4 Generation of Stable STING-GFP cells using retrovirus

For retroviral packaging, 5 x 10^6 Plat-A cells (Cell Biolabs) were plated on a 10 cm plate in media without antibiotics. The following day, cells were transfected with 9 µg of pMX-STING-GFP using Fugene HD (Promega). Retroviral supernatant was collected 72 hours post transfection, supplemented with Polybrene (8 µg/mL), and passed through 0.22 µm filter to remove cellular debris before being added to WT and VPS13C^{KO} HeLa cells. After 24 hours, retroviral supernatant was removed and replaced with fresh DMEM complete. After an additional 24 hours, HeLa cells were FACS sorted to enrich for GFP positive cells.

pMX-STING-GFP

6.2.5 Generation of CRISPR-KO and CRISPR-KI rescue cell lines

Early passage HeLa-M cells were transfected with 1.5 µg of PX459 plasmid (Addgene plasmid #62988) containing a single guide RNA (sgRNA) against VPS13C using Lipofectamine 2000 (ThermoFisher). At 24h post-transfection, cells were selected in complete DMEM containing 2 µg/mL puromycin. At 48h and 72h post transfection, media was replaced with fresh puromycin-containing media. After three days of puromycin selection, single clones were obtained using serial dilution and then screened by immunoblot. Two clonal cell lines lacking VPS13C by immunoblot were selected. Genomic DNA was extracted using a DNAeasy kit (Qiagen) and a ~500 bp portion around the predicted CRISPR cut site was amplified by PCR and purified by NucleoSpin Gel and PCR Clean-up kit (Macherey-Nagel). This fragment was then ligated into an EGFP-N1 vector using Xho1 and Apa1 restriction sites and transformed into DH5-

a competent cells. After plating the transformation mix onto agar plates, >48 bacterial colonies per clone were submitted for Sanger sequencing to maximize the probability of sequencing all alleles. Frameshift mutations leading to premature stop codons were identified by Sanger sequencing.

To rescue VPS13C expression we used CRISPR mediated homology directed repair (HDR) using a single-stranded oligo DNA nucleotide (ssODN) as previously described (Okamoto et al., 2019). Briefly, a gRNA was synthesized that incorporated a single nucleotide insertion present in one VPS13C allele in both of the VPS13C^{KO} clones. An ssODN corresponding to the WT VPS13C sequence flanking the insertion was generated. Both VPS13C^{KO} clones were transfected with 1μg of PX459 plasmid containing the gRNA against the mutant VPS13C allele and 100 pmols of ssODN. Puromycin selection and single clone selection was performed as above, and rescue of protein expression was confirmed by immunoblot.

6.2.6 Live-cell imaging

Prior to imaging, growth medium was removed and replaced with live-cell imaging solution (Life Technologies). All live-cell imaging was performed at 37°C in 5% CO_2. Imaging was performed using an Andor Dragonfly spinning-disk confocal microscope equipped with a plan apochromat objective (63x, 1.4 NA, oil) and a Zyla scientific CMOS camera. For lysotracker experiments, cells were incubated in 50 nM LysoTracker Red DND-99 (ThermoFisher) in complete DMEM for 30 minutes, washed twice with media, then imaged in live-cell imaging solution.

6.2.7 *Immunofluorescence*

WT and VPS13CKO HeLa cells were plated on glass coverslips and fixed in a pre-warmed (37°C) solution of 4% paraformaldehyde in PBS for 15 minutes at room temperature, permeabilized with 0.1% (v/v) Triton X-100 in PBS for 10 minutes at room temperature, and blocked using filtered PBS containing 1% (w/v) BSA for an hour at room temperature. Coverslips were then incubated with antibodies against DNA (CBL186, EMD Millipore, 1:150) and HSP60 (12165S, CST, 1:1000), diluted in filtered PBS containing 1% BSA at 4°C overnight, followed by 3 x 5-minute washes in PBS. Secondary antibodies (1:1000, Alexa fluorophores 488 and 555, Invitrogen) were incubated in PBS containing 1% BSA for 1 hour at room temperature and removed by 3 x 5-minute washes in PBS. Finally, coverslips were mounted onto slides using ProLong Gold Antifade Mountant with DAPI (ThermoFisher P36935) and allowed to cure overnight at room temperature prior to imaging.

6.2.8 *Image processing and analysis*

Fluorescence images were processed using Fiji software (ImageJ; National Institutes of Health). For quantification of lysotracker images (Figure 1E), cells were outlined manually and their average fluorescence intensity measured. Intensities were then normalized such that the average intensity of the WT cells was 1. For quantification of stable STING-GFP cells, cells with a reticular ER or vesicular pattern were counted manually and the percentage of cells with punctate STING-GFP distribution was calculated.

6.2.9 Synthesis of colloidal dextran-conjugated superparamagnetic iron-oxide nanoparticles (SPIONs)

SPIONs were synthesized according to the following protocol: 10 mL of aqueous 1.2 M $FeCl_2$ and 10 mL of 1.8 M $FeCl_3$ were combined in a 500 mL glass beaker with magnetic stirring, followed by slow addition of 10 mL of 30% NH_4OH. This mixture was stirred for 5 minutes and during this time a dark brown sludge formed. The beaker was then placed on a strong magnet to allow the particles to migrate towards the magnet. The supernatant was removed and the particles resuspended in 100 ml water, followed by repeated separation on the magnet. This was step was repeated two more times. Particles were then resuspended in 80 mL of 0.3 M HCl and stirred for 30 minutes, followed by addition of 4 g of dextran and another 30 minutes of stirring. Particles were transferred into dialysis bags and dialyzed for 48 hours in milliQ water with water changes approximately every 12 hours. The resulting mixture was then centrifuged at 19,000 g for 15 minutes to remove large aggregates. Supernatant containing nanoparticles was stored at 4˚C.

6.2.10 Immunoblotting

HeLa-M cells were lysed on ice by repeating pipetting in RIPA buffer (150 mM NaCl, 10 mM Tris, 0.5 mM EDTA, 0.5% NP40) supplemented with Protease Inhibitor Cocktail (Roche) and PhosStop phosphatase inhibitor (Roche)), and centrifuged at 15,000 x *g* for 10 min at 4˚C and the post-nuclear supernatant collected. Total protein content was then measured by Pierce BCA assay (ThermoFisher). Samples were prepared for immunoblot at equal protein concentrations in 3x Laemmli buffer (188 mM Tris-HCl, 3% SDS, 30% glycerol, 0.01% bromophenol blue, 15% β-mercaptoethanol) and denatured at 95°C for five minutes. Proteins were separated on Mini PROTEAN TGX 4-20% tris-glycine gels (Bio-Rad) before transfer to nitrocellulose membranes at 4˚C for one hour at 120 volts in transfer buffer containing 25 mM Tris, 192 mM glycine, 20% methanol in milliQ water. Total protein was then visualized using Ponceau stain (company) and then blocked in 5% milk in TBS containing 0.1% Tween-20 (TBST) for one hour. Membranes were then incubated with primary antibodies in 2.5% milk in TBST overnight at 4˚C. The next day, membranes were washed 3x in TBST and then incubated with secondary antibodies conjugated to IRdye 800CW or IRdye 680CW (1:10,000, Licor) in 2.5% milk in TBST at 22˚C for one hour, washed 3x with TBST, 3x with TBS, and then imaged using a Licor Odyssey Infrared Imager.

For VPS13C immunoblotting, post-nuclear supernatant was collected as above. Samples for WB were prepared using NuPAGE LDS Sample Buffer and Reducing Agent (Thermofisher) and incubated for 10 minutes at 70 ˚C. Proteins samples were separated on NuPage Tris-Acetate 3-8% gels and then transferred onto nitrocellulose membranes at 4˚C overnight at 0.5 mA in NuPAGE transfer buffer containing 20% methanol. Membranes were blocked as above and incubated with primary antibody against VPS13C (Proteintech, custom, 1:400) in 2.5% milk in TBST for 2h at 22˚C. Membranes were incubated with secondary antibodies, washed, and imaged as above.

6.2.11 Purification of lysosomes with dextran-conjugated SPIONs

WT and VPS13C^{KO} HeLa cells were plated on 4x 15 cm plates at 3.5 x 10^{6} cells per dish. The following day, the culture medium (DMEM) was exchanged for fresh DMEM containing 10 mM HEPES and 10% SPION solution by volume for 4 hours (pulse). The medium was then changed back to fresh DMEM and after 15 hours (chase) the cells were washed twice with PBS and then scraped into 5 mL of PBS on ice. Cells were then centrifuged at 1000 rpm for 10 min at 4˚C. PBS was removed and the cell pellet was resuspended in 3mL homogenization buffer (HB)(5mM Tris, 250 mM Sucrose, 1mM EGTA pH 7.4) supplemented with protease inhibitor cocktail (Roche) immediately before use) and passed through a manual cell homogenizer (Isobiotec, 10 cycles, 10-micron clearance) to generate a total cell lysate. The lysate was centrifuged at 800 g for 10 min at 4˚C, and the supernatant was loaded onto a magnetic LS column (Miltenyi Biotec) pre-equilibrated with 1mL of HB. The column was washed with 5 mL HB, then removed from the magnetic rack and eluted with 3 successive aliquots of 1mL HB forced through with positive pressure. The eluate was then centrifuged at 55,000 rpm for 1 hr at 4˚C to pellet the lysosome fraction and the resulting pellet was resuspended in 200 µL of mass-spectrometry grade water (ThermoFisher) and flash frozen. Fluorescence images of nanoparticles were obtained using FluoreMAG A ferrofluid (Liquids Research Ltd) with a 4 hour pulse and 15 hour chase.

6.2.12 Lipid extraction for mass spectrometry lipidomics

Mass spectrometry-based lipid analysis was performed by Lipotype GmbH (Dresden, Germany) as described (Sampaio et al. 2011). Lipids were extracted using a two-step chloroform/methanol procedure (Ejsing et al. 2009). Samples were spiked with an internal lipid standard mixture containing: cardiolipin 16:1/15:0/15:0/15:0 (CL), ceramide 18:1;2/17:0 (Cer), diacylglycerol 17:0/17:0 (DAG), hexosylceramide 18:1;2/12:0 (HexCer), lyso-phosphatidate 17:0 (LPA), lyso-phosphatidylcholine 12:0 (LPC), lyso-phosphatidylethanolamine 17:1 (LPE), lysophosphatidylglycerol 17:1 (LPG), lyso-phosphatidylinositol 17:1 (LPI), lyso-phosphatidylserine 17:1 (LPS), phosphatidate 17:0/17:0 (PA), phosphatidylcholine 17:0/17:0 (PC), phosphatidylethanolamine 17:0/17:0 (PE), phosphatidylglycerol 17:0/17:0 (PG), phosphatidylinositol 16:0/16:0 (PI), phosphatidylserine 17:0/17:0 (PS), cholesterol ester 20:0 (CE), sphingomyelin 18:1;2/12:0;0 (SM), triacylglycerol 17:0/17:0/17:0 (TAG). After extraction, the organic phase was transferred to an infusion plate and dried in a speed vacuum concentrator. The 1st step dry extract was re-suspended in 7.5 mM ammonium acetate in chloroform/methanol/propanol (1:2:4, V:V:V) and the 2nd step dry extract in a 33% ethanol solution of methylamine in chloroform/methanol (0.003:5:1; V:V:V). All liquid handling steps were performed using Hamilton Robotics STARlet robotic platform with the Anti Droplet Control feature for organic solvents pipetting.

6.2.13 Mass spectrometry data acquisition

Samples were analyzed by direct infusion on a QExactive mass spectrometer (Thermo Scientific) equipped with a TriVersa NanoMate ion source (Advion Biosciences). Samples were analyzed in both positive and negative ion modes with a resolution of $R_{m/z=200}$=280000 for MS and $R_{m/z=200}$=17500 for MSMS experiments, in a single acquisition. MSMS was triggered by an inclusion list encompassing corresponding MS mass ranges scanned in 1 Da increments (Surma et al. 2015). Both MS and MSMS data were combined to monitor CE, DAG and TAG ions as ammonium adducts; PC, PC O-, as acetate adducts; and CL, PA, PE, PE O-, PG, PI and PS as deprotonated anions. MS only was used to monitor LPA, LPE, LPE O-, LPI and LPS as deprotonated anions; Cer, HexCer, SM, LPC and LPC O- as acetate adducts.

6.2.14 Data analysis and post-processing

Data were analyzed with in-house developed lipid identification software based on LipidXplorer (Herzog et al. 2011; Herzog et al. 2012). Data post-processing and normalization were performed using an in-house developed data management system. Only lipid identifications with a signal-to-noise ratio >5, and a signal intensity 5-fold higher than in corresponding blank samples were considered for further data analysis.

6.2.15 Measurement of di-22:6-BMP and di-18:1-BMP

Targeted high resolution UPLC-MS/MS was used to accurately quantitate total di-22:6-BMP (the sum of its 3 isoforms). Total di-18:1-BMP was measured as well. Quantitation was performed by Nextcea, Inc. (Woburn, MA) using authentic di-22:6-BMP and di-18:1-BMP reference standards. Di-14:0-BMP was employed as an internal standard.

6.2.16 Depletion of mtDNA

HeLa cells were treated with 2 μg/mL ethidium bromide (EtBr) in DMEM for 8 days. Medium was replaced every two days, and cells were passaged on day 4. At day 8, cells were lysed and total DNA, RNA, and protein were collected. Depletion of mtDNA and levels of ISG transcripts were assayed using qPCR as described below.

6.2.17 Quantitative PCR

RNA was extracted using the RNeasy plus micro RNA extraction kit followed by reverse transcription using iScript cDNA synthesis Kit (Bio-Rad). Equal amounts of DNA and corresponding primers (Supplementary Table 1) were used for quantitative PCR (qPCR) using SYBR Green Master Mix. For each biological sample, two technical replicates were performed. Mean values were normalized against the β-actin threshhold cycle (Ct) value to calculate ΔCt. The ΔCt of each sample was then compared to the ΔCt of the WT sample to generate the ΔΔCt value. Relative expression was then analyzed using the $2^{-\Delta\Delta Ct}$ method and the relative fold change was plotted with the WT samples given a value of 1. To quantify mtDNA, DNA was extracted from total cell lysate and cytosolic fractions using DNeasy kit (Qiagen). DNA samples were each diluted 1:10 and corresponding primers (Supplementary Table 1) were used for quantitative PCR (qPCR) using SYBR Green Master Mix. Two technical replicates were performed for each biological sample and mean Ct values of mtDNA amplicons form cytosolic fractions were normalized against the corresponding total cell lysate hB2M (nuclear DNA control) Ct value. Relative copy number was determined by the $2^{-\Delta\Delta Ct}$ method and the WT mtDNA abundance was given a value of 1.

6.2.18 Fractionation of cytosol by centrifugation

Cytoplasmic buffer (CB, 150 mM NaCl, 50 mM HEPES, 1 mg/mL digitonin, pH 7.4) and lysis buffer (CB + 1% SDS supplemented with Protease Inhibitor Cocktail (Roche)) were prepared. HeLa cells were plated in 15 cm plates, 3.5 x 10^6 per plate. After 24 hours, cells were trypsinized and centrifuged at 1500 rpm for 5 min at 22 ˚C. Cells were resuspended in PBS and counted. For each genotype, 5 x 10^6 cells were collected and centrifuged at 1500 rpm for 5 min at 22 ˚C. Cells were resuspended in 1 mL PBS and 50 µL was transferred to a prechilled Eppendorf tube (WCE) and kept on ice. The remaining 950 µL was transferred to a prechilled Eppendorf tube and centrifuged at 4500 RPM for 5 min at 4 ˚C. The supernatant was removed and the cells were resuspended in CB and rotated for 10 min at 4 ˚C. Sample was centrifuged at

980 g for 3 min at 4 ˚C. The supernatant was transferred to a new Eppendorf and the pellet (Pel) was flash frozen for analysis. The supernatant was centrifuged at 17000 g for 10 min at 4 ˚C. The supernatant was again collected (Cyt). DNA was collected from these samples using a DNeasy kit (Qiagen)

6.2.19 Statistical analyses

GraphPad Prism 8 software was used for statistical comparison of live cell imaging, immunoblot densitometry, qPCR, and BMP measurement. Student's t-test was used to assess significant differences between groups. Statistical analysis for lipidomic data was performed using RStudio. Groups were compared using student's t-test followed by adjustment for multiple comparisons using Benjamini–Hochberg methodology to control false discovery rate (FDR). Q-values were determined using the R package ''qvalue,'' and a significance threshold of 0.05 was used.

References

Abeliovich, A., and A.D. Gitler. 2016. Defects in trafficking bridge Parkinson's disease pathology and genetics. *Nature*. 539:207-216.

Abu-Remaileh, M., G.A. Wyant, C. Kim, N.N. Laqtom, M. Abbasi, S.H. Chan, E. Freinkman, and D.M. Sabatini. 2017. Lysosomal metabolomics reveals V-ATPase- and mTOR-dependent regulation of amino acid efflux from lysosomes. *Science*. 358:807-813.

Aharon-Peretz, J., H. Rosenbaum, and R. Gershoni-Baruch. 2004. Mutations in the glucocerebrosidase gene and Parkinson's disease in Ashkenazi Jews. *N Engl J Med*. 351:1972-1977.

AhYoung, A.P., J. Jiang, J. Zhang, X. Khoi Dang, J.A. Loo, Z.H. Zhou, and P.F. Egea. 2015. Conserved SMP domains of the ERMES complex bind phospholipids and mediate tether assembly. *Proc Natl Acad Sci U S A*. 112:E3179-3188.

Alcalay, R.N., F. Hsieh, E. Tengstrand, S. Padmanabhan, M. Baptista, C. Kehoe, S. Narayan, A.K. Boehme, and K. Merchant. 2020. Higher Urine bis(Monoacylglycerol)Phosphate Levels in LRRK2 G2019S Mutation Carriers: Implications for Therapeutic Development. *Mov Disord*. 35:134-141.

Alesutan, I., J. Seifert, T. Pakladok, J. Rheinlaender, A. Lebedeva, S.T. Towhid, C. Stournaras, J. Voelkl, T.E. Schaffer, and F. Lang. 2013. Chorein sensitivity of actin polymerization, cell shape and mechanical stiffness of vascular endothelial cells. *Cell Physiol Biochem*. 32:728-742.

Amick, J., A. Roczniak-Ferguson, and S.M. Ferguson. 2016. C9orf72 binds SMCR8, localizes to lysosomes, and regulates mTORC1 signaling. *Mol Biol Cell*. 27:3040-3051.

Anding, A.L., C. Wang, T.K. Chang, D.A. Sliter, C.M. Powers, K. Hofmann, R.J. Youle, and E.H. Baehrecke. 2018. Vps13D Encodes a Ubiquitin-Binding Protein that Is Required for the Regulation of Mitochondrial Size and Clearance. *Curr Biol*. 28:287-295 e286.

Aoun, M., P.A. Corsetto, G. Nugue, G. Montorfano, E. Ciusani, D. Crouzier, P. Hogarth, A. Gregory, S. Hayflick, G. Zorzi, A.M. Rizzo, and V. Tiranti. 2017. Changes in Red Blood Cell membrane lipid composition: A new perspective into the pathogenesis of PKAN. *Mol Genet Metab*. 121:180-189.

Baldwin, H.A., C. Wang, G. Kanfer, H.V. Shah, A. Velayos-Baeza, M. Dulovic-Mahlow, N. Bruggemann, A. Anding, E.H. Baehrecke, D. Maric, W.A. Prinz, and R.J. Youle. 2021. VPS13D promotes peroxisome biogenesis. *J Cell Biol*. 220.

Bankaitis, V.A., L.M. Johnson, and S.D. Emr. 1986. Isolation of yeast mutants defective in protein targeting to the vacuole. *Proc Natl Acad Sci U S A*. 83:9075-9079.

Bargiela, D., P. Shanmugarajah, C. Lo, E.L. Blakely, R.W. Taylor, R. Horvath, S. Wharton, P.F. Chinnery, and M. Hadjivassiliou. 2015. Mitochondrial pathology in progressive cerebellar ataxia. *Cerebellum Ataxias*. 2:16.

Bean, B.D.M., S.K. Dziurdzik, K.L. Kolehmainen, C.M.S. Fowler, W.K. Kwong, L.I. Grad, M. Davey, C. Schluter, and E. Conibear. 2018. Competitive organelle-specific adaptors recruit Vps13 to membrane contact sites. *J Cell Biol*. 217:3593-3607.

Bender, A., K.J. Krishnan, C.M. Morris, G.A. Taylor, A.K. Reeve, R.H. Perry, E. Jaros, J.S. Hersheson, J. Betts, T. Klopstock, R.W. Taylor, and D.M. Turnbull. 2006. High levels of mitochondrial DNA deletions in substantia nigra neurons in aging and Parkinson disease. *Nat Genet*. 38:515-517.

Bian, X., Y. Saheki, and P. De Camilli. 2018. Ca(2+) releases E-Syt1 autoinhibition to couple ER-plasma membrane tethering with lipid transport. *EMBO J*. 37:219-234.

Bird, T.D., S. Cederbaum, R.W. Valey, and W.L. Stahl. 1978. Familial degeneration of the basal ganglia with acanthocytosis: a clinical, neuropathological, and neurochemical study. *Ann Neurol*. 3:253-258.

Blauwendraat, C., M.A. Nalls, and A.B. Singleton. 2020. The genetic architecture of Parkinson's disease. *Lancet Neurol*. 19:170-178.

Blomen, V.A., P. Majek, L.T. Jae, J.W. Bigenzahn, J. Nieuwenhuis, J. Staring, R. Sacco, F.R. van Diemen, N. Olk, A. Stukalov, C. Marceau, H. Janssen, J.E. Carette, K.L. Bennett, J. Colinge, G. Superti-Furga, and T.R. Brummelkamp. 2015. Gene essentiality and synthetic lethality in haploid human cells. *Science*. 350:1092-1096.

Bonekamp, N.A., and N.G. Larsson. 2018. SnapShot: Mitochondrial Nucleoid. *Cell*. 172:388-388 e381.

Bonet-Ponce, L., A. Beilina, C.D. Williamson, E. Lindberg, J.H. Kluss, S. Saez-Atienzar, N. Landeck, R. Kumaran, A. Mamais, C.K.E. Bleck, Y. Li, and M.R. Cookson. 2020. LRRK2 mediates tubulation and vesicle sorting from lysosomes. *Sci Adv*. 6.

Brekk, O.R., J.R. Honey, S. Lee, P.J. Hallett, and O. Isacson. 2020. Cell type-specific lipid storage changes in Parkinson's disease patient brains are recapitulated by experimental glycolipid disturbance. *Proc Natl Acad Sci U S A*. 117:27646-27654.

Brickner, J.H., and R.S. Fuller. 1997. SOI1 encodes a novel, conserved protein that promotes TGN-endosomal cycling of Kex2p and other membrane proteins by modulating the function of two TGN localization signals. *J Cell Biol*. 139:23-36.

Bultron, G., K. Kacena, D. Pearson, M. Boxer, R. Yang, S. Sathe, G. Pastores, and P.K. Mistry. 2010. The risk of Parkinson's disease in type 1 Gaucher disease. *J Inherit Metab Dis*. 33:167-173.

Calzada, E., O. Onguka, and S.M. Claypool. 2016. Phosphatidylethanolamine Metabolism in Health and Disease. *Int Rev Cell Mol Biol*. 321:29-88.

Campbell, C.L., and P.E. Thorsness. 1998. Escape of mitochondrial DNA to the nucleus in yme1 yeast is mediated by vacuolar-dependent turnover of abnormal mitochondrial compartments. *J Cell Sci*. 111 (Pt 16):2455-2464.

Cohen, M.M., Jr., B.D. Hall, D.W. Smith, C.B. Graham, and K.J. Lampert. 1973. A new syndrome with hypotonia, obesity, mental deficiency, and facial, oral, ocular, and limb anomalies. *J Pediatr*. 83:280-284.

Cook, D.A., G.T. Kannarkat, A.F. Cintron, L.M. Butkovich, K.B. Fraser, J. Chang, N. Grigoryan, S.A. Factor, A.B. West, J.M. Boss, and M.G. Tansey. 2017. LRRK2 levels in immune cells are increased in Parkinson’s disease. *npj Parkinson's Disease*. 3:11.

Da Costa, R., M. Bordessoules, M. Guilleman, V. Carmignac, V. Lhussiez, H. Courot, A. Bataille, A. Chlemaire, C. Bruno, P. Fauque, C. Thauvin, L. Faivre, and L. Duplomb. 2020. Vps13b is required for acrosome biogenesis through functions in Golgi dynamic and membrane trafficking. *Cell Mol Life Sci*. 77:511-529.

Darvish, H., P. Bravo, A. Tafakhori, L.J. Azcona, S. Ranji-Burachaloo, A.H. Johari, and C. Paisan-Ruiz. 2018. Identification of a large homozygous VPS13C deletion in a patient with early-onset Parkinsonism. *Mov Disord*. 33:1968-1970.

De, M., A.N. Oleskie, M. Ayyash, S. Dutta, L. Mancour, M.E. Abazeed, E.J. Brace, G. Skiniotis, and R.S. Fuller. 2017. The Vps13p-Cdc31p complex is directly required for TGN late endosome transport and TGN homotypic fusion. *J Cell Biol*. 216:425-439.

Dean, J.M., and I.J. Lodhi. 2018. Structural and functional roles of ether lipids. *Protein Cell*. 9:196-206.

Demirsoy, S., S. Martin, S. Motamedi, S. van Veen, T. Holemans, C. Van den Haute, A. Jordanova, V. Baekelandt, P. Vangheluwe, and P. Agostinis. 2017. ATP13A2/PARK9 regulates endo-/lysosomal cargo sorting and proteostasis through a novel PI(3, 5)P2-mediated scaffolding function. *Hum Mol Genet*. 26:1656-1669.

Dhekne, H.S., I. Yanatori, R.C. Gomez, F. Tonelli, F. Diez, B. Schule, M. Steger, D.R. Alessi, and S.R. Pfeffer. 2018. A pathway for Parkinson's Disease LRRK2 kinase to block primary cilia and Sonic hedgehog signaling in the brain. *Elife*. 7.

Dimmer, K.S., and D. Rapaport. 2017. Mitochondrial contact sites as platforms for phospholipid exchange. *Biochim Biophys Acta Mol Cell Biol Lipids*. 1862:69-80.

Dolle, C., I. Flones, G.S. Nido, H. Miletic, N. Osuagwu, S. Kristoffersen, P.K. Lilleng, J.P. Larsen, O.B. Tysnes, K. Haugarvoll, L.A. Bindoff, and C. Tzoulis. 2016. Defective mitochondrial DNA homeostasis in the substantia nigra in Parkinson disease. *Nat Commun*. 7:13548.

Dong, R., Y. Saheki, S. Swarup, L. Lucast, J.W. Harper, and P. De Camilli. 2016. Endosome-ER Contacts Control Actin Nucleation and Retromer Function through VAP-Dependent Regulation of PI4P. *Cell*. 166:408-423.

Drin, G., J.F. Casella, R. Gautier, T. Boehmer, T.U. Schwartz, and B. Antonny. 2007. A general amphipathic alpha-helical motif for sensing membrane curvature. *Nat Struct Mol Biol*. 14:138-146.

Du, Y., J. Xiong, and W. Ji. 2020. Trans-Golgi network-lipid droplet contacts maintain the TGN integrity and function via lipid transfer activities of VPS13B. *bioRxiv*.

Duplomb, L., S. Duvet, D. Picot, G. Jego, S. El Chehadeh-Djebbar, N. Marle, N. Gigot, B. Aral, V. Carmignac, J. Thevenon, E. Lopez, J.B. Riviere, A. Klein, C. Philippe, N. Droin, E. Blair, F. Girodon, J. Donadieu, C. Bellanne-Chantelot, L. Delva, J.C. Michalski, E. Solary, L. Faivre, F. Foulquier, and C. Thauvin-Robinet. 2014. Cohen syndrome is associated with major glycosylation defects. *Hum Mol Genet*. 23:2391-2399.

Dziurdzik, S.K., B.D.M. Bean, M. Davey, and E. Conibear. 2020. A VPS13D spastic ataxia mutation disrupts the conserved adaptor-binding site in yeast Vps13. *Hum Mol Genet*. 29:635-648.

Eguchi, T., T. Kuwahara, M. Sakurai, T. Komori, T. Fujimoto, G. Ito, S.I. Yoshimura, A. Harada, M. Fukuda, M. Koike, and T. Iwatsubo. 2018. LRRK2 and its substrate Rab GTPases are sequentially targeted onto stressed lysosomes and maintain their homeostasis. *Proc Natl Acad Sci U S A*. 115:E9115-E9124.

Elbaz-Alon, Y., Y. Guo, N. Segev, M. Harel, D.E. Quinnell, T. Geiger, O. Avinoam, D. Li, and J. Nunnari. 2020. PDZD8 interacts with Protrudin and Rab7 at ER-late endosome membrane contact sites associated with mitochondria. *Nat Commun*. 11:3645.

Elbaz-Alon, Y., E. Rosenfeld-Gur, V. Shinder, A.H. Futerman, T. Geiger, and M. Schuldiner. 2014. A dynamic interface between vacuoles and mitochondria in yeast. *Dev Cell*. 30:95-102.

Fanning, S., D. Selkoe, and U. Dettmer. 2020. Parkinson's disease: proteinopathy or lipidopathy? *NPJ Parkinsons Dis*. 6:3.

Ferguson, S.M. 2015. Beyond indigestion: emerging roles for lysosome-based signaling in human disease. *Curr Opin Cell Biol*. 35:59-68.

Fernandopulle, M.S., R. Prestil, C. Grunseich, C. Wang, L. Gan, and M.E. Ward. 2018. Transcription Factor-Mediated Differentiation of Human iPSCs into Neurons. *Curr Protoc Cell Biol*. 79:e51.

Fidler, D.R., S.E. Murphy, K. Courtis, P. Antonoudiou, R. El-Tohamy, J. Ient, and T.P. Levine. 2016. Using HHsearch to tackle proteins of unknown function: A pilot study with PH domains. *Traffic*. 17:1214-1226.

Fischer, T.D., C. Wang, B.S. Padman, M. Lazarou, and R.J. Youle. 2020. STING induces LC3B lipidation onto single-membrane vesicles via the V-ATPase and ATG16L1-WD40 domain. *J Cell Biol*. 219.

Foller, M., A. Hermann, S. Gu, I. Alesutan, S.M. Qadri, O. Borst, E.M. Schmidt, F. Schiele, J.M. vom Hagen, C. Saft, L. Schols, H. Lerche, C. Stournaras, A. Storch, and F. Lang. 2012. Chorein-sensitive polymerization of cortical actin and suicidal cell death in chorea-acanthocytosis. *FASEB J*. 26:1526-1534.

Galmes, R., A. Houcine, A.R. van Vliet, P. Agostinis, C.L. Jackson, and F. Giordano. 2016. ORP5/ORP8 localize to endoplasmic reticulum-mitochondria contacts and are involved in mitochondrial function. *EMBO Rep*. 17:800-810.

Ganga, A.K., M.C. Kennedy, M.E. Oguchi, S. Gray, K.E. Oliver, T.A. Knight, E.M. De La Cruz, Y. Homma, M. Fukuda, and D.K. Breslow. 2021. Rab34 GTPase mediates ciliary membrane formation in the intracellular ciliogenesis pathway. *Curr Biol*. 31:2895-2905 e2897.

Gao, Y., J. Xiong, Q.Z. Chu, and W.K. Ji. 2022. PDZD8-mediated lipid transfer at contacts between the ER and late endosomes/lysosomes is required for neurite outgrowth. *J Cell Sci*. 135.

Gatta, A.T., and T.P. Levine. 2017. Piecing Together the Patchwork of Contact Sites. *Trends Cell Biol*. 27:214-229.

Gauthier, J., I.A. Meijer, D. Lessel, N.E. Mencacci, D. Krainc, M. Hempel, K. Tsiakas, H. Prokisch, E. Rossignol, M.H. Helm, L.H. Rodan, J. Karamchandani, M. Carecchio, S.J. Lubbe, A. Telegrafi, L.B. Henderson, K. Lorenzo, S.E. Wallace, I.A. Glass, F.F. Hamdan, J.L. Michaud, G.A. Rouleau, and P.M. Campeau. 2018. Recessive mutations in >VPS13D cause childhood onset movement disorders. *Ann Neurol*. 83:1089-1095.

Gautier, R., D. Douguet, B. Antonny, and G. Drin. 2008. HELIQUEST: a web server to screen sequences with specific alpha-helical properties. *Bioinformatics*. 24:2101-2102.

Ghanbarpour, A., D.P. Valverde, T.J. Melia, and K.M. Reinisch. 2021. A model for a partnership of lipid transfer proteins and scramblases in membrane expansion and organelle biogenesis. *Proc Natl Acad Sci U S A*. 118.

Gillingham, A.K., J. Bertram, F. Begum, and S. Munro. 2019. In vivo identification of GTPase interactors by mitochondrial relocalization and proximity biotinylation. *Elife*. 8.

Gillingham, A.K., R. Sinka, I.L. Torres, K.S. Lilley, and S. Munro. 2014. Toward a comprehensive map of the effectors of rab GTPases. *Dev Cell*. 31:358-373.

Gkirtzimanaki, K., E. Kabrani, D. Nikoleri, A. Polyzos, A. Blanas, P. Sidiropoulos, A. Makrigiannakis, G. Bertsias, D.T. Boumpas, and P. Verginis. 2018. IFNalpha Impairs Autophagic Degradation of mtDNA Promoting Autoreactivity of SLE Monocytes in a STING-Dependent Fashion. *Cell Rep*. 25:921-933 e925.

Go, C.D., J.D.R. Knight, A. Rajasekharan, B. Rathod, G.G. Hesketh, K.T. Abe, J.-Y. Youn, P. Samavarchi-Tehrani, H. Zhang, L.Y. Zhu, E. Popiel, J.-P. Lambert, É. Coyaud, S.W.T. Cheung, D. Rajendran, C.J. Wong, H. Antonicka, L. Pelletier, A.F. Palazzo, E.A. Shoubridge, B. Raught, and A.-C. Gingras. 2021. A proximity-dependent biotinylation map of a human cell: an interactive web resource. *bioRxiv*:796391.

Gonugunta, V.K., T. Sakai, V. Pokatayev, K. Yang, J. Wu, N. Dobbs, and N. Yan. 2017. Trafficking-Mediated STING Degradation Requires Sorting to Acidified Endolysosomes and Can Be Targeted to Enhance Anti-tumor Response. *Cell Rep*. 21:3234-3242.

Grippa, A., L. Buxo, G. Mora, C. Funaya, F.Z. Idrissi, F. Mancuso, R. Gomez, J. Muntanya, E. Sabido, and P. Carvalho. 2015. The seipin complex Fld1/Ldb16 stabilizes ER-lipid droplet contact sites. *J Cell Biol*. 211:829-844.

Gruenberg, J. 2020. Life in the lumen: The multivesicular endosome. *Traffic*. 21:76-93.

Gui, X., H. Yang, T. Li, X. Tan, P. Shi, M. Li, F. Du, and Z.J. Chen. 2019. Autophagy induction via STING trafficking is a primordial function of the cGAS pathway. *Nature*. 567:262-266.

Guillen-Samander, A., X. Bian, and P. De Camilli. 2019. PDZD8 mediates a Rab7-dependent interaction of the ER with late endosomes and lysosomes. *Proc Natl Acad Sci U S A*. 116:22619-22623.

Guillen-Samander, A., M. Leonzino, M.G. Hanna, N. Tang, H. Shen, and P. De Camilli. 2021. VPS13D bridges the ER to mitochondria and peroxisomes via Miro. *J Cell Biol*. 220.

Guo, M., A. Hartlova, B.D. Dill, A.R. Prescott, M. Gierlinski, and M. Trost. 2015. High-resolution quantitative proteome analysis reveals substantial differences between phagosomes of RAW 264.7 and bone marrow derived macrophages. *Proteomics*. 15:3169-3174.

Hanekamp, T., M.K. Thorsness, I. Rebbapragada, E.M. Fisher, C. Seebart, M.R. Darland, J.A. Coxbill, D.L. Updike, and P.E. Thorsness. 2002. Maintenance of mitochondrial morphology is linked to maintenance of the mitochondrial genome in Saccharomyces cerevisiae. *Genetics*. 162:1147-1156.

Hang, L., J. Thundyil, and K.L. Lim. 2015. Mitochondrial dysfunction and Parkinson disease: a Parkin-AMPK alliance in neuroprotection. *Ann N Y Acad Sci*. 1350:37-47.

Hendrickson, W.A. 1991. Determination of macromolecular structures from anomalous diffraction of synchrotron radiation. *Science*. 254:51-58.

Henry, A.G., S. Aghamohammadzadeh, H. Samaroo, Y. Chen, K. Mou, E. Needle, and W.D. Hirst. 2015. Pathogenic LRRK2 mutations, through increased kinase activity, produce enlarged lysosomes with reduced degradative capacity and increase ATP13A2 expression. *Hum Mol Genet*. 24:6013-6028.

Hickman, S., S. Izzy, P. Sen, L. Morsett, and J. El Khoury. 2018. Microglia in neurodegeneration. *Nat Neurosci*. 21:1359-1369.

Hirabayashi, Y., S.K. Kwon, H. Paek, W.M. Pernice, M.A. Paul, J. Lee, P. Erfani, A. Raczkowski, D.S. Petrey, L.A. Pon, and F. Polleux. 2017. ER-mitochondria tethering by PDZD8 regulates Ca(2+) dynamics in mammalian neurons. *Science*. 358:623-630.

Hobert, J.A., and G. Dawson. 2007. A novel role of the Batten disease gene CLN3: association with BMP synthesis. *Biochem Biophys Res Commun*. 358:111-116.

Holemans, T., D.M. Sorensen, S. van Veen, S. Martin, D. Hermans, G.C. Kemmer, C. Van den Haute, V. Baekelandt, T. Gunther Pomorski, P. Agostinis, F. Wuytack, M. Palmgren, J. Eggermont, and P. Vangheluwe. 2015. A lipid switch unlocks Parkinson's disease-associated ATP13A2. *Proc Natl Acad Sci U S A*. 112:9040-9045.

Holmes, S.E., E. O'Hearn, A. Rosenblatt, C. Callahan, H.S. Hwang, R.G. Ingersoll-Ashworth, A. Fleisher, G. Stevanin, A. Brice, N.T. Potter, C.A. Ross, and R.L. Margolis. 2001. A repeat expansion in the gene encoding junctophilin-3 is associated with Huntington disease-like 2. *Nat Genet*. 29:377-378.

Holthuis, J.C., and A.K. Menon. 2014. Lipid landscapes and pipelines in membrane homeostasis. *Nature*. 510:48-57.

Honisch, S., S. Gu, J.M. Vom Hagen, S. Alkahtani, A.A. Al Kahtane, A. Tsapara, A. Hermann, A. Storch, L. Schols, F. Lang, and C. Stournaras. 2015. Chorein Sensitive Arrangement of Cytoskeletal Architecture. *Cell Physiol Biochem*. 37:399-408.

Honscher, C., M. Mari, K. Auffarth, M. Bohnert, J. Griffith, W. Geerts, M. van der Laan, M. Cabrera, F. Reggiori, and C. Ungermann. 2014. Cellular metabolism regulates contact sites between vacuoles and mitochondria. *Dev Cell*. 30:86-94.

Hsu, T.H., R.H. Chen, Y.H. Cheng, and C.W. Wang. 2017. Lipid droplets are central organelles for meiosis II progression during yeast sporulation. *Mol Biol Cell*. 28:440-451.

Hughes, C.E., T.K. Coody, M.Y. Jeong, J.A. Berg, D.R. Winge, and A.L. Hughes. 2020. Cysteine Toxicity Drives Age-Related Mitochondrial Decline by Altering Iron Homeostasis. *Cell*. 180:296-310 e218.

Huttlin, E.L., R.J. Bruckner, J.A. Paulo, J.R. Cannon, L. Ting, K. Baltier, G. Colby, F. Gebreab, M.P. Gygi, H. Parzen, J. Szpyt, S. Tam, G. Zarraga, L. Pontano-Vaites, S. Swarup, A.E. White, D.K. Schweppe, R. Rad, B.K. Erickson, R.A. Obar, K.G. Guruharsha, K. Li, S. Artavanis-Tsakonas, S.P. Gygi, and J.W. Harper. 2017. Architecture of the human interactome defines protein communities and disease networks. *Nature*. 545:505-509.

Insolera, R., P. Lorincz, A.J. Wishnie, G. Juhasz, and C.A. Collins. 2021. Mitochondrial fission, integrity and completion of mitophagy require separable functions of Vps13D in Drosophila neurons. *PLoS Genet*. 17:e1009731.

Ishibashi, Y., A. Kohyama-Koganeya, and Y. Hirabayashi. 2013. New insights on glucosylated lipids: metabolism and functions. *Biochim Biophys Acta*. 1831:1475-1485.

Jeong, H., J. Park, and C. Lee. 2016. Crystal structure of Mdm12 reveals the architecture and dynamic organization of the ERMES complex. *EMBO Rep*. 17:1857-1871.

Jimenez-Rojo, N., and H. Riezman. 2019. On the road to unraveling the molecular functions of ether lipids. *FEBS Lett*. 593:2378-2389.

John Peter, A.T., B. Herrmann, D. Antunes, D. Rapaport, K.S. Dimmer, and B. Kornmann. 2017. Vps13-Mcp1 interact at vacuole-mitochondria interfaces and bypass ER-mitochondria contact sites. *J Cell Biol*. 216:3219-3229.

Kalia, L.V., and A.E. Lang. 2015. Parkinson's disease. *Lancet*. 386:896-912.

Kalluri, R., and V.S. LeBleu. 2020. The biology, function, and biomedical applications of exosomes. *Science*. 367.

Khozhukhar, N., D. Spadafora, Y. Rodriguez, and M. Alexeyev. 2018. Elimination of Mitochondrial DNA from Mammalian Cells. *Curr Protoc Cell Biol*. 78:20 11 21-20 11 14.

Kim, M.J., R.U. Lee, J. Oh, J.E. Choi, H. Kim, K. Lee, S.K. Hwang, J.H. Lee, J.A. Lee, B.K. Kaang, C.S. Lim, and Y.S. Lee. 2019. Spatial Learning and Motor Deficits in Vacuolar Protein Sorting-associated Protein 13b (Vps13b) Mutant Mouse. *Exp Neurobiol*. 28:485-494.

Kim, S., Y.C. Wong, F. Gao, and D. Krainc. 2021. Dysregulation of mitochondria-lysosome contacts by GBA1 dysfunction in dopaminergic neuronal models of Parkinson's disease. *Nat Commun*. 12:1807.

Knorr, R.L., R. Dimova, and R. Lipowsky. 2012. Curvature of double-membrane organelles generated by changes in membrane size and composition. *PLoS One*. 7:e32753.

Kolehmainen, J., G.C. Black, A. Saarinen, K. Chandler, J. Clayton-Smith, A.L. Traskelin, R. Perveen, S. Kivitie-Kallio, R. Norio, M. Warburg, J.P. Fryns, A. de la Chapelle, and A.E. Lehesjoki. 2003. Cohen syndrome is caused by mutations in a novel gene, COH1, encoding a transmembrane protein with a presumed role in vesicle-mediated sorting and intracellular protein transport. *Am J Hum Genet*. 72:1359-1369.

Kornmann, B., E. Currie, S.R. Collins, M. Schuldiner, J. Nunnari, J.S. Weissman, and P. Walter. 2009. An ER-mitochondria tethering complex revealed by a synthetic biology screen. *Science*. 325:477-481.

Kraytsberg, Y., E. Kudryavtseva, A.C. McKee, C. Geula, N.W. Kowall, and K. Khrapko. 2006. Mitochondrial DNA deletions are abundant and cause functional impairment in aged human substantia nigra neurons. *Nat Genet*. 38:518-520.

Kumar, N., M. Leonzino, W. Hancock-Cerutti, F.A. Horenkamp, P. Li, J.A. Lees, H. Wheeler, K.M. Reinisch, and P. De Camilli. 2018. VPS13A and VPS13C are lipid transport proteins differentially localized at ER contact sites. *J Cell Biol*. 217:3625-3639.

Lahiri, S., A. Toulmay, and W.A. Prinz. 2015. Membrane contact sites, gateways for lipid homeostasis. *Curr Opin Cell Biol*. 33:82-87.

Lang, A.B., A.T. John Peter, P. Walter, and B. Kornmann. 2015. ER-mitochondrial junctions can be bypassed by dominant mutations in the endosomal protein Vps13. *J Cell Biol*. 210:883-890.

Lazarou, M., D.A. Sliter, L.A. Kane, S.A. Sarraf, C. Wang, J.L. Burman, D.P. Sideris, A.I. Fogel, and R.J. Youle. 2015. The ubiquitin kinase PINK1 recruits autophagy receptors to induce mitophagy. *Nature*. 524:309-314.

Lees, J.A., M. Messa, E.W. Sun, H. Wheeler, F. Torta, M.R. Wenk, P. De Camilli, and K.M. Reinisch. 2017. Lipid transport by TMEM24 at ER-plasma membrane contacts regulates pulsatile insulin secretion. *Science*. 355.

Leonzino, M., K.M. Reinisch, and P. De Camilli. 2021. Insights into VPS13 properties and function reveal a new mechanism of eukaryotic lipid transport. *BBA - Molecular and Cell Biology of Lipids*.

Lesage, S., V. Drouet, E. Majounie, V. Deramecourt, M. Jacoupy, A. Nicolas, F. Cormier-Dequaire, S.M. Hassoun, C. Pujol, S. Ciura, Z. Erpapazoglou, T. Usenko, C.A. Maurage, M. Sahbatou, S. Liebau, J. Ding, B. Bilgic, M. Emre, N. Erginel-Unaltuna, G. Guven, F. Tison, C. Tranchant, M. Vidailhet, J.C. Corvol, P. Krack, A.L. Leutenegger, M.A. Nalls, D.G. Hernandez, P. Heutink, J.R. Gibbs, J. Hardy, N.W. Wood, T. Gasser, A. Durr, J.F. Deleuze, M. Tazir, A. Destee, E. Lohmann, E. Kabashi, A. Singleton, O. Corti, A. Brice, S. French

Parkinson's Disease Genetics, and C. International Parkinson's Disease Genomics. 2016. Loss of VPS13C Function in Autosomal-Recessive Parkinsonism Causes Mitochondrial Dysfunction and Increases PINK1/Parkin-Dependent Mitophagy. *Am J Hum Genet*. 98:500-513.

Levine, T., and C. Loewen. 2006. Inter-organelle membrane contact sites: through a glass, darkly. *Curr Opin Cell Biol*. 18:371-378.

Lewandowski, N.M., S. Ju, M. Verbitsky, B. Ross, M.L. Geddie, E. Rockenstein, A. Adame, A. Muhammad, J.P. Vonsattel, D. Ringe, L. Cote, S. Lindquist, E. Masliah, G.A. Petsko, K. Marder, L.N. Clark, and S.A. Small. 2010. Polyamine pathway contributes to the pathogenesis of Parkinson disease. *Proc Natl Acad Sci U S A*. 107:16970-16975.

Li, P., J.A. Lees, C.P. Lusk, and K.M. Reinisch. 2020. Cryo-EM reconstruction of a VPS13 fragment reveals a long groove to channel lipids between membranes. *J Cell Biol*. 219.

Li, X., F. Lu, M.N. Trinh, P. Schmiege, J. Seemann, J. Wang, and G. Blobel. 2017. 3.3 A structure of Niemann-Pick C1 protein reveals insights into the function of the C-terminal luminal domain in cholesterol transport. *Proc Natl Acad Sci U S A*. 114:9116-9121.

Lin, M.K., and M.J. Farrer. 2014. Genetics and genomics of Parkinson's disease. *Genome Med*. 6:48.

Lin, R., C. Heylbroeck, P.M. Pitha, and J. Hiscott. 1998. Virus-dependent phosphorylation of the IRF-3 transcription factor regulates nuclear translocation, transactivation potential, and proteasome-mediated degradation. *Mol Cell Biol*. 18:2986-2996.

Liu, L., K. Zhang, H. Sandoval, S. Yamamoto, M. Jaiswal, E. Sanz, Z. Li, J. Hui, B.H. Graham, A. Quintana, and H.J. Bellen. 2015a. Glial lipid droplets and ROS induced by mitochondrial defects promote neurodegeneration. *Cell*. 160:177-190.

Liu, N., E.A. Tengstrand, L. Chourb, and F.Y. Hsieh. 2014. Di-22:6-bis(monoacylglycerol)phosphate: A clinical biomarker of drug-induced phospholipidosis for drug development and safety assessment. *Toxicol Appl Pharmacol*. 279:467-476.

Liu, S., X. Cai, J. Wu, Q. Cong, X. Chen, T. Li, F. Du, J. Ren, Y.T. Wu, N.V. Grishin, and Z.J. Chen. 2015b. Phosphorylation of innate immune adaptor proteins MAVS, STING, and TRIF induces IRF3 activation. *Science*. 347:aaa2630.

Liu, X., K. Salokas, F. Tamene, Y. Jiu, R.G. Weldatsadik, T. Ohman, and M. Varjosalo. 2018. An AP-MS- and BioID-compatible MAC-tag enables comprehensive mapping of protein interactions and subcellular localizations. *Nat Commun*. 9:1188.

Logan, T., S. DeVos, M.J. Simon, S. Davis, J. Wang, R. Low, F. Huang, Y. Rajendra, R. Prorok, E. Sun, A. Rana, J. Hsiao-Nakamoto, S. Mosesova, Y. Zhu, G.M. Cherf, B. Lengerich, A. Bhalla, D.J. Kim, D. Chan, J. Duque, H. Tran, M. Lenser, H. Nguyen, R. Chau, T. Earr, M.S. Kariolis, K.M. Monroe, P.E. Sanchez, M.S. Dennis, K.R. Henne, K. Gunasekaran, G. Astarita, R.J. Watts, Z.K. Sweeney, J.W. Lewcock, A. Srivastava, and G. Di Paolo. 2020. A brain penetrant progranulin biotherapeutic rescues lysosomal and inflammatory phenotypes in the brain of GRN knockout mice. *Alzheimer's & Dementia*. 16:e040602.

Lupo, F., E. Tibaldi, A. Matte, A.K. Sharma, A.M. Brunati, S.L. Alper, C. Zancanaro, D. Benati, A. Siciliano, M. Bertoldi, F. Zonta, A. Storch, R.H. Walker, A. Danek, B. Bader, A. Hermann, and L. De Franceschi. 2016. A new molecular link between defective autophagy and erythroid abnormalities in chorea-acanthocytosis. *Blood*. 128:2976-2987.

Maeda, S., C. Otomo, and T. Otomo. 2019. The autophagic membrane tether ATG2A transfers lipids between membranes. *Elife*. 8.

Maeda, S., H. Yamamoto, L.N. Kinch, C.M. Garza, S. Takahashi, C. Otomo, N.V. Grishin, S. Forli, N. Mizushima, and T. Otomo. 2020. Structure, lipid scrambling activity and role in autophagosome formation of ATG9A. *Nat Struct Mol Biol*. 27:1194-1201.

Malpartida, A.B., M. Williamson, D.P. Narendra, R. Wade-Martins, and B.J. Ryan. 2021. Mitochondrial Dysfunction and Mitophagy in Parkinson's Disease: From Mechanism to Therapy. *Trends Biochem Sci*. 46:329-343.

Manyam, B.V., T.N. Ferraro, and T.A. Hare. 1988. Cerebrospinal fluid amino compounds in Parkinson's disease. Alterations due to carbidopa/levodopa. *Arch Neurol*. 45:48-50.

Martin-Jimenez, R., O. Lurette, and E. Hebert-Chatelain. 2020. Damage in Mitochondrial DNA Associated with Parkinson's Disease. *DNA Cell Biol*. 39:1421-1430.

Matoba, K., T. Kotani, A. Tsutsumi, T. Tsuji, T. Mori, D. Noshiro, Y. Sugita, N. Nomura, S. Iwata, Y. Ohsumi, T. Fujimoto, H. Nakatogawa, M. Kikkawa, and N.N. Noda. 2020. Atg9 is a lipid scramblase that mediates autophagosomal membrane expansion. *Nat Struct Mol Biol*. 27:1185-1193.

Matsui, H., F. Sato, S. Sato, M. Koike, Y. Taruno, S. Saiki, M. Funayama, H. Ito, Y. Taniguchi, N. Uemura, A. Toyoda, Y. Sakaki, S. Takeda, Y. Uchiyama, N. Hattori, and R. Takahashi. 2013. ATP13A2 deficiency induces a decrease in cathepsin D activity, fingerprint-like inclusion body formation, and selective degeneration of dopaminergic neurons. *FEBS Lett*. 587:1316-1325.

Matsuo, H., J. Chevallier, N. Mayran, I. Le Blanc, C. Ferguson, J. Faure, N.S. Blanc, S. Matile, J. Dubochet, R. Sadoul, R.G. Parton, F. Vilbois, and J. Gruenberg. 2004. Role of LBPA and Alix in multivesicular liposome formation and endosome organization. *Science*. 303:531-534.

Mazzulli, J.R., Y.H. Xu, Y. Sun, A.L. Knight, P.J. McLean, G.A. Caldwell, E. Sidransky, G.A. Grabowski, and D. Krainc. 2011. Gaucher disease glucocerebrosidase and alpha-synuclein form a bidirectional pathogenic loop in synucleinopathies. *Cell*. 146:37-52.

McCauley, M.E., J.G. O'Rourke, A. Yanez, J.L. Markman, R. Ho, X. Wang, S. Chen, D. Lall, M. Jin, A. Muhammad, S. Bell, J. Landeros, V. Valencia, M. Harms, M. Arditi, C. Jefferies, and R.H. Baloh. 2020. C9orf72 in myeloid cells suppresses STING-induced inflammation. *Nature*. 585:96-101.

McCray, B.A., E. Skordalakes, and J.P. Taylor. 2010. Disease mutations in Rab7 result in unregulated nucleotide exchange and inappropriate activation. *Hum Mol Genet*. 19:1033-1047.

McLelland, G.L., S.A. Lee, H.M. McBride, and E.A. Fon. 2016. Syntaxin-17 delivers PINK1/parkin-dependent mitochondrial vesicles to the endolysosomal system. *J Cell Biol*. 214:275-291.

Miranda, A.M., Z.M. Lasiecka, Y. Xu, J. Neufeld, S. Shahriar, S. Simoes, R.B. Chan, T.G. Oliveira, S.A. Small, and G. Di Paolo. 2018. Neuronal lysosomal dysfunction releases exosomes harboring APP C-terminal fragments and unique lipid signatures. *Nat Commun*. 9:291.

Motwani, M., S. Pesiridis, and K.A. Fitzgerald. 2019. DNA sensing by the cGAS-STING pathway in health and disease. *Nat Rev Genet*. 20:657-674.

Munoz-Braceras, S., R. Calvo, and R. Escalante. 2015. TipC and the chorea-acanthocytosis protein VPS13A regulate autophagy in Dictyostelium and human HeLa cells. *Autophagy*. 11:918-927.

Murphy, K.E., A.M. Gysbers, S.K. Abbott, N. Tayebi, W.S. Kim, E. Sidransky, A. Cooper, B. Garner, and G.M. Halliday. 2014. Reduced glucocerebrosidase is associated with increased alpha-synuclein in sporadic Parkinson's disease. *Brain*. 137:834-848.

Murphy, S.E., and T.P. Levine. 2016. VAP, a Versatile Access Point for the Endoplasmic Reticulum: Review and analysis of FFAT-like motifs in the VAPome. *Biochim Biophys Acta*. 1861:952-961.

Nagata, O., M. Nakamura, H. Sakimoto, Y. Urata, N. Sasaki, N. Shiokawa, and A. Sano. 2018. Mouse model of chorea-acanthocytosis exhibits male infertility caused by impaired sperm motility as a result of ultrastructural morphological abnormalities in the mitochondrial sheath in the sperm midpiece. *Biochem Biophys Res Commun*. 503:915-920.

Nalls, M.A., C. Blauwendraat, C.L. Vallerga, K. Heilbron, S. Bandres-Ciga, D. Chang, M. Tan, D.A. Kia, A.J. Noyce, A. Xue, J. Bras, E. Young, R. von Coelln, J. Simon-Sanchez, C. Schulte, M. Sharma, L. Krohn, L. Pihlstrom, A. Siitonen, H. Iwaki, H. Leonard, F. Faghri, J.R. Gibbs, D.G. Hernandez, S.W. Scholz, J.A. Botia, M. Martinez, J.C. Corvol, S. Lesage, J. Jankovic, L.M. Shulman, M. Sutherland, P. Tienari, K. Majamaa, M. Toft, O.A. Andreassen, T. Bangale, A. Brice, J. Yang, Z. Gan-Or, T. Gasser, P. Heutink, J.M. Shulman, N.W. Wood, D.A. Hinds, J.A. Hardy, H.R. Morris, J. Gratten, P.M. Visscher, R.R. Graham, A.B. Singleton, T. andMe Research, C. System Genomics of Parkinson's Disease, and C. International Parkinson's Disease Genomics. 2019. Identification of novel risk loci, causal insights, and heritable risk for Parkinson's disease: a meta-analysis of genome-wide association studies. *Lancet Neurol*. 18:1091-1102.

Nalls, M.A., N. Pankratz, C.M. Lill, C.B. Do, D.G. Hernandez, M. Saad, A.L. DeStefano, E. Kara, J. Bras, M. Sharma, C. Schulte, M.F. Keller, S. Arepalli, C. Letson, C. Edsall, H. Stefansson, X. Liu, H. Pliner, J.H. Lee, R. Cheng, M.A. Ikram, J.P. Ioannidis, G.M. Hadjigeorgiou, J.C. Bis, M. Martinez, J.S. Perlmutter, A. Goate, K. Marder, B. Fiske, M. Sutherland, G. Xiromerisiou, R.H. Myers, L.N. Clark, K. Stefansson, J.A. Hardy, P. Heutink, H. Chen, N.W. Wood, H. Houlden, H. Payami, A. Brice, W.K. Scott, T. Gasser, L. Bertram, N. Eriksson, T. Foroud, and A.B. Singleton. 2014. Large-scale meta-analysis of genome-wide association data identifies six new risk loci for Parkinson's disease. *Nat Genet*. 46:989-993.

Nasser, F., A. Kurtenbach, S. Biskup, S. Weidensee, S. Kohl, and E. Zrenner. 2019. Ophthalmic features of retinitis pigmentosa in Cohen syndrome caused by pathogenic variants in the VPS13B gene. *Acta Ophthalmol*.

Nussbaum, R.L., and C.E. Ellis. 2003. Alzheimer's disease and Parkinson's disease. *N Engl J Med*. 348:1356-1364.

Oka, T., S. Hikoso, O. Yamaguchi, M. Taneike, T. Takeda, T. Tamai, J. Oyabu, T. Murakawa, H. Nakayama, K. Nishida, S. Akira, A. Yamamoto, I. Komuro, and K. Otsu. 2012. Mitochondrial DNA that escapes from autophagy causes inflammation and heart failure. *Nature*. 485:251-255.

Okamoto, S., Y. Amaishi, I. Maki, T. Enoki, and J. Mineno. 2019. Highly efficient genome editing for single-base substitutions using optimized ssODNs with Cas9-RNPs. *Sci Rep*. 9:4811.

Olsen, A.L., and M.B. Feany. 2021. Parkinson's disease risk genes act in glia to control neuronal alpha-synuclein toxicity. *Neurobiol Dis*. 159:105482.

Ordureau, A., S.A. Sarraf, D.M. Duda, J.M. Heo, M.P. Jedrychowski, V.O. Sviderskiy, J.L. Olszewski, J.T. Koerber, T. Xie, S.A. Beausoleil, J.A. Wells, S.P. Gygi, B.A. Schulman, and J.W. Harper. 2014. Quantitative proteomics reveal a feedforward mechanism for mitochondrial PARKIN translocation and ubiquitin chain synthesis. *Mol Cell*. 56:360-375.

Osawa, T., T. Kotani, T. Kawaoka, E. Hirata, K. Suzuki, H. Nakatogawa, Y. Ohsumi, and N.N. Noda. 2019. Atg2 mediates direct lipid transfer between membranes for autophagosome formation. *Nat Struct Mol Biol*. 26:281-288.

Palikaras, K., E. Lionaki, and N. Tavernarakis. 2018. Mechanisms of mitophagy in cellular homeostasis, physiology and pathology. *Nat Cell Biol*. 20:1013-1022.

Park, B.C., Y.I. Yim, X. Zhao, M.B. Olszewski, E. Eisenberg, and L.E. Greene. 2015. The clathrin-binding and J-domains of GAK support the uncoating and chaperoning of clathrin by Hsc70 in the brain. *J Cell Sci*. 128:3811-3821.

Park, J.S., and A.M. Neiman. 2012. VPS13 regulates membrane morphogenesis during sporulation in Saccharomyces cerevisiae. *J Cell Sci*. 125:3004-3011.

Park, J.S., Y. Okumura, H. Tachikawa, and A.M. Neiman. 2013. SPO71 encodes a developmental stage-specific partner for Vps13 in Saccharomyces cerevisiae. *Eukaryot Cell*. 12:1530-1537.

Park, J.S., M.K. Thorsness, R. Policastro, L.L. McGoldrick, N.M. Hollingsworth, P.E. Thorsness, and A.M. Neiman. 2016. Yeast Vps13 promotes mitochondrial function and is localized at membrane contact sites. *Mol Biol Cell*. 27:2435-2449.

Patel, D., and S.N. Witt. 2017. Ethanolamine and Phosphatidylethanolamine: Partners in Health and Disease. *Oxid Med Cell Longev*. 2017:4829180.

Pei, J., B.H. Kim, and N.V. Grishin. 2008. PROMALS3D: a tool for multiple protein sequence and structure alignments. *Nucleic Acids Res*. 36:2295-2300.

Peikert, K., A. Danek, and A. Hermann. 2018. Current state of knowledge in Chorea-Acanthocytosis as core Neuroacanthocytosis syndrome. *Eur J Med Genet*. 61:699-705.

Pelzl, L., B. Elsir, I. Sahu, R. Bissinger, Y. Singh, B. Sukkar, S. Honisch, L. Schoels, M. Jemaa, E. Lang, A. Storch, A. Hermann, C. Stournaras, and F. Lang. 2017. Lithium Sensitivity of Store Operated Ca2+ Entry and Survival of Fibroblasts Isolated from Chorea-Acanthocytosis Patients. *Cell Physiol Biochem*. 42:2066-2077.

Peretti, D., S. Kim, R. Tufi, and S. Lev. 2019. Lipid Transfer Proteins and Membrane Contact Sites in Human Cancer. *Front Cell Dev Biol*. 7:371.

Pfisterer, S.G., D. Bakula, T. Frickey, A. Cezanne, D. Brigger, M.P. Tschan, H. Robenek, and T. Proikas-Cezanne. 2014. Lipid droplet and early autophagosomal membrane targeting of Atg2A and Atg14L in human tumor cells. *J Lipid Res*. 55:1267-1278.

Pickrell, A.M., C.H. Huang, S.R. Kennedy, A. Ordureau, D.P. Sideris, J.G. Hoekstra, J.W. Harper, and R.J. Youle. 2015. Endogenous Parkin Preserves Dopaminergic Substantia Nigral Neurons following Mitochondrial DNA Mutagenic Stress. *Neuron*. 87:371-381.

Pickrell, A.M., and R.J. Youle. 2015. The roles of PINK1, parkin, and mitochondrial fidelity in Parkinson's disease. *Neuron*. 85:257-273.

Pinnell, J.R., M. Cui, and K. Tieu. 2021. Exosomes in Parkinson disease. *J Neurochem*. 157:413-428.

Poewe, W., K. Seppi, C.M. Tanner, G.M. Halliday, P. Brundin, J. Volkmann, A.E. Schrag, and A.E. Lang. 2017. Parkinson disease. *Nat Rev Dis Primers*. 3:17013.

Ramirez, A., A. Heimbach, J. Grundemann, B. Stiller, D. Hampshire, L.P. Cid, I. Goebel, A.F. Mubaidin, A.L. Wriekat, J. Roeper, A. Al-Din, A.M. Hillmer, M. Karsak, B. Liss, C.G. Woods, M.I. Behrens, and C. Kubisch. 2006. Hereditary parkinsonism with dementia is caused by mutations in ATP13A2, encoding a lysosomal type 5 P-type ATPase. *Nat Genet*. 38:1184-1191.

Rampoldi, L., C. Dobson-Stone, J.P. Rubio, A. Danek, R.M. Chalmers, N.W. Wood, C. Verellen, X. Ferrer, A. Malandrini, G.M. Fabrizi, R. Brown, J. Vance, M. Pericak-Vance, G. Rudolf, S. Carre, E. Alonso, M. Manfredi, A.H. Nemeth, and A.P. Monaco. 2001. A conserved sorting-associated protein is mutant in chorea-acanthocytosis. *Nat Genet*. 28:119-120.

Ramseyer, V.D., V.A. Kimler, and J.G. Granneman. 2018. Vacuolar protein sorting 13C is a novel lipid droplet protein that inhibits lipolysis in brown adipocytes. *Mol Metab*. 7:57-70.

Ran, F.A., P.D. Hsu, J. Wright, V. Agarwala, D.A. Scott, and F. Zhang. 2013. Genome engineering using the CRISPR-Cas9 system. *Nat Protoc*. 8:2281-2308.

Reczek, D., M. Schwake, J. Schroder, H. Hughes, J. Blanz, X. Jin, W. Brondyk, S. Van Patten, T. Edmunds, and P. Saftig. 2007. LIMP-2 is a receptor for lysosomal mannose-6-phosphate-independent targeting of beta-glucocerebrosidase. *Cell*. 131:770-783.

Redding, K., J.H. Brickner, L.G. Marschall, J.W. Nichols, and R.S. Fuller. 1996. Allele-specific suppression of a defective trans-Golgi network (TGN) localization signal in Kex2p identifies three genes involved in localization of TGN transmembrane proteins. *Mol Cell Biol*. 16:6208-6217.

Reeve, A., M. Meagher, N. Lax, E. Simcox, P. Hepplewhite, E. Jaros, and D. Turnbull. 2013. The impact of pathogenic mitochondrial DNA mutations on substantia nigra neurons. *J Neurosci*. 33:10790-10801.

Riekkinen, P., U.K. Rinne, T.T. Pelliniemi, and V. Sonninen. 1975. Interaction between dopamine and phospholipids. Studies of the substantia nigra in Parkinson disease patients. *Arch Neurol*. 32:25-27.

Riley, J.S., and S.W. Tait. 2020. Mitochondrial DNA in inflammation and immunity. *EMBO Rep*. 21:e49799.

Robert, X., and P. Gouet. 2014. Deciphering key features in protein structures with the new ENDscript server. *Nucleic Acids Res*. 42:W320-324.

Rogers, L.D., and L.J. Foster. 2007. The dynamic phagosomal proteome and the contribution of the endoplasmic reticulum. *Proc Natl Acad Sci U S A*. 104:18520-18525.

Rothaug, M., F. Zunke, J.R. Mazzulli, M. Schweizer, H. Altmeppen, R. Lullmann-Rauch, W.W. Kallemeijn, P. Gaspar, J.M. Aerts, M. Glatzel, P. Saftig, D. Krainc, M. Schwake, and J. Blanz. 2014. LIMP-2 expression is critical for beta-glucocerebrosidase activity and alpha-synuclein clearance. *Proc Natl Acad Sci U S A*. 111:15573-15578.

Rowe, E.R., M.L. Mimmack, A.D. Barbosa, A. Haider, I. Isaac, M.M. Ouberai, A.R. Thiam, S. Patel, V. Saudek, S. Siniossoglou, and D.B. Savage. 2016. Conserved Amphipathic Helices Mediate Lipid Droplet Targeting of Perilipins 1-3. *J Biol Chem*. 291:6664-6678.

Rzepnikowska, W., K. Flis, S. Munoz-Braceras, R. Menezes, R. Escalante, and T. Zoladek. 2017. Yeast and other lower eukaryotic organisms for studies of Vps13 proteins in health and disease. *Traffic*. 18:711-719.

Saheki, Y., X. Bian, C.M. Schauder, Y. Sawaki, M.A. Surma, C. Klose, F. Pincet, K.M. Reinisch, and P. De Camilli. 2016. Control of plasma membrane lipid homeostasis by the extended synaptotagmins. *Nat Cell Biol*. 18:504-515.

Saheki, Y., and P. De Camilli. 2017. Endoplasmic Reticulum-Plasma Membrane Contact Sites. *Annu Rev Biochem*. 86:659-684.

Sakimoto, H., M. Nakamura, O. Nagata, I. Yokoyama, and A. Sano. 2016. Phenotypic abnormalities in a chorea-acanthocytosis mouse model are modulated by strain background. *Biochem Biophys Res Commun*. 472:118-124.

Samaranayake, H.S., A.E. Cowan, and L.A. Klobutcher. 2011. Vacuolar protein sorting protein 13A, TtVPS13A, localizes to the tetrahymena thermophila phagosome membrane and is required for efficient phagocytosis. *Eukaryot Cell*. 10:1207-1218.

Sato, S., M. Koike, M. Funayama, J. Ezaki, T. Fukuda, T. Ueno, Y. Uchiyama, and N. Hattori. 2016. Lysosomal Storage of Subunit c of Mitochondrial ATP Synthase in Brain-Specific Atp13a2-Deficient Mice. *Am J Pathol*. 186:3074-3082.

Saunders, A., E.Z. Macosko, A. Wysoker, M. Goldman, F.M. Krienen, H. de Rivera, E. Bien, M. Baum, L. Bortolin, S. Wang, A. Goeva, J. Nemesh, N. Kamitaki, S. Brumbaugh, D. Kulp, and S.A. McCarroll. 2018. Molecular Diversity and Specializations among the Cells of the Adult Mouse Brain. *Cell*. 174:1015-1030 e1016.

Schauder, C.M., X. Wu, Y. Saheki, P. Narayanaswamy, F. Torta, M.R. Wenk, P. De Camilli, and K.M. Reinisch. 2014. Structure of a lipid-bound extended synaptotagmin indicates a role in lipid transfer. *Nature*. 510:552-555.

Schmidt, E.M., E. Schmid, P. Munzer, A. Hermann, A.K. Eyrich, A. Russo, B. Walker, S. Gu, J.M. vom Hagen, C. Faggio, M. Schaller, M. Foller, L. Schols, M. Gawaz, O. Borst, A. Storch, C. Stournaras, and F. Lang. 2013. Chorein sensitivity of cytoskeletal organization and degranulation of platelets. *FASEB J*. 27:2799-2806.

Schormair, B., D. Kemlink, B. Mollenhauer, O. Fiala, G. Machetanz, J. Roth, R. Berutti, T.M. Strom, B. Haslinger, C. Trenkwalder, D. Zahorakova, P. Martasek, E. Ruzicka, and J. Winkelmann. 2018. Diagnostic exome sequencing in early-onset Parkinson's disease confirms VPS13C as a rare cause of autosomal-recessive Parkinson's disease. *Clin Genet*. 93:603-612.

Seifert, W., J. Kuhnisch, T. Maritzen, D. Horn, V. Haucke, and H.C. Hennies. 2011. Cohen syndrome-associated protein, COH1, is a novel, giant Golgi matrix protein required for Golgi integrity. *J Biol Chem*. 286:37665-37675.

Seifert, W., J. Kuhnisch, T. Maritzen, S. Lommatzsch, H.C. Hennies, S. Bachmann, D. Horn, and V. Haucke. 2015. Cohen syndrome-associated protein COH1 physically and functionally interacts with the small GTPase RAB6 at the Golgi complex and directs neurite outgrowth. *J Biol Chem*. 290:3349-3358.

Sekine, S., and R.J. Youle. 2018. PINK1 import regulation; a fine system to convey mitochondrial stress to the cytosol. *BMC Biol*. 16:2.

Seong, E., R. Insolera, M. Dulovic, E.J. Kamsteeg, J. Trinh, N. Bruggemann, E. Sandford, S. Li, A.B. Ozel, J.Z. Li, T. Jewett, A.J.A. Kievit, A. Munchau, V. Shakkottai, C. Klein, C.A. Collins, K. Lohmann, B.P. van de Warrenburg, and M. Burmeister. 2018. Mutations in VPS13D lead to a new recessive ataxia with spasticity and mitochondrial defects. *Ann Neurol*. 83:1075-1088.

Shang, G., C. Zhang, Z.J. Chen, X.C. Bai, and X. Zhang. 2019. Cryo-EM structures of STING reveal its mechanism of activation by cyclic GMP-AMP. *Nature*. 567:389-393.

Sherman, D.J., R. Xie, R.J. Taylor, A.H. George, S. Okuda, P.J. Foster, D.J. Needleman, and D. Kahne. 2018. Lipopolysaccharide is transported to the cell surface by a membrane-to-membrane protein bridge. *Science*. 359:798-801.

Shi, L., K. Howan, Q.T. Shen, Y.J. Wang, J.E. Rothman, and F. Pincet. 2013. Preparation and characterization of SNARE-containing nanodiscs and direct study of cargo release through fusion pores. *Nat Protoc*. 8:935-948.

Shiokawa, N., M. Nakamura, M. Sameshima, A. Deguchi, T. Hayashi, N. Sasaki, and A. Sano. 2013. Chorein, the protein responsible for chorea-acanthocytosis, interacts with beta-adducin and beta-actin. *Biochem Biophys Res Commun*. 441:96-101.

Showalter, M.R., A.L. Berg, A. Nagourney, H. Heil, K.L. Carraway, 3rd, and O. Fiehn. 2020. The Emerging and Diverse Roles of Bis(monoacylglycero) Phosphate Lipids in Cellular Physiology and Disease. *Int J Mol Sci*. 21.

Shui, W., L. Sheu, J. Liu, B. Smart, C.J. Petzold, T.Y. Hsieh, A. Pitcher, J.D. Keasling, and C.R. Bertozzi. 2008. Membrane proteomics of phagosomes suggests a connection to autophagy. *Proc Natl Acad Sci U S A*. 105:16952-16957.

Sidransky, E., and G. Lopez. 2012. The link between the GBA gene and parkinsonism. *Lancet Neurol*. 11:986-998.

Sliter, D.A., J. Martinez, L. Hao, X. Chen, N. Sun, T.D. Fischer, J.L. Burman, Y. Li, Z. Zhang, D.P. Narendra, H. Cai, M. Borsche, C. Klein, and R.J. Youle. 2018. Parkin and PINK1 mitigate STING-induced inflammation. *Nature*. 561:258-262.

Smolders, S., S. Philtjens, D. Crosiers, A. Sieben, E. Hens, B. Heeman, S. Van Mossevelde, P. Pals, B. Asselbergh, R. Dos Santos Dias, Y. Vermeiren, R. Vandenberghe, S. Engelborghs, P.P. De Deyn, J.J. Martin, P. Cras, W. Annaert, C. Van Broeckhoven, and B. consortium. 2021. Contribution of rare homozygous and compound heterozygous VPS13C missense mutations to dementia with Lewy bodies and Parkinson's disease. *Acta Neuropathol Commun*. 9:25.

Sprenger, H.G., T. MacVicar, A. Bahat, K.U. Fiedler, S. Hermans, D. Ehrentraut, K. Ried, D. Milenkovic, N. Bonekamp, N.G. Larsson, H. Nolte, P. Giavalisco, and T. Langer. 2021. Cellular pyrimidine imbalance triggers mitochondrial DNA-dependent innate immunity. *Nat Metab*. 3:636-650.

Struck, D.K., D. Hoekstra, and R.E. Pagano. 1981. Use of resonance energy transfer to monitor membrane fusion. *Biochemistry*. 20:4093-4099.

Swanson, K.V., R.D. Junkins, C.J. Kurkjian, E. Holley-Guthrie, A.A. Pendse, R. El Morabiti, A. Petrucelli, G.N. Barber, C.A. Benedict, and J.P. Ting. 2017. A noncanonical function of cGAMP in inflammasome priming and activation. *J Exp Med*. 214:3611-3626.

Taguchi, Y.V., J. Liu, J. Ruan, J. Pacheco, X. Zhang, J. Abbasi, J. Keutzer, P.K. Mistry, and S.S. Chandra. 2017. Glucosylsphingosine Promotes alpha-Synuclein Pathology in Mutant GBA-Associated Parkinson's Disease. *J Neurosci*. 37:9617-9631.

Tamura, N., T. Nishimura, Y. Sakamaki, I. Koyama-Honda, H. Yamamoto, and N. Mizushima. 2017. Differential requirement for ATG2A domains for localization to autophagic membranes and lipid droplets. *FEBS Lett*. 591:3819-3830.

Tasseva, G., H.D. Bai, M. Davidescu, A. Haromy, E. Michelakis, and J.E. Vance. 2013. Phosphatidylethanolamine deficiency in Mammalian mitochondria impairs oxidative phosphorylation and alters mitochondrial morphology. *J Biol Chem*. 288:4158-4173.

Tharkeshwar, A.K., D. Demedts, and W. Annaert. 2020. Superparamagnetic Nanoparticles for Lysosome Isolation to Identify Spatial Alterations in Lysosomal Protein and Lipid Composition. *STAR Protoc*. 1:100122.

Tharkeshwar, A.K., J. Trekker, W. Vermeire, J. Pauwels, R. Sannerud, D.A. Priestman, D. Te Vruchte, K. Vints, P. Baatsen, J.P. Decuypere, H. Lu, S. Martin, P. Vangheluwe, J.V. Swinnen, L. Lagae, F. Impens, F.M. Platt, K. Gevaert, and W. Annaert. 2017. A novel approach to analyze lysosomal dysfunctions through subcellular proteomics and lipidomics: the case of NPC1 deficiency. *Sci Rep*. 7:41408.

Thorsness, P.E., and T.D. Fox. 1993. Nuclear mutations in Saccharomyces cerevisiae that affect the escape of DNA from mitochondria to the nucleus. *Genetics*. 134:21-28.

Tomemori, Y., M. Ichiba, A. Kusumoto, E. Mizuno, D. Sato, S. Muroya, M. Nakamura, H. Kawaguchi, H. Yoshida, S. Ueno, K. Nakao, K. Nakamura, A. Aiba, M. Katsuki, and A. Sano. 2005. A gene-targeted mouse model for chorea-acanthocytosis. *J Neurochem*. 92:759-766.

Ueno, S., Y. Maruki, M. Nakamura, Y. Tomemori, K. Kamae, H. Tanabe, Y. Yamashita, S. Matsuda, S. Kaneko, and A. Sano. 2001. The gene encoding a newly discovered protein, chorein, is mutated in chorea-acanthocytosis. *Nat Genet*. 28:121-122.

Ugur, B., W. Hancock-Cerutti, M. Leonzino, and P. De Camilli. 2020. Role of VPS13, a protein with similarity to ATG2, in physiology and disease. *Curr Opin Genet Dev*. 65:61-68.

Valverde, D.P., S. Yu, V. Boggavarapu, N. Kumar, J.A. Lees, T. Walz, K.M. Reinisch, and T.J. Melia. 2019. ATG2 transports lipids to promote autophagosome biogenesis. *J Cell Biol*. 218:1787-1798.

van Veen, S., S. Martin, C. Van den Haute, V. Benoy, J. Lyons, R. Vanhoutte, J.P. Kahler, J.P. Decuypere, G. Gelders, E. Lambie, J. Zielich, J.V. Swinnen, W. Annaert, P. Agostinis, B. Ghesquiere, S. Verhelst, V. Baekelandt, J. Eggermont, and P. Vangheluwe. 2020. ATP13A2 deficiency disrupts lysosomal polyamine export. *Nature*. 578:419-424.

Vanier, M.T. 2010. Niemann-Pick disease type C. *Orphanet J Rare Dis*. 5:16.

Velayos-Baeza, A., A. Vettori, R.R. Copley, C. Dobson-Stone, and A.P. Monaco. 2004. Analysis of the human VPS13 gene family. *Genomics*. 84:536-549.

Velikkakath, A.K., T. Nishimura, E. Oita, N. Ishihara, and N. Mizushima. 2012. Mammalian Atg2 proteins are essential for autophagosome formation and important for regulation of size and distribution of lipid droplets. *Mol Biol Cell*. 23:896-909.

Vidyadhara, D.J., J.E. Lee, and S.S. Chandra. 2019. Role of the endolysosomal system in Parkinson's disease. *J Neurochem*. 150:487-506.

Voelker, D.R. 1984. Phosphatidylserine functions as the major precursor of phosphatidylethanolamine in cultured BHK-21 cells. *Proc Natl Acad Sci U S A*. 81:2669-2673.

Vonk, J.J., W.M. Yeshaw, F. Pinto, A.I. Faber, L.L. Lahaye, B. Kanon, M. van der Zwaag, A. Velayos-Baeza, R. Freire, I.S.C. van, N.A. Grzeschik, and O.C. Sibon. 2017. Drosophila Vps13 Is Required for Protein Homeostasis in the Brain. *PLoS One*. 12:e0170106.

Wallings, R., N. Connor-Robson, and R. Wade-Martins. 2019. LRRK2 interacts with the vacuolar-type H+-ATPase pump a1 subunit to regulate lysosomal function. *Hum Mol Genet*. 28:2696-2710.

Walsh, M.T., E. Di Leo, I. Okur, P. Tarugi, and M.M. Hussain. 2016. Structure-function analyses of microsomal triglyceride transfer protein missense mutations in abetalipoproteinemia and hypobetalipoproteinemia subjects. *Biochim Biophys Acta*. 1861:1623-1633.

Wang, C., M.E. Ward, R. Chen, K. Liu, T.E. Tracy, X. Chen, M. Xie, P.D. Sohn, C. Ludwig, A. Meyer-Franke, C.M. Karch, S. Ding, and L. Gan. 2017. Scalable Production of iPSC-Derived Human Neurons to Identify Tau-Lowering Compounds by High-Content Screening. *Stem Cell Reports*. 9:1221-1233.

Wang, C.W., J. Kim, W.P. Huang, H. Abeliovich, P.E. Stromhaug, W.A. Dunn, Jr., and D.J. Klionsky. 2001. Apg2 is a novel protein required for the cytoplasm to vacuole targeting, autophagy, and pexophagy pathways. *J Biol Chem*. 276:30442-30451.

Wang, S., S. Zhang, L.C. Liou, Q. Ren, Z. Zhang, G.A. Caldwell, K.A. Caldwell, and S.N. Witt. 2014. Phosphatidylethanolamine deficiency disrupts alpha-synuclein homeostasis in yeast and worm models of Parkinson disease. *Proc Natl Acad Sci U S A*. 111:E3976-3985.

Weber, T., B.V. Zemelman, J.A. McNew, B. Westermann, M. Gmachl, F. Parlati, T.H. Sollner, and J.E. Rothman. 1998. SNAREpins: minimal machinery for membrane fusion. *Cell*. 92:759-772.

Weindel, C.G., S.L. Bell, K.J. Vail, K.O. West, K.L. Patrick, and R.O. Watson. 2020. LRRK2 maintains mitochondrial homeostasis and regulates innate immune responses to Mycobacterium tuberculosis. *Elife*. 9.

West, A.B., D.J. Moore, S. Biskup, A. Bugayenko, W.W. Smith, C.A. Ross, V.L. Dawson, and T.M. Dawson. 2005. Parkinson's disease-associated mutations in leucine-rich repeat kinase 2 augment kinase activity. *Proc Natl Acad Sci U S A*. 102:16842-16847.

West, A.P., W. Khoury-Hanold, M. Staron, M.C. Tal, C.M. Pineda, S.M. Lang, M. Bestwick, B.A. Duguay, N. Raimundo, D.A. MacDuff, S.M. Kaech, J.R. Smiley, R.E. Means, A. Iwasaki, and G.S. Shadel. 2015. Mitochondrial DNA stress primes the antiviral innate immune response. *Nature*. 520:553-557.

West, A.P., and G.S. Shadel. 2017. Mitochondrial DNA in innate immune responses and inflammatory pathology. *Nat Rev Immunol*. 17:363-375.

Wilhelm, L.P., C. Wendling, B. Vedie, T. Kobayashi, M.P. Chenard, C. Tomasetto, G. Drin, and F. Alpy. 2017. STARD3 mediates endoplasmic reticulum-to-endosome cholesterol transport at membrane contact sites. *EMBO J*. 36:1412-1433.

Wong, L.H., A. Copic, and T.P. Levine. 2017. Advances on the Transfer of Lipids by Lipid Transfer Proteins. *Trends Biochem Sci*. 42:516-530.

Wong, L.H., A.T. Gatta, and T.P. Levine. 2019. Lipid transfer proteins: the lipid commute via shuttles, bridges and tubes. *Nat Rev Mol Cell Biol*. 20:85-101.

Wong, Y.C., D. Ysselstein, and D. Krainc. 2018. Mitochondria-lysosome contacts regulate mitochondrial fission via RAB7 GTP hydrolysis. *Nature*. 554:382-386.

Wyant, G.A., M. Abu-Remaileh, R.L. Wolfson, W.W. Chen, E. Freinkman, L.V. Danai, M.G. Vander Heiden, and D.M. Sabatini. 2017. mTORC1 Activator SLC38A9 Is Required to Efflux Essential Amino Acids from Lysosomes and Use Protein as a Nutrient. *Cell*. 171:642-654 e612.

Yambire, K.F., C. Rostosky, T. Watanabe, D. Pacheu-Grau, S. Torres-Odio, A. Sanchez-Guerrero, O. Senderovich, E.G. Meyron-Holtz, I. Milosevic, J. Frahm, A.P. West, and N. Raimundo. 2019. Impaired lysosomal acidification triggers iron deficiency and inflammation in vivo. *Elife*. 8.

Yang, R.Y., H. Xue, L. Yu, A. Velayos-Baeza, A.P. Monaco, and F.T. Liu. 2016. Identification of VPS13C as a Galectin-12-Binding Protein That Regulates Galectin-12 Protein Stability and Adipogenesis. *PLoS One*. 11:e0153534.

Yeshaw, W.M., M. van der Zwaag, F. Pinto, L.L. Lahaye, A.I. Faber, R. Gomez-Sanchez, A.M. Dolga, C. Poland, A.P. Monaco, I.S.C. van, N.A. Grzeschik, A. Velayos-Baeza, and O.C. Sibon. 2019. Human VPS13A is associated with multiple organelles and influences mitochondrial morphology and lipid droplet motility. *Elife*. 8.

Yim, W.W., and N. Mizushima. 2020. Lysosome biology in autophagy. *Cell Discov*. 6:6.

Youle, R.J., and D.P. Narendra. 2011. Mechanisms of mitophagy. *Nat Rev Mol Cell Biol*. 12:9-14.

Ysselstein, D., J.M. Shulman, and D. Krainc. 2019. Emerging links between pediatric lysosomal storage diseases and adult parkinsonism. *Mov Disord*. 34:614-624.

Yu, C.H., S. Davidson, C.R. Harapas, J.B. Hilton, M.J. Mlodzianoski, P. Laohamonthonkul, C. Louis, R.R.J. Low, J. Moecking, D. De Nardo, K.R. Balka, D.J. Calleja, F. Moghaddas, E. Ni, C.A. McLean, A.L. Samson, S. Tyebji, C.J. Tonkin, C.R. Bye, B.J. Turner, G. Pepin, M.P. Gantier, K.L. Rogers, K. McArthur, P.J. Crouch, and S.L. Masters. 2020a. TDP-43 Triggers Mitochondrial DNA Release via mPTP to Activate cGAS/STING in ALS. *Cell*. 183:636-649 e618.

Yu, H., Y. Liu, D.R. Gulbranson, A. Paine, S.S. Rathore, and J. Shen. 2016. Extended synaptotagmins are Ca2+-dependent lipid transfer proteins at membrane contact sites. *Proc Natl Acad Sci U S A*. 113:4362-4367.

Yu, H., T. Sun, J. An, L. Wen, F. Liu, Z. Bu, Y. Cui, and J. Feng. 2020b. Potential Roles of Exosomes in Parkinson's Disease: From Pathogenesis, Diagnosis, and Treatment to Prognosis. *Front Cell Dev Biol*. 8:86.

Yu, L., C.K. McPhee, L. Zheng, G.A. Mardones, Y. Rong, J. Peng, N. Mi, Y. Zhao, Z. Liu, F. Wan, D.W. Hailey, V. Oorschot, J. Klumperman, E.H. Baehrecke, and M.J. Lenardo. 2010. Termination of autophagy and reformation of lysosomes regulated by mTOR. *Nature*. 465:942-946.

Yuan, L., and J.Y. Li. 2019. Exosomes in Parkinson's Disease: Current Perspectives and Future Challenges. *ACS Chem Neurosci*. 10:964-972.

Zavodszky, E., M.N. Seaman, K. Moreau, M. Jimenez-Sanchez, S.Y. Breusegem, M.E. Harbour, and D.C. Rubinsztein. 2014. Mutation in VPS35 associated with Parkinson's disease impairs WASH complex association and inhibits autophagy. *Nat Commun*. 5:3828.

Zhang, C., G. Shang, X. Gui, X. Zhang, X.C. Bai, and Z.J. Chen. 2019. Structural basis of STING binding with and phosphorylation by TBK1. *Nature*. 567:394-398.

Zhang, M., H. Mu, Z. Shang, K. Kang, H. Lv, L. Duan, J. Li, X. Chen, Y. Teng, Y. Jiang, and R. Zhang. 2017. Genome-wide pathway-based association analysis identifies risk pathways associated with Parkinson's disease. *Neuroscience*. 340:398-410.

Zunke, F., A.C. Moise, N.R. Belur, E. Gelyana, I. Stojkovska, H. Dzaferbegovic, N.J. Toker, S. Jeon, K. Fredriksen, and J.R. Mazzulli. 2018. Reversible Conformational Conversion of alpha-Synuclein into Toxic Assemblies by Glucosylceramide. *Neuron*. 97:92-107 e110.